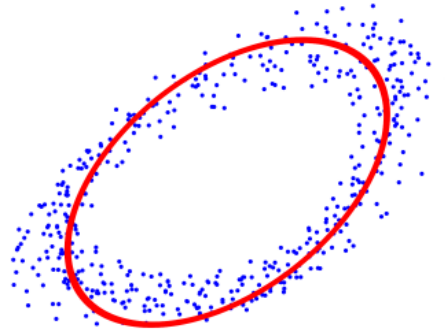




DEPARTMENT OF AEROSPACE ENGINEERING
INDIAN INSTITUTE OF TECHNOLOGY
MADRAS
CHENNAI-600 036

Thermoacoustic oscillations in hydrogen enriched turbulent combustion



A thesis

Submitted by

Abhishek Kushwaha

For the award of the degree

Of

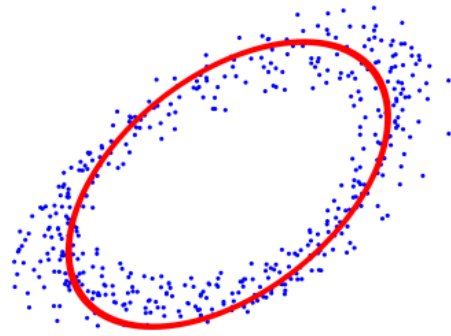
DOCTOR OF PHILOSOPHY

September, 2023



DEPARTMENT OF AEROSPACE ENGINEERING
INDIAN INSTITUTE OF TECHNOLOGY
MADRAS
CHENNAI-600 036

Thermoacoustic oscillations in hydrogen enriched turbulent combustion



A thesis

Submitted by

Abhishek Kushwaha

For the award of the degree

Of

DOCTOR OF PHILOSOPHY

September, 2023

QUOTATIONS

सर्वतीर्थमयी माता सर्वदेवमयः पिता
मातरं पितरं तस्मात् सर्वयत्नेन पूजयेत्

English Couplet:

Mother is (the embodiment) of all pilgrimages, father is (the embodiment) of all deities.

Hence, mother and father are to be revered with all efforts.

- SUBHĀṢITAS

DEDICATION

To my mother and father

THESIS CERTIFICATE

This is to undertake that the thesis titled, **THERMOACOUSTIC OSCILLATIONS IN HYDROGEN ENRICHED TURBULENT COMBUSTION** submitted by **Abhishek Kushwaha** to the Indian Institute of Technology Madras, for the award of Doctor of Philosophy, is a bonafide record of the research work done by me under the supervision of Prof. R. I. Sujith. The contents of this thesis, in full or in parts, have not been submitted to any other Institute or University for the award of any degree or diploma.

Chennai 600 036

Research Scholar

Date: 11 September, 2023

Research Guide

Prof. R. I. Sujith

Professor

Dept. of Aerospace Engineering

IIT Madras, 600 036

LIST OF PUBLICATIONS

The publications arising out of the work mentioned in this thesis are given as follows

1. REFEREED JOURNAL ARTICLES BASED ON THE THESIS

- (a) **A. Kushwaha, K. Praveen, Samadhan A. Pawar, R. I. Sujith, I. Chterev, and I. Boxx** (2021). Dynamical characterization of thermoacoustic oscillations in a hydrogen-enriched partially premixed swirl-stabilized methane/air combustor. *Journal of Engineering for Gas Turbines and Power*, **143(12)**: , 121022 (11 pages).

2. REFEREED JOURNAL ARTICLES (Others)

- (a) **A. Sahay, A. Kushwaha, Samadhan A. Pawar, PR Midhun, Jayesh M. Dhadphale, and R. I. Sujith** (2023). Mitigation of limit cycle oscillations in a turbulent thermoacoustic system via delayed acoustic self-feedback. *Chaos: An Interdisciplinary Journal of Nonlinear Science*, **33(4)**, 043118.

3. REFEREED CONFERENCE ARTICLES

- (a) **A. Kushwaha, K. Praveen, Samadhan A. Pawar, R. I. Sujith, I. Chterev, and I. Boxx** (2021). Dynamical characterization of thermoacoustic oscillations in a hydrogen-enriched partially premixed swirl-stabilized methane/air combustor. *Turbo Expo: Power for Land, Sea, and Air*, (pp. **V03BT04A024**).

ACKNOWLEDGEMENTS

This thesis is a culmination of diligent efforts, invaluable guidance, and unwavering support from numerous individuals, whose contributions were essential to its successful completion. First and foremost, I am deeply indebted to my thesis advisor, Prof. R. I. Sujith, for his unwavering support, guidance, and invaluable insights throughout the research process. His encouragement to pursue unconventional ideas resulted in some of the most thrilling experiences of my Ph.D studies. His emphasis on clear, precise, and accessible scientific writing has improved me in better comprehending and communicating my work. He has instilled in me the qualities of an open-minded researcher, inspiring me to explore diverse research avenues with enthusiasm. The knowledge I have gained from him is invaluable, and I will forever regard him as a source of inspiration in my academic journey. In the years to come, his never-ending quest to choose happiness in the face of adversity during research will continue to be my guiding light.

I am indebted to Prof. P. Sriram and Prof. H. S. N. Murthy for their guidance and encouragement during various stages of my Ph. D. I wish to also thank Prof. Dr. Nagabhushana Rao Vadlamani, Prof. Nandan Kumar Sinha and Prof. Niket Kaisare for motivating me and critically reviewing my research work as a part of my Doctoral Committee. I am particularly grateful to Prof. Chandramouli, P., Prof. Srinivasan, K. and Prof. Pravendra Kumar for providing guidance and advice at various crucial junctures in my life.

I am extremely grateful to Prof. Isaac Boxx (DLR, Stuttgart, Germany) for his generosity in sharing the experimental datasets on hydrogen-enriched combustion. It was a pleasure to meet and work with him in RWTH Aachen University, Germany. I had a great learning experience. I would also like to thank Dr. Ianko Chterelev for conducting a great experimental campaign and tabulated every minor details related to the experiments.

I would like to acknowledge Ministry of Human Resources and Development, India for providing me financial support for my Ph. D. programme. I would also like to express my gratitude to IIT Madras for providing me funds to visit RWTH Aachen University, Germany. I would like to acknowledge the European Research Council (ERC) for the project 'Hyburn' under the European Union's Horizon 2020 research and innovation program.

I am greatly thankful to my colleagues from RGD lab. Particularly, I would like to thank Dr. Praveen Kasthuri, Dr. Amitesh Roy and Dr. Samadhan Ananda Pawar, who guided me during my first project. Whenever I needed help or advise during my Ph. D, I knew I could count on them. I would also like to thank Jayesh M. Dhadphale, Sivakumar, Rohit R., Shruti Tandon, Sanket Ambedkar and Thonti Beeraiah. I would never have had the courage to try new things if it hadn't been for their support. I would also like to thank Samarjeet Singh, Sri Vignesh, Dr. Manikandan R., Dr. Induja Pavitaran and Dr. Ankan Banerjee, who have made my time at work and outside work memorable. I would like to thank Thilagraj and Anand for supporting me with their manufacturing skills. I would also thank Ankit Sahay, Dr. Somnath De and Ramesh Bhavi for correcting my thesis.

I wish to convey my profound gratitude to my family, specially for my father Sukhbasi Lal Kushwaha, and my mother Munny Devi. Their unwavering love, affection, and steadfast support have been instrumental in my education, sustaining me through numerous challenging circumstances. I am eternally thankful to my sisters Nisha and Asha, for their unwavering support and guardianship over the past five years. Additionally, I am indebted to my friends, particularly Pragya Pahariya, Anushi Misra, Divya Shikhar Singh, Vikas Yadav, Rajan Kumar and Sandeep Kumar, for their invaluable emotional support during various trying times.

ABSTRACT

KEYWORDS: Thermoacoustic instability; Hydrogen-enriched combustion; Proper orthogonal decomposition (POD); Spatiotemporal dynamics; Synchronization.

Traditionally, various power-producing industries have relied on hydrocarbon-based fuels to generate significant power. However, due to the increasing demand for power and mounting concerns surrounding pollution, alternative methods for power generation are being actively explored. One promising alternative is the utilization of hydrogen as a fuel, as it is considered to be a clean energy source. The combustion of hydrogen produces high temperatures, which can result in the formation of NO_x emissions. To address this challenge, a mixture of hydrogen and hydrocarbon fuels is employed to mitigate the issue of excessive temperatures. However, under lean fuel conditions with hydrogen-enriched fuels, combustors are susceptible to thermoacoustic instability.

For several decades, the occurrence of thermoacoustic instabilities has posed a persistent challenge in both aero and rocket engines and land-based power-generating systems. The occurrence of self-sustained, large amplitude periodic oscillations within a combustor can be attributed to the intricate interplay among the confined acoustic field, unsteady combustion, and the hydrodynamic flow field, which collectively form the phenomenon known as thermoacoustic instability. The presence of such instabilities poses significant risks to the safe operation of the combustor, as high-pressure fluctuations can concurrently damage multiple components of the combustor and gas

turbine engine. Along with thermoacoustic instability, it is important to understand other dynamical changes including transition to thermoacoustic instability, existence of chaotic oscillations, intermittency and their underlying mechanisms, resulting from the incremental addition of hydrogen.

Firstly, the stability of a turbulent combustor as a function of hydrogen volume fraction in the fuel flow rate is investigated while maintaining a constant global equivalence ratio and thermal power in a technically premixed swirl combustor (PRECCINSTA). The datasets were provided by Dr. Isaac Boxx of the German Aerospace Center (DLR), located in Stuttgart, Germany, originating from the experiments conducted by his research team. Successive increments in hydrogen fuel fraction cause the dominant frequency of the acoustic pressure to gradually increase to higher values due to increased temperature in the system. We observe that different acoustic modes can be excited with hydrogen enrichment. Using tools derived from the synchronization theory, we also characterize different dynamical states that the combustor exhibits as a result of interaction among different acoustic modes. We find chaotic oscillations along with the states of intermittency and thermoacoustic instabilities having period-1 and period-2 limit cycle oscillations. Besides temporal analysis, we also investigate the spatiotemporal dynamics for each dynamic state using the instantaneous snapshots from the flow velocity field, OH-PLIF field and OH*-chemiluminescence field. Along with the dynamical characterization, we also study the transition from period-2 limit cycle oscillations to period-1 limit cycle oscillations via chaotic oscillations due to interaction of multiple acoustic modes in the combustion chamber.

Second, we study the coupled behaviour between fluctuations in the acoustic pressure, the heat release rate oscillations and flow velocity field in the combustion chamber during different states of thermoacoustic instability using a data driven method known as proper orthogonal decomposition (POD). We identify dominating coherent structures as spatial modes in the reactive field and rank them based on their respective fraction of turbulent kinetic energy. Along with the spatial information, we also calculate the temporal coefficients of each POD mode of velocity field. Using the temporal coefficients of dominating modes, we analyze the temporal signals and observe 1:1 and 2:1 frequency locking among the acoustic pressure, heat release rate and flow velocity fluctuations during the states of thermoacoustic instabilities. These frequency-locked states, which indicate the underlying phase-synchronization states, are observed to be correlated with coherent structures in the flow velocity field.

Finally, to understand the underlying mechanism behind the correlation among dominating structures from different spatial data fields, we study interaction between coupled structures from the OH-PLIF and the OH*-chemiluminescence fields acquired simultaneously during the states of thermoacoustic instabilities. We calculate the extended POD modes of OH-PLIF and OH*-chemiluminescence snapshots with the help of temporal coefficients of POD modes of the velocity field. We find the structures in flame surface and heat release rate that are correlated with the dominant coherent structures of the flow field using extended POD (EPOD). We observe that the structures in the flow velocity, flame surface and heat release rate fields correlate and share the same spatial regions during thermoacoustic instability with period-1 limit cycle oscillations. In the case of period-2 limit cycle oscillations, the structures from flame

surface and heat release rate field are strongly correlated. However, these structures contribute less to the coherent structures of the flow field.

TABLE OF CONTENTS

	Page
ACKNOWLEDGEMENTS	i
ABSTRACT	v
LIST OF TABLES	xiii
LIST OF FIGURES	xix
GLOSSARY	xxi
ABBREVIATIONS	xxii
NOTATION	xxiv
CHAPTER 1 INTRODUCTION	1
1.1 Hydrogen-enriched fuels: A better alternative	4
1.1.1 Effect of hydrogen enrichment on flame stability	5
1.1.2 Variation in flame speed due to hydrogen enrichment	6
1.1.3 Effect of hydrogen addition on flame shapes	6
1.1.4 Other effects of hydrogen enrichment	7
1.2 Thermoacoustic instability: A complex problem	8
1.3 Mechanisms Leading to Thermoacoustic Instability	10
1.3.1 Fluctuations in flame surface area	11
1.3.2 Coherent structures in flow field	11
1.3.3 Fluctuations in equivalence ratio	12
1.3.4 Other mechanisms	13

1.4	Nonlinear Dynamics of Thermoacoustic Systems	14
1.5	Thermoacoustic instability in hydrogen-enriched combustion	15
1.6	Dynamical Systems Approach	19
1.7	Modal decomposition of thermoacoustic systems	22
1.8	Objectives of the Thesis	25
1.9	Overview of the work	27
CHAPTER 2 EXPERIMENTAL FACILITIES		30
2.1	Experimental setup	30
2.2	Acoustic signal acquisition	32
2.3	Optical measurements	33
2.3.1	Stereoscopic particle image velocimetry (SPIV)	33
2.3.2	OH*-Chemiluminescence	34
2.3.3	OH - planar laser-induced fluorescence (PLIF)	35
2.4	Operational conditions	37
CHAPTER 3 METHODOLOGIES FOR ANALYSES		39
3.1	Nonlinear time series analysis (NTSA)	39
3.1.1	Phase-space reconstruction	40
3.2	Other methods for analysis	46
3.2.1	Power spectrum	46
3.2.2	Continuous wavelet transform (CWT)	49
3.3	Proper Orthogonal Decomposition (POD)	51
3.4	Extended proper orthogonal decomposition (EPOD)	54
3.5	Hilbert transform and analytical signals	56
3.6	Quantifying chaotic behavior of temporal dynamics	58

CHAPTER 4 CHARACTERIZATION OF DYNAMICAL STATES AND TRANSITION DUE TO H₂ ENRICHMENT	61
4.1 Period-1 limit cycle oscillations	63
4.2 Period-2 limit cycle oscillations	65
4.3 Intermittency	68
4.4 Chaotic oscillations	72
4.5 Transition from P2 LCO to P1 LCO	79
4.6 Interim summary	82
CHAPTER 5 FREQUENCY LOCKING AMONG ACOUSTIC PRESSURE, HEAT RELEASE RATE AND FLOW VELOCITY	85
5.1 Chaotic state-1 oscillations	85
5.2 1:1 Frequency Locking	88
5.3 2:1 Frequency Locking	93
5.4 Interim summary	97
CHAPTER 6 COUPLED LARGE-SCALE STRUCTURES FROM FLOW, FLAME AND HEAT RELEASE RATE DISTRIBUTION FIELDS	100
6.1 Chaotic oscillations in the absence of H ₂	102
6.2 Period-1 limit cycle oscillations at 50% H ₂ enrichment	108
6.3 Period-2 limit cycle oscillations at 20% H ₂ enrichment	113
6.4 Interim summary	119
CHAPTER 7 CONCLUSION AND SCOPE FOR FUTURE WORK	121
APPENDIX A GLOBAL EQUIVALENCE RATIO, THERMAL POWER RATING AND VISCOSITY CALCULATION FOR A H₂-CH₄-AIR MIXTURE	126

A.1	Calculation of global equivalence ratio for H_2-CH_4 -air mixture	126
A.2	Determination of Thermal Power (\mathcal{P}) rating for the burner	128
A.3	Determination of nominal Reynolds number (Re) H_2-CH_4 -air mixture	129
A.4	Determination of viscosity of H_2-CH_4 -air mixture	130
 APPENDIX B ADIABATIC FLAME TEMPERATURE CALCULATION FOR A H_2-CH_4-AIR MIXTURE		131
 REFERENCES		144

LIST OF TABLES

Table	Title	Page
2.1	Different dynamical states observed by increasing FFF (%) for $\mathcal{P} = 10.5$ kW, 15.6 kW, and 20.8 kW for $\phi_g = 0.65$ and 0.8. The expanded forms of the abbreviations used in the table are provided in the Abbreviations section (see pages xix-xx). NA refers to non-availability of data at that conditions due to the breakage of the quartz window allowing optical access to the combustor.	37
3.1	The values of different operating parameters during the experiments. Keys: $H_2(\%)$ - Volumetric percentage of H_2 in the fuel; Re - Nominal Reynolds number; ϕ_g - Global equivalence ratio; \mathcal{P} - Thermal power rating (kW) and dynamical states. The experimental cases analysed here are shown.	54
5.1	Results of the 0-1 test for different signal during all the dynamical states discussed in this paper. The values close to 1 indicate the existence of chaos in the signal. The signal with regular dynamics show the values close to 0.	88

LIST OF FIGURES

1.1	The positive feedback mechanism between the unsteady heat release rate and the acoustic field, a prerequisite for the development of thermoacoustic instability, is depicted schematically. When the system's damping is overwhelmed by the system's acoustic force (driving), thermoacoustic oscillations occur.	2
2.1	(a) Schematic of the experimental setup of the technically premixed gas turbine model combustor. Different regions and shear layers are indicated with the abbreviations which are: OSL - Outer shear layer, ISL - Inner shear layer, ORZ - Outer recirculation zone and IRZ - Inner recirculation zone. Different coloured rectangles indicate the regions captured by different image-capturing techniques. Instantaneous (b) vorticity field, (c) OH-PLIF intensity showing the flame area, and (d) OH*-chemiluminescence field showing the heat release rate distribution are also shown for reference	31
3.1	3-dimensional phase portrait of (a) period-1, (b) period-2, and (c) quasi-periodic signals using sinusoidal waves, and (d) Lorenz attractor are obtained through phase space reconstruction.	45
3.2	(a) Sinusoidal waves with two different frequencies (2 Hz and 5 Hz) for different time intervals and, (b) the corresponding scalogram are shown.	50
4.1	(a) The time series (b) scalogram, (c) three-dimensional phase space, and (d) power spectrum of p' during the state of P1 LCO, observed for $\mathcal{P} = 20.8$ kW, $\phi_g = 0.65$, $HFF = 50\%$, and $Re = 2.64 \times 10^4$	63
4.2	(I) The overlapped time series of normalized p' and \dot{q}' fluctuations during the state of P1 LCO. The instantaneous (II) PIV images, (III) OH-PLIF images, and (IV) OH*-chemiluminescence images corresponding to five instants (a-e) over a cycle of p' signal are shown.	64
4.3	(a) The time series, (b) scalogram, (c) three-dimensional phase space, and (d) power spectrum of p' signal during the state of P2 LCO observed for $\mathcal{P} = 20.8$ kW, $\phi_g = 0.65$, $HFF = 20\%$, and $Re = 2.72 \times 10^4$	66
4.4	(I) The overlapped time series of normalized p' and \dot{q}' fluctuations during the state of P2 LCO. The instantaneous (II) PIV, (III) OH-PLIF, and (IV) OH*-chemiluminescence images corresponding to five instants (a-e) over a cycle of the p' signal are shown.	67

4.5	(a) The time series, (b) scalogram, (c) three-dimensional phase space, and (d) power spectrum of p' signal during the state of intermittency for $\mathcal{P} = 20.8$ kW, $\phi_g = 0.65$, $HFF = 40\%$, and $Re = 2.68 \times 10^4$	69
4.6	(I) The time series of normalized p' and q' fluctuations during the aperiodic epoch in the state of intermittency. The corresponding (II) PIV (III) OH-PLIF, and (IV) OH*- chemiluminescence images are shown.	70
4.7	(I) The time series of normalized p' and q' fluctuations for five instants (a-e) during one periodic cycle in the state of intermittency. The corresponding (II) PIV, (III) OH-PLIF, and (IV) OH*- chemiluminescence images are shown.	71
4.8	(a) The time series, (b) scalogram, (c) three-dimensional phase space, and (d) power spectrum of p' during chaotic state-1 (CO1), observed for $\mathcal{P} = 20.8$ kW, $\phi_g = 0.65$, $HFF = 0\%$, and $Re = 2.41 \times 10^4$	73
4.9	(a) The time series, (b) scalogram, (c) three-dimensional phase space, and (d) power spectrum of p' signal during chaotic state-2 (CO2) for $\mathcal{P} = 15.6$ kW, $\phi_g = 0.8$, $HFF = 70\%$, and $Re = 1.42 \times 10^4$	74
4.10	0-1 test performed for chaotic state-1 (Fig. 4.8a) and chaotic state-2 (Fig. 4.9a). (i) The plot between the translation variables $x(n)$ and $y(n)$, (ii) the behaviour of mean square displacement $M(n)$ with n , and (iii) the variation of the growth rate K with N	75
4.11	(I) The time series of normalized p' and q' fluctuations for five time instants (a-h) during different instants indicating the local maxima and minima in chaotic state-1. The corresponding (II) PIV (III) OH-PLIF, and (IV) OH*- chemiluminescence images are shown.	76
4.12	(I) The time series of normalized p' and q' fluctuations for eight time instants (a-h) during different instants indicating the local maxima and minima in chaotic state-2 (CO2). The corresponding (II) PIV, (III) OH-PLIF, and (IV) OH*- chemiluminescence images are shown.	78
4.13	The effect of increasing HFF in the fuel on the acoustic pressure oscillations is presented using (I) time series, (II) amplitude spectrum, and (III) three-dimensional phase space, and (IV) first return map of p' oscillations. HFF is varied from 0% to 60% in steps of 10% while maintaining $\mathcal{P} = 15.6$ kW and $\phi_g = 0.8$. The red colored dotted line in (II) represents the frequency of the fundamental mode in the combustor for 0% HFF	80

5.1	Characterization of the thermoacoustic response during the state of chaotic oscillations. (a) Time series and (b) power spectra of fluctuations in acoustic pressure, heat release rate and the temporal coefficients of the first three POD modes. (c) Phase space trajectory in the complex analytical plane for the part of the signals indicated in panel (a).	86
5.2	(a-c) Phase portrait of the pairs of temporal coefficients ($a_1 - a_3$) of the first three POD modes of the velocity field for the state of chaotic oscillations. The red lines indicate a few periodic orbits.	87
5.3	Illustration of 1:1 frequency locking between p' and q' signals during the state of period-1 LCO. (a) Time series of the normalized p' (black line) and q' (orange line) signals, (b, c) the corresponding phase spaces, and (d, e) first return maps for $\mathcal{P} = 15.6$ kW, $\phi_g = 0.8$ and $HFF = 50\%$. (f) The zoomed view of the signals with markers corresponding to the local maximas. (g, h) The spiking signals indicating the locations of local maxima in p' and q' oscillations, respectively. C_1, C_2, \dots in (g) represent the number of cycles, and blue dotted boxes contain the number of peaks in one oscillation cycle of p' and q' signals.	89
5.4	(a) time series of (i) acoustic pressure, (ii) heat release rate, (iii - v) temporal coefficients of first three POD modes normalised by their respective maxima values; (b) the corresponding power spectra and (c) the analytical signals in the complex plane, corresponding to the time series enclosed in the red dashed box during the state of period-1 limit cycle oscillations for $\mathcal{P} = 20.8$ kW, $\phi_g = 0.8$, $HFF = 50\%$, and $Re = 2.64 \times 10^4$	91
5.5	(a-f) Phase portrait of the temporal coefficients of the POD modes of the flow velocity field with respect to acoustic pressure and heat release rate along with analytical curves having the same dominating frequencies and phase differences as the original data and the corresponding phase difference with the red line indicating the mean value of phase difference, for the state of TAI with period-1 LCO.	92
5.6	Depiction of 2:1 frequency locking between p' and q' signals during the state of P2 LCO. (a) Time series of normalized p' (black line) and q' (orange line) signals, (b, c) the corresponding phase spaces, and (d, e) first return maps for the conditions of $\mathcal{P} = 15.6$ kW, $\phi_g = 0.8$ and $HFF = 0\%$. The description of (f, g, h) is the same as that in Fig. 5.3.	93

5.7	(a) time series of (i) acoustic pressure (ii) heat release rate (iii - v) temporal coefficients of first three POD modes normalised by their respective maxima values; (b) the corresponding power spectra and (c) the analytical signals in the complex plane, corresponding to the time series enclosed in the red dashed box during the state of period-2 limit cycle oscillations for $\mathcal{P} = 20.8$ kW, $\phi_g = 0.8$, $FFF = 20\%$, and $Re = 2.74 \times 10^4$	95
5.8	(a-f) Phase portrait of the temporal coefficients of the POD modes of the flow velocity field with respect to acoustic pressure and heat release rate along with analytical curves having the same dominating frequencies and phase differences as the original data and the corresponding phase difference with the red line indicating the mean value of phase difference, for the state of TAI with period-2 LCO.	96
6.1	Fraction of the kinetic energy contained in the spectrum of POD modes (6.1) obtained from the flow velocity field (\mathbf{u}') for the three dynamical states highlighted in Table 3.1. The key role played by large-scale coherent structures during the states of thermoacoustic instabilities (period-1 and period-2) is depicted by the first two principal modes containing an order of magnitude higher kinetic energy than that observed during stable operation.	101
6.2	Flow and flame dynamics for the purely CH ₄ -air flame for the baseline condition. Mean of the (a) transverse velocity component u_x , (b) flame brush obtained from OH-PLIF images, and (c) heat release rate fluctuations obtained from OH*-chemiluminescence. Panels (d-f) shows the first three POD modes of u'_x and the extended modes associated with I'_P and I'_C	104
6.3	Flow and flame dynamics for the purely CH ₄ -air flame. Mean of the (a) axial velocity component (u_y), (b) flame brush obtained from OH-PLIF images, and (c) heat release rate fluctuations obtained from OH*-chemiluminescence. Panels (d-f) shows the first three POD modes of u'_y and the extended POD modes associated with I'_P and I'_C	107
6.4	Flow and flame dynamics during Period-1 TAI with 50% hydrogen enrichment. Mean of the (a) transverse velocity component \bar{u}_x , (b) flame brush obtained from OH-PLIF images, and (c) heat release rate fluctuations obtained from OH*-chemiluminescence. Panels (d-f) shows the first three POD modes of u'_x and the extended modes associated with I'_P and I'_C	110

6.5	Flow and flame dynamics for 50% H ₂ -enriched CH ₄ -air flame. Mean of the (a) axial velocity component (u_y), (b) flame brush obtained from OH-PLIF images, and (c) heat release rate fluctuations obtained from OH*-chemiluminescence. Panels (d-f) shows the first three POD modes of u'_y and the extended POD modes associated with I'_P and I'_C	112
6.6	Mean of the (a) transverse velocity component u_x , (b) flame brush obtained from OH-PLIF images, and (c) heat release rate fluctuations obtained from OH*-chemiluminescence. Panels (d-f) shows the first three POD modes of u'_x and the extended modes associated with I'_P and I'_C . for the state of period-2 LCO with 20% hydrogen by volume of the fuel.	115
6.7	Flow and flame dynamics for 20% H ₂ -enriched CH ₄ -air flame. Mean of the (a) axial velocity component (u_y), (b) flame brush obtained from OH-PLIF images, and (c) heat release rate fluctuations obtained from OH*-chemiluminescence. Panels (d-f) shows the first three POD modes of u'_y and the extended POD modes associated with I'_P and I'_C	117
B.1	Adiabatic flame temperature (in K) with increase HFF for the operating condition $\mathcal{P} = 15$ kW and $\phi = 0.8$	131

GLOSSARY

The following are some of the commonly used terms in the thesis:

Intermittency	A dynamical state which consists of the periodic bursts amidst the aperiodic fluctuations in the acoustic pressure measured.
Lean combustion	Combustion of a fuel in the presence of more air or oxidizer than is necessary for a stoichiometric reaction to happen.
Lean premixed combustion	Lean combustion in which the mixing of fuel and air takes place before the process of combustion.
Lean premixed pre-vaporized combustion	Lean premixed combustion in which the fuel mixture is vaporized before combustion process.
Premixed combustion	Combustion of a fuel-air/oxidizer combination that has been properly mixed.
Stoichiometric combustion	The exact ratio between air and flammable gas or vapor at which complete combustion takes place.
Technically premixed combustion	Combustion of fuel that is injected into air or oxidizer flow just upstream of the flame with not enough time to mix thoroughly.
Thermoacoustic instability	A phenomenon that occurs in a confined combustion environment where a feedback between heat release rate fluctuations and pressure fluctuations resulting from laminar or turbulent flames, increasing acoustic energy and leading to large-amplitude pressure oscillations.

ABBREVIATIONS

<i>CH₄</i>	Methane
CMOS	Complementary metal-oxide semiconductor
CWT	Continuous wavelet transformation
CO1	Chaotic oscillations state-1
CO2	Chaotic oscillations state-2
CO₂	Carbon-di-oxide
EPOD	Extended proper orthogonal decomposition
<i>HFF</i>	Hydrogen fuel fraction
HRR	Heat Release Rate
<i>H₂</i>	Hydrogen
I	Intermittency
IRZ	Inner recirculation zone
ISL	Inner shear layer
LCO	Limit cycle oscillations
LPM	Lean Premixed
NO_x	Oxides of Nitrogen
NA	Non-availability
OH*	Hydroxyl radical
ORZ	Outer recirculation zone
OSL	Outer shear layer
PLIF	Planar Laser Induced Fluorescence

P1	Period-1
P2	Period-2
PMT	Photo-multiplier tube
POD	Proper orthogonal decomposition
PSD	Power spectral density
RMS	Root Mean Square
R.O.I	Region Of Interest
SPIV	Stereoscopic Particle Image Velocimetry
SLPM	Standard Litres Per Minute
TAI	Thermoacoustic instability
UHC	Unburned Hydrocarbons

NOTATION

Upper-case Latin alphabets

D_e	Diameter of exhaust duct, m
D_N	Exit diameter of nozzle, m
E	Turbulent kinetic energy
I_P	OH-PLIF intensity
I_C	OH*-chemiluminescence intensity
K	Asymptotic growth rate
L_c	Characteristic length
\mathcal{P}	Power rating, kW
Re	Reynolds number
\bar{U}	Nominal flow velocity, ms^{-1}

Lower-case Latin alphabets

$a_i(t)$	Temporal coefficients of i_{th} POD mode
d	Embedding dimension
f, f_a, f_h, f_s	Frequency, Hz
h_{CH_4}	Calorific values of methane, MJ/kg
h_{H_2}	Calorific values of hydrogen, MJ/kg
\dot{m}_{CH_4}	Mass flow rate of methane, kg s^{-1}
\dot{m}_{H_2}	Mass flow rate of hydrogen, kg s^{-1}
\dot{m}_a	Mass flow rate of air, kg s^{-1}
\dot{m}_t	Mass flow rate of total mixture, kg s^{-1}
p	Acoustic pressure, kPa
$\dot{q}(t)$	Global heat release rate signal, a.u.
u_x	Transverse component of instantaneous flow velocity, m/s
u_y	Axial component of instantaneous flow velocity, m/s
u_z	Tangential component of instantaneous flow velocity, m/s
u_{res}	Resultant flow velocity, m/s
x, y, z	Rectangular Coordinate system, m

Greek Letters

$\Delta\phi_{p'\dot{q}'}$	phase delay between $p'(t)$ and $\dot{q}'(t)$
$\Delta\phi_{a_1a_2}$	phase delay between $a_1(t)$ and $a_2(t)$
$\Delta\phi_{p'a_1}$	phase delay between $p'(t)$ and $a_1(t)$
$\Delta\phi_{p'a_2}$	phase delay between $p'(t)$ and $a_2(t)$
λ_i	i_{th} Eigenvalue
μ	Dynamic viscosity, $\text{Kg}(\text{ms})^{-1}$
ϕ	Equivalence ratio
ϕ_g	Global equivalence ratio
τ	Time delay for embedding
Ψ_i	i_{th} spatial POD mode
Ω_i	i_{th} EPOD mode

Other symbols

$(\cdot)_{rms}$	Root mean square
$(\cdot)'$	Fluctuating above mean
(\cdot)	Mean
$\langle \cdot \rangle$	Ensemble or time average
$\hat{(\cdot)}$	Normalized quantity by the global maxima of the quantity

CHAPTER 1

INTRODUCTION

The global power industry has been experiencing a persistent rise in pollutants emission as well as energy demand, necessitating the exploration of alternative fuel sources.

Over the next decade, the [International Energy Agency and Bank \(2014\)](#) has forecasted that the demand for energy will be increased by one-third of the current demand. In response, gas turbine-based aviation and power industries are actively seeking fuel alternatives while also considering factors such as fuel flexibility, availability, and adherence to international standards aimed at reducing pollution. These considerations are driven by the escalating costs associated with conventional fuels and the imperative to meet the environmental criteria ([Timagenis, 1980](#); [Julian, 2000](#); [Otto *et al.*, 2017](#); [Karakaya *et al.*, 2018](#)).

Gas turbines have become indispensable in meeting the current demand for electricity due to their exceptional attributes such as high power density, fuel flexibility, high efficiency, and favorable economics ([Jansohn, 2013](#)). To address the challenge of balancing power supply with fluctuating consumer demands, operators of gas turbines in aviation and land-based applications are actively pursuing new technologies ([Lieuwen and Yang, 2005](#)). However, these operators predominantly rely on

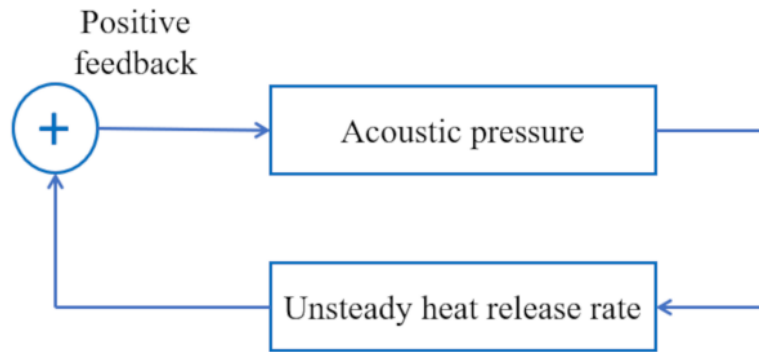


Figure 1.1: The positive feedback mechanism between the unsteady heat release rate and the acoustic field, a prerequisite for the development of thermoacoustic instability, is depicted schematically. When the system's damping is overwhelmed by the system's acoustic force (driving), thermoacoustic oscillations occur.

conventional fuels such as jet fuels, aviation gasoline, methane and liquefied petroleum gas (LPG), which generate a substantial amount of pollutants. The primary concern associated with these pollutants is the production of hazardous nitrogen oxides or NO_x. NO_x is generated during the combustion process when nitrogen from air interacts with oxygen at extremely high temperatures (Correa, 1993; Lieuwen *et al.*, 1998; Nakata *et al.*, 1998).

One strategy for mitigating NO_x emissions involves employing lean premixed (LP) combustion (Lazik *et al.*, 2008), which entails mixing the fuel with an excess amount of oxidizer (air) compared to the stoichiometric ratio prior to the combustion process. This approach reduces the temperature within the combustor, thereby suppressing NO_x formation. In some instances, LP combustion incorporates pre-vaporized fuel, referred to as lean premixed pre-vaporized (LPP) combustion, as an additional technique to

achieve lower emissions (Foust *et al.*, 2012; Yi *et al.*, 2012).

However, under lean premixed (LP) conditions, the occurrence of thermoacoustic instability becomes a significant concern (Culick and Kuentzmann, 2006).

Thermoacoustic instability refers to the emergence of large-amplitude periodic oscillations in the acoustic pressure field, facilitated by the establishment of a positive feedback mechanism (Rayleigh, 1878) between fluctuations in the acoustic pressure and the unsteady heat release rate (Poinsot *et al.*, 1987; McManus *et al.*, 1993; Pawar *et al.*, 2017; Mondal *et al.*, 2017). When the net driving force of the acoustic pressure surpasses the overall damping effects resulting from heat loss and viscous dissipation within the system, exponential growth of the acoustic pressure fluctuations ensues. Eventually, these fluctuations reach a saturation point leading to self-sustained periodic oscillations, once the driving force balances the damping characteristics of the system (Lieuwen and Yang, 2005; Juniper and Sujith, 2018). These periodic oscillations with significant amplitudes are commonly referred to as limit cycle oscillations (LCO).

The existence of these LCOs poses a threat to various combustor components, including fuel injectors and turbine blades, as the increased amplitude of acoustic pressure can lead to detrimental vibrations and damage, ultimately impairing their performance (Shanbhogue *et al.*, 2009). Furthermore, apart from the adverse effects

on component performance, the condition of thermoacoustic instability also contributes to the substantial production of carbon dioxide (Cellek and Pınarbaşı, 2018).

1.1 HYDROGEN-ENRICHED FUELS: A BETTER ALTERNATIVE

To reduce carbon emissions stemming from the combustion process, hydrogen has emerged as a highly favourable substitute for conventional hydrocarbon-based fuels.

Hydrogen exhibits remarkable potential as an alternative fuel to fossil fuels in diverse sectors such as transportation, power generation, and industrial processes, primarily owing to its clean-burning nature that culminates in the sole production of water vapour upon combustion. In pursuit of minimizing the release of diverse pollutants, certain industries endeavour to employ pure hydrogen as a fuel (Chiesa *et al.*, 2005).

Although the utilization of pure hydrogen for combustion purposes yields reduced carbon emissions, it concurrently entails augmented NO_x emissions attributable to the higher flame temperature in combustion systems (İlbas *et al.*, 2006).

The operators of gas turbine engines have demonstrated keen interest in the utilization of hydrogen-blended hydrocarbon fuels as a potential solution to address carbon and NO_x emissions challenges (Beita *et al.*, 2021). The development of gas turbine combustors utilizing hydrogen-blended fuels holds the potential for significant reductions in

greenhouse gas emissions (Schefer *et al.*, 2002), primarily attributable to the lower flame temperature achieved in such systems. To increase the combustion efficiency and decrease emissions, Sierens and Rosseel (2000) used different compositions of hydrogen and methane as fuels. Many studies have been done to study various aspects of hydrogen-enriched combustion such as lean combustion flammability enhancement (Schefer, 2003), variations in flame field (Davis *et al.*, 2013; Chtereve and Boxx, 2021) and hydrodynamic flow field (Kim *et al.*, 2009; Di Sarli *et al.*, 2012; Roy and Gupta, 2023).

1.1.1 Effect of hydrogen enrichment on flame stability

In a swirl-stabilized flame enriched with hydrogen, the influence of hydrogen addition on flame stability under fuel-lean conditions was investigated by Karbasi and Wierzba (1998). Their findings revealed that incorporating hydrogen into the hydrocarbon fuel within a swirl-stabilized premixed combustor led to a significant increase in the lean stability limit. Additionally, Schefer (2003) reported that the introduction of hydrogen widened the flammability limits in lean mixtures, enabling operation of the combustor at lower equivalence ratios. This adjustment facilitated the reduction of temperatures in the combustion zone, consequently leading to diminished NO_x emissions. Furthermore, the addition of hydrogen in the fuel blend can induce notable effects on the location

of the reaction zone within the combustor. The higher flame speed and expanded flammability range associated with hydrogen-blended fuels may cause the reaction zone to shift downstream within the combustor (Jackson *et al.*, 2003; Kim *et al.*, 2009).

1.1.2 Variation in flame speed due to hydrogen enrichment

The enrichment of H₂ results in an augmentation of the reaction rate and flame speed (Kim *et al.*, 2009), thereby profoundly altering the manner in which the flame interacts with the turbulent flow field and acoustic pressure fluctuations. Numerical investigations by Hawkes and Chen (2004) have demonstrated that the addition of hydrogen to premixed methane combustion leads to an increased turbulent burning velocity and an elevated ratio of turbulent burning velocity to laminar burning velocity. Moreover, Halter *et al.* (2007) reported the increment to the flame surface density of a Bunsen burner due to the addition of hydrogen that is also verified by Guo *et al.* (2010). Variations in flame surface density affect the flame shape in the combustor (Kuhlmann *et al.*, 2022).

1.1.3 Effect of hydrogen addition on flame shapes

The flame shape of CH₄ has also been reported to undergo a drastic change from columnar, V-shaped to M-shaped flame under H₂-enrichment (Davis *et al.*, 2013;

Taamallah *et al.*, 2015a; Shanbhogue *et al.*, 2016; Chtereve and Boxx, 2019). This observation was further supported by Chtereve and Boxx (2021), who reported the change in flame shape even at elevated pressures at various levels of H₂ enrichment. In addition, the change in flame shape due to H₂ addition strongly affects the thermoacoustic stability of the combustor. Using linear stability analysis, Oberleithner *et al.* (2015) showed that V-flames possess strong radial gradients, thus suppressing the formation of precessing vortex cores (PVC). In contrast, M-flames have smooth density gradients and lead to the formation of PVC. The presence of PVC further affects the thermoacoustic response.

1.1.4 Other effects of hydrogen enrichment

Emadi *et al.* (2012) examined the augmented burning rate of the fuel resulting from hydrogen enrichment, which also led to increased flame front wrinkles due to enhanced interaction between small-scale turbulence and the flames. Zhang and Ratner (2019) measured curvature of H₂ enriched flame and found that the addition of hydrogen causes enhancement in the flame wrinkling and the flame surface area, leading to the occurrence of thermoacoustic instability. Thermoacoustic instability has the potential to inflict structural harm upon the engines, leading to unscheduled shutdowns and financial losses (Lieuwen and Yang, 2005). Consequently, it becomes imperative to

first comprehend the fundamental attributes of TAI and subsequently investigate the impact of hydrogen addition to the fuel on the dynamics within real-world combustor systems.

1.2 THERMOACOUSTIC INSTABILITY: A COMPLEX PROBLEM

When a flame is confined within a tube or duct, it gives rise to acoustic phenomena characterized by sound generation. Initially, [Higgins \(1802\)](#) offered an explanation of the acoustic properties exhibited by a hydrogen flame enclosed within a glass duct with an open end. He called this phenomenon ‘singing flames’. Subsequently, [Sondhauss \(1850\)](#) observed sound production in a hot bulb tube that is closed-ended, attributing it to the formation of a temperature gradient within the tube. In a study by [Rijke \(1859\)](#), a metallic wire mesh was employed as a heat source positioned at the lower section of a glass tube with both ends open. The wire mesh was heated by an external flame, and upon its removal, sound was generated for a short time interval. Furthermore, the author reported that the location of the mesh wire (heat source) at a quarter length of the duct yielded sound with the maximum power. Later, the flame-heated wire mesh was substituted with an electric heater in the horizontal Rijke tube.

In 1878, Rayleigh formulated a comprehensive criterion that elucidates the mechanisms by which heat addition initiates and sustains sound generation within a Rijke tube

(Rayleigh, 1878). This criterion, known as Rayleigh's criterion, holds significant importance in determining the presence of thermoacoustic instability. Rayleigh's criteria, as stated in his own words, is as follows:

“If heat be communicated to, and abstracted from, a mass of air vibrating (for example) in a cylinder bounded by a piston, the effect produced will depend upon the phase of the vibration at which the transfer of heat takes place. If heat be given to the air at the moment of greatest condensation, or be taken from it at the moment of greatest rarefaction, the vibration is encouraged. On the other hand, if heat be given at the moment of greatest rarefaction, or abstracted at the moment of greatest condensation, the vibration is discouraged.”

Later, Putnam and Dennis (1956), and Chu (1965) formulated Rayleigh's criteria in a mathematical expression, which is given by the following equation:

$$R = \int_0^T p'(t) \dot{q}'(t) dt, \quad (1.1)$$

where R is the Rayleigh index, p' is the acoustic pressure fluctuations, \dot{q}' is the heat release rate fluctuations in the flame, t is the time, and T denotes the time period of the oscillations during the state of TAI. Early investigations into TAI explored the nonlinearities inherent in the gas dynamic processes occurring within the combustor,

which give rise to TAI. [Sterling \(1993\)](#) proposed that the presence of nonlinearities in TAI can be attributed to the unsteady heat release rate. Subsequently, [Heckl \(1988\)](#) employed a modified version of King's law ([King, 1914](#)) to comprehend the observed oscillations in a Rijke tube and developed a model for the unsteady heat release rate arising from the heated wire mesh. By considering the nonlinear effects resulting from fluctuations in the unsteady heat release rate, they successfully predicted the amplitude of acoustic pressure oscillations and implemented active control techniques to mitigate TAI within the Rijke tube. Furthermore, [Matveev and Culick \(2003\)](#) reported the occurrence of hysteresis when employing heater power as a variable. They observed that abrupt changes in acoustic pressure resulted in the generation of substantial amplitude fluctuations within the Rijke tube, consequently inducing TAI.

1.3 MECHANISMS LEADING TO THERMOACOUSTIC INSTABILITY

According to Rayleigh's criteria, thermoacoustic instability arises within a combustor when heat release rate oscillations are in phase with the acoustic pressure oscillations. During the occurrence of thermoacoustic instability, energy is fed to the acoustic field due to positive feedback between the acoustic field and the unsteady heat release rate. Various mechanisms contribute to the generation of unsteady heat release rate, subsequently leading to thermoacoustic instability in different combustion systems.

Several of these mechanisms are listed below -

1.3.1 Fluctuations in flame surface area

In various combustion systems, the combustion process occurs within a confined space. The resulting sound generated by the flame interacts with the walls of the confinement, leading to the wrinkling of the flame surface. The presence of Darrieus-Landau instability ([Landau, 1944](#)) and thermal-diffusive instabilities ([Sivashinsky, 1977](#)) induces instability in the originally laminar flame. The wrinkling of the flame surface impacts the heat release rate by augmenting the flame surface area, thereby intensifying the reaction rate.

1.3.2 Coherent structures in flow field

The investigation of coherent structure formation during the onset of thermoacoustic instability has been a prominent focus of early research endeavors. The shape of coherent structures depends on the flow velocity ([Renard *et al.*, 2000](#)). In laminar combustors characterized by low flow velocities and stable hydrodynamics, the coherent structures exhibit definite shapes ([Roos and Kegelman, 1986](#)). However, turbulent combustors, distinguished by significantly higher flow velocities, experience perturbed hydrodynamics, resulting in the irregular rotational motion of coherent structures. The elevated flow velocity in turbulent combustors necessitates the adoption of diverse flame

holding mechanisms, such as bluff-body, swirler, dump plane, etc. [Kaskan and Noreen \(1955\)](#) observed the occurrence of vortex shedding downstream of an isolated flame holder during thermoacoustic instability. Additionally, at higher modes of transverse thermoacoustic instability, [Elias *et al.* \(1959\)](#) documented the shedding of large-scale vortices emanating from the tips of flame holder.

1.3.3 Fluctuations in equivalence ratio

To mitigate the formation of NO_x, it is necessary to operate the engine at a lower average temperature in the combustor. This objective is accomplished through the implementation of lean premixed combustion techniques ([Barenblatt *et al.*, 1985](#)).

However, gas turbines utilizing lean premixed combustion often exhibit increased susceptibility to thermoacoustic instability due to their heightened vulnerability to equivalence ratio fluctuations ([Lieuwen *et al.*, 2001](#)). This susceptibility arises from the pronounced steepening of the gradient of chemical reaction time versus equivalence ratio as the flame becomes leaner ([Oates, 1978](#)). The relationship between the chemical reaction time and the reaction rate is inversely proportional, signifying that even minor deviations in the equivalence ratio under lean conditions can give rise to significant oscillations in heat release rate ([NPTELHRD, 2012](#)).

Equivalence ratio fluctuations primarily stem from fluctuations in the mass flow rates

of fuel and air. Acoustic perturbations propagate upstream, influencing the rates of fuel and airflow, thus causing fluctuations in the equivalence ratio. These fluctuations are then convected downstream into the combustion zone, contributing to the overall combustion process. The fluctuating equivalence ratio give rise to variations in both the reaction rate and the flame speed, thereby resulting in fluctuations in the heat release rate (Lieuwen *et al.*, 1998). When these fluctuations in the heat release rate occur to be in-phase with the fluctuations in acoustic pressure, it can lead to the onset of thermoacoustic instability.

1.3.4 Other mechanisms

In addition to the previously discussed factors, several other contributors to the emergence of thermoacoustic instabilities have been identified. Thermoacoustic instability is influenced by factors such as the geometric configuration of the combustion chamber, the design of the flame anchoring mechanism, and the dimensions of the air and fuel supply manifolds. These factors can affect the amplitude and frequency of the oscillations by altering the phase difference between fluctuations in heat release rate and acoustic pressure, as discussed by Candel (2002). Furthermore, the unsteady heat release rate is susceptible to the impact of velocity fluctuations at the flame anchoring point and the stretching and straining rates experienced by the flame (Lieuwen, 2021).

1.4 NONLINEAR DYNAMICS OF THERMOACOUSTIC SYSTEMS

In the regime of linear stability, the exponential growth rate of infinitesimally small perturbations can be determined through linear stability analysis. However, during the onset of TAI in the combustor, the amplitude of oscillations saturates at a finite value, indicating the presence of nonlinearity within the system (Culick, 1994). Culick and colleagues applied principles of nonlinear acoustics to elucidate the dynamics of unsteady gas flows within solid propellant rocket engines. Their work provided a theoretical framework to comprehend the phenomenon of amplitude saturation observed during thermoacoustic instability (Culick, 1994; Jahnke and Culick, 1994; Culick and Burnley, 1999). Nonetheless, their studies did not delve into the specific mechanisms that trigger the onset of instability.

Extensive research has been conducted in gas turbine combustors to investigate the nonlinear characteristics exhibited during thermoacoustic instability (Peracchio and Proscia, 1998; Lieuwen and Neumeier, 2002; Bellows *et al.*, 2007). Lieuwen (2002) focused on examining the impact of flame dynamics on this nonlinear behavior when the combustor experiences instability. In addition to pressure oscillations, numerous investigations have also addressed the phenomenon of the saturation of heat release rate oscillations during thermoacoustic instability (Balachandran *et al.*, 2005; Birbaud *et al.*,

2007).

The describing function approach has been used to investigate the nonlinear behavior exhibited by combustors during thermoacoustic instability (Kochenburg, 1950). This approach involves defining a transfer function that accounts for the frequency and amplitude of the input forcing. Dowling (1997) utilized describing function analysis to estimate the amplitudes of periodic oscillations. In their work, they incorporated nonlinearities into Bloxsidge *et al.* (1988) model, with particular emphasis on the "saturating" nature of the heat release rate as a key nonlinear factor. The saturation of the heat release rate serves as the primary source of nonlinearity in their investigations. Furthermore, Noiray *et al.* (2008) combined experimental observations with theoretical insights to predict the properties of thermoacoustic instability accurately. In addition to forecasting the amplitude and frequency of periodic oscillations, they were able to elucidate the phenomena of mode switching and triggering (Yazaki *et al.*, 1990; Sayadi *et al.*, 2014; Sujith *et al.*, 2016; Juniper and Sujith, 2018).

1.5 THERMOACOUSTIC INSTABILITY IN HYDROGEN-ENRICHED COMBUSTION

In turbulent combustors, stable operation is not characterized by acoustical silence.

The turbulent reacting flow in these systems produces broadband acoustic sound,

commonly referred to as combustion noise (Dowling and Mahmoudi, 2015). The impact of hydrogen enrichment on combustion regimes, transitioning to thermoacoustic instability from combustion noise, has been widely recognized (Janus *et al.*, 1997; Nair *et al.*, 2014; Tony *et al.*, 2015). However, in-depth investigations into these effects have only recently been conducted. In a study by Hong *et al.* (2013), it was observed that varying the hydrogen content resulted in frequency variations and changes in the flame response. These variations were attributed to the relative phase difference between the fluctuations in unsteady heat release rate and acoustic pressure.

Additionally, Palies *et al.* (2017) demonstrated a transition from stable to unstable operation through intermittent oscillations, as the equivalence ratio increased in a hydrogen-enriched low-swirl combustor. Furthermore, the dynamics of a hydrogen-enriched methane/air combustor were investigated by Zhang and Ratner (2019). They identified three distinct states: stable, conditionally unstable, and unstable. These states were found to be dependent on various levels of hydrogen enrichment and the bulk flow velocities, with hydrogen enrichment under high velocities being capable of exciting thermoacoustic instability.

Over the past decade, many researchers have extensively investigated the combustion dynamics of a technically premixed swirl turbulent burner, as known as PRECCINSTA

burner, employing both experimental approaches ([Meier *et al.*, 2007](#); [Oberleithner *et al.*, 2015](#); [Chterev and Boxx, 2019](#)) and computational methods ([Fiorina *et al.*, 2010](#); [Bénard *et al.*, 2019](#); [Filomeno *et al.*, 2021](#); [Agostinelli *et al.*, 2022](#)). These investigations aimed to comprehend various aspects of flame dynamics, vortex dynamics, fuel-air mixing and flame-acoustic coupling. In the study conducted by [Chterev and Boxx \(2019\)](#), the impact of hydrogen addition to a methane/air PRECCINSTA burner at atmospheric conditions was explored. They observed that the addition of hydrogen causes the flame to become more compact, transforming its shape from an M configuration to a V configuration.

Moreover, hydrogen enrichment influenced the dominant frequencies of unstable acoustic modes and affected the amplitude of thermoacoustic oscillations. Consequently, hydrogen enrichment can either trigger or suppress thermoacoustic instability. Recently, [Chterev and Boxx \(2020\)](#) examined the effects of hydrogen enrichment in the PRECCINSTA burner under elevated pressure conditions. They discovered that, with hydrogen addition, the amplitude of acoustic pressure oscillations during thermoacoustic instability depended on the phase delay between the Helmholtz modes and the heat release rate fluctuations within the combustor.

In swirl combustors, the addition of hydrogen has been identified as a factor capable of

shifting the system dynamics to TAI from a state of combustion noise (Janus *et al.*, 1997). The mixing of hydrogen in the fuel mixture alters the occurrence of TAI, shifting it to lower equivalence ratios while reducing the amplitude of dynamic pressure fluctuations (Figura *et al.*, 2007). These characteristics can be attributed to the inclusion of hydrogen alongside methane (CH₄), resulting in an increased reaction rate and a shorter convective time scale. Variations in hydrogen content have been found to induce changes in frequency and flame response due to alterations in the relative phase between the heat release rate and the acoustic pressure fluctuations, as reported by Hong *et al.* (2013).

Furthermore, studies such as Aesøy *et al.* (2020), have revealed a reduction in the phase difference between the heat release rate and the acoustic pressure for hydrogen-enriched fuels, highlighting the impact of hydrogen on flame transfer functions. Investigations by Lee and Kim (2020) focused on the dynamics of a mesoscale burner used for the combustion of methane and hydrogen. Their findings suggested that the dynamics were associated with higher eigenmodes during pure hydrogen operation. Additionally, several other research studies have demonstrated diverse effects of hydrogen-enrichment on combustion dynamics (Taamallah *et al.*, 2015a; Shanbhogue *et al.*, 2016; Zhang and Ratner, 2019; Chterev and Boxx, 2019). Consequently,

understanding the dynamics of hydrogen-enriched combustion in modern swirl-stabilized burners remains a topic of great interest within the scientific community. With the aim of achieving this objective, we employ a dynamical systems approach to gain a deeper understanding of the dynamics in a hydrogen-enriched combustor.

1.6 DYNAMICAL SYSTEMS APPROACH

A dynamical system refers to a system whose state undergoes temporal evolution or changes over time. These systems are commonly described by a set of difference equations (for discrete systems) or differential equations. The domain of dynamical systems theory is dedicated to comprehending the long-term qualitative behavior manifested by such systems. In recent times, there has been a growing reliance on various tools derived from dynamical systems theory, particularly nonlinear time-series analysis. This approach has revealed behaviors in various studies that extend beyond simple period-1 oscillations, uncovering intricate and complex dynamics. [Culick \(1994\)](#) used numerical continuation analysis to observe quasiperiodic oscillations in a combustor with six longitudinal acoustic modes, showcasing the richness of the system's behavior.

By employing numerical continuation methods, it is revealed that limit cycle oscillations are not the sole asymptotic state in dynamical systems ([Jahnke and Culick,](#)

1994). Remarkably, they reported, for the first time, that the occurrence of pitchfork and torus bifurcations, resulting in the emergence of quasiperiodic oscillations. The phenomenon of period doubling leading to chaotic behavior has been documented in numerical studies (Lei and Turan, 2009; Datta *et al.*, 2009).

In a laminar premixed burner, Sujith and Kabiraj (2012) conducted a comprehensive analysis of bifurcations. Their research elucidated that the onset of thermoacoustic instability in this system is associated with a Hopf bifurcation. Furthermore, variations in the flame location revealed the existence of quasiperiodicity and intermittency preceding flame blowout (Kabiraj *et al.*, 2012b). To characterize these distinct dynamical states, they used bifurcation plots, phase space reconstruction, and recurrence plots obtained from the acoustic pressure and flame dynamics acquired utilising high-speed chemiluminescence images (Kabiraj and Sujith, 2012). Similar findings, using numerical simulations, also reported by Kashinath *et al.* (2013, 2014). Using the tools of dynamical systems theory, numerous investigations have directed their focus towards comprehending the initiation of thermoacoustic instability. These studies have attributed the loss of stability of a fixed point to a Hopf bifurcation (Lieuwen, 2002; Ananthkrishnan *et al.*, 2005).

In a turbulent combustor, it has been observed that stable combustion which is

characterized by low-amplitude aperiodic pressure oscillations commonly referred to as combustion noise exhibits peculiar attributes not typically associated with conventional noise. [Nair *et al.* \(2013\)](#) conducted a series of determinism tests and proposed that combustion noise possesses determinism and exhibits chaotic behavior. This finding was further supported by [Tony *et al.* \(2015\)](#), who verified that combustion noise manifests as deterministic chaos. Additionally, [Nair *et al.* \(2014\)](#) demonstrated that the transition to thermoacoustic instability from combustion noise (state of stable operation) in a turbulent combustion chamber occurs through a dynamical state recognized as intermittency using various tools of the dynamical systems theory. Many research papers have reported the existence of intermittent oscillations experimentally ([Gotoda *et al.*, 2014](#); [Murugesan and Sujith, 2015](#); [Sampath and Chakravarthy, 2016](#); [Unni and Sujith, 2017](#)) and numerically ([Nair and Sujith, 2015](#); [Seshadri *et al.*, 2016](#)) prior to limit cycle oscillations. Furthermore, it is demonstrated that during states of TAI, the flow field exhibits periodic shedding of large-scale vortices, commonly referred to as coherent structures ([Unni *et al.*, 2018](#); [George *et al.*, 2018](#)). Dynamical systems theory was employed to unveil the multifaceted dynamical behaviors manifested within thermoacoustic systems ([Sterling, 1993](#); [Jahnke and Culick, 1994](#); [Datta *et al.*, 2009](#); [Gotoda *et al.*, 2011](#); [Kabiraj *et al.*, 2012a](#); [Nair *et al.*, 2014](#)).

1.7 MODAL DECOMPOSITION OF THERMOACOUSTIC SYSTEMS

The presence of coherent structures plays a significant role in shaping the overall thermoacoustic characteristics of turbulent combustors (Poinsot *et al.*, 1987; Sterling and Zukoski, 1987; Schadow and Gutmark, 1992), as these structures exert significant influence over the flow behavior. In-depth investigations employing techniques such as spark-Schlieren imaging and C_2 radiation mapping have enabled the tracking of coherent structure formation, growth, and decay. These structures profoundly impact the mixing process between the unburnt fuel-air mixture and the burnt hot gases. The mutual synchronization between acoustic pressure fluctuations and the periodic shedding of coherent structures is one of the fundamental mechanisms during the emergence of thermoacoustic instability (Poinsot *et al.*, 1987; Pawar *et al.*, 2017; George *et al.*, 2018).

For analysing coherent patterns in turbulent flow, the proper orthogonal decomposition (POD) approach is widely recognized as one of the most significant techniques (Lumley, 1967; Sirovich, 1987). This method entails reducing turbulent flow fields into orthogonal modes, which are derived by optimizing either the L^2 -norm or the kinetic energy of the velocity field. These POD modes possess orthogonality and serve to characterize the dominant coherent structures that contain the majority of the turbulent

kinetic energy. In various systems exhibiting thermoacoustic stability, the relationship between coherent structures and pressure variations has been investigated with POD.

[Sui et al. \(2017\)](#) employed the proper orthogonal decomposition (POD) method to gain insights into the behavior of acoustic fluctuations, specifically the different eigenmodes, in a spatial context. They accomplished this by reconstructing the two-dimensional pressure field of a Rijke tube. Through their analysis, they observed 1:1 and 2:1 coupling phenomena among various filtered modal coefficients. This coupling behavior was investigated using traditional Lissajous patterns, which are axisymmetric patterns employed as a representation method for a pair of signals. The frequency locking behavior of the signal pair, indicative of their ratio of the dominating frequencies, can be deduced from these patterns ([Greenslade Jr, 1993](#)). In another study by [Boxx et al. \(2010\)](#), the POD technique was utilized to investigate the phenomenon of precessing vortex core (PVC). Their analysis revealed that in the most energetic mode, the dominant vortices exhibited a counter-clockwise rotation. Conversely, in the second mode, the dominating vortices rotated in a clockwise direction. By leveraging the information extracted from the POD modes, the researchers proposed that the first two dominant modes corresponded to a helical PVC, while the third mode was associated with axial thermoacoustic pulsation.

In the field of fluid dynamical systems, where strong coupling exists between subsystems, comprehending the impact of coherent structures on other correlated variables is crucial. To address this correlations between structures, [Borée \(2003\)](#) introduced the extended proper orthogonal decomposition (EPOD). This approach enables the projection of other correlated variables, such as concentration, temperature, and so on, onto the POD modes of the velocity field. As a result, analogous flow structures can be obtained in these correlated variables, aiding in the understanding of the interplay between coherent structures and other associated variables. [Duwig and Iudiciani \(2010\)](#) used the extended proper orthogonal decomposition (EPOD) technique to investigate the correlation between modes in the reacting flow field and the unsteady flame. This analysis was conducted using planar laser-induced fluorescence (PLIF) data obtained from an acoustically excited flame. The EPOD method allowed for a comprehensive examination of the relationship between these modes, shedding light on the intricate dynamics of the flame. Furthermore, EPOD has been applied in various thermoacoustic systems to explore the influence of coherent structures on correlated modes of related variables such as pressure, temperature, and scalar concentrations (specifically OH* and CH* intensity fields) ([Sieber *et al.*, 2017](#); [Wang *et al.*, 2019](#); [Lohrasbi *et al.*, 2021](#)). With this, it is important to understand how the coherent structures couple with the structures from other fields such as flame surface and heat

release rate distribution.

1.8 OBJECTIVES OF THE THESIS

In summary, the presence of thermoacoustic instability presents a significant challenge in the development of practical combustors utilizing lean hydrogen-enriched fuel combustion (Beita *et al.*, 2021). So far, the limit cycle oscillations in hydrogen enriched turbulent combustors have been largely studied using tools based on linear theory (Sierens and Rosseel, 2000; Schefer *et al.*, 2002). However, given the notable presence of nonlinear characteristics, such as triggering and limit cycle oscillations, in hydrogen-enriched combustion (Emadi *et al.*, 2012; Taamallah *et al.*, 2015b; Palies *et al.*, 2017), a comprehensive examination of various dynamical states in a hydrogen-enriched combustor has not been previously conducted. Additionally, the progressive increment of hydrogen within the fuel composition introduces changes to the system dynamics that have not yet been explored from the perspective of nonlinearity in the combustion system.

The current understanding of coupled interactions within various dynamical states is primarily limited to the coupled behaviour between fluctuations in the acoustic pressure and the heat release rate (Pawar *et al.*, 2018; Mondal *et al.*, 2018). However, in technically premixed turbulent combustors exhibiting thermoacoustic instabilities, the

flow field plays a vital role, as evidenced by the emergence of coherent structures (Unni *et al.*, 2018). The investigation of the correlation between coherent structures from the flow field and dominant structures derived from the heat release rate distribution during the period-1 oscillations is conducted using the extended version of proper orthogonal decomposition (EPOD) (Sieber *et al.*, 2017). However, an extensive exploration to elucidate the correlations between the coherent structures in the flow velocity field and the dominant structures derived from the flame surface and the heat release rate distribution has yet to be conducted.

In the present work, the experiments were done in a laboratory-scale swirl stabilised partially premixed combustor. We then, use the tools from the dynamical systems theory to analyse the temporal and spatiotemporal data obtained from these experimental datasets provided by Dr. Isaac Boxx, to achieve the following objectives of the thesis:

1. We characterize different dynamical states that arise as a result of hydrogen enrichment of the fuel, using the time series analysis of the fluctuations in acoustic pressure at the combustion chamber of a technically premixed swirl-stabilized combustor.
2. Additionally, we study the spatiotemporal dynamics during various dynamical states using the high-speed snapshots of the flow, the flame and the heat release rate distribution using various imaging techniques.
3. We investigate the transition of dynamical states from one thermoacoustic state having period-2 limit cycle oscillations to another thermoacoustic state with period-1 limit cycle oscillations through chaotic state oscillations with successive increment of hydrogen in the fuel using the analysis based on nonlinear time series.
4. We examine frequency locking behaviour between the acoustic pressure and the

heat release rate fluctuations during different states of thermoacoustic oscillations in hydrogen-enriched combustion using various tools from the synchronization theory.

5. Subsequently, we present a framework to understand the coupled interaction of acoustic pressure, heat release rate and flow velocity fluctuations temporally. Furthermore, we investigate how the dominating coherent structures from the flow velocity field correlate with the dominant structures from the flame and heat release rate distribution during different dynamical states in the combustion chamber.

1.9 OVERVIEW OF THE WORK

The remaining chapters of the thesis are summarized here. **Chapter 2** summarizes the description of the experimental setup and provides the details of the measurement techniques used to obtain the datasets, we used in the present study. In **Chapter 3**, we discuss different methodologies used in this study to calculate the dominant POD modes of the flow field and EPOD modes of OH-PLIF and OH*-chemiluminescence images. To determine the chaotic behaviour in a signal qualitatively, we study and perform the 0-1 test.

Chapter 4 provides the details of different dynamical states observed due to the addition of hydrogen in the fuel. We explore five different dynamical states in this study: chaotic oscillations (chaotic oscillations states-1 and chaotic oscillations states-2), intermittency and thermoacoustic instabilities (period-1 limit cycle oscillations and period-2 limit cycle oscillations). We explain the characteristics of each dynamical

states using different analyses such as time series, fast Fourier transformation (FFT), phase portrait and scalogram. Along with the characteristics of each dynamical states, we also study variation in the flow, flame and heat release rate distribution. Further, we investigate the transition of P2-LCO to P1-LCO through the state of CO-2 due to the addition of hydrogen in the fuel while maintaining a constant global equivalence ratio and thermal power.

Chapter 5 details about the frequency locking between different temporal signals for the states of thermoacoustic instabilities. Using different analyses such as time series analysis, first return map and spectrum of the signals, we investigate the frequency locking behaviour between the fluctuations in the acoustic pressure and the heat release rate. Subsequently, with the help of phase portrait and phase difference between two signals, we extend the concept of frequency locking among the acoustic, the heat release rate and the hydrodynamic field using the temporal coefficients of dominating POD modes. We observe 1:1 and 2:1 frequency locking during the states of thermoacoustic instabilities.

In **Chapter 6**, we study the correlation between the coherent structures of the flow field and the structures from simultaneously acquired OH-PLIF and OH*-chemiluminescence fields. **Chapter 7** summaries the major results from this study. **Appendices** include

the procedures for the calculation of global equivalence ratio (A.1), nominal Reynolds number A.3, dynamics viscosity (A.4) and computation of adiabatic flame temperature (B) due to addition of hydrogen in the fuel.

CHAPTER 2

EXPERIMENTAL FACILITIES

The experiments described in this thesis were performed in a laboratory-scale turbulent combustor with a conical centerbody acting as the flame-stabilizing mechanism. The data-sets were provided by Dr. Isaac Boxx of the German Aerospace Center (DLR), located in Stuttgart, Germany, originating from the experiments conducted by his research team under the project known as *Hyburn*. The objective of this project is to facilitate transportation to a reliable and cost-effective energy system based on carbon-free renewable power generation. Initially, the acoustic pressure fluctuations and the heat release rate fluctuations were measured in the combustion chamber. The experimental setup has an optical accessibility to the combustion chamber, enabling to observe the performance of flow seeding that investigate the dynamics of the flame and the flow in various combustor dynamical states.

2.1 EXPERIMENTAL SETUP

The experimental investigations were performed under atmospheric pressure conditions using a technologically advanced gas turbine model combustor (PRECCINSTA configuration) shown in Fig. 2.1. Here, PRECCINSTA stands for PREdiction and

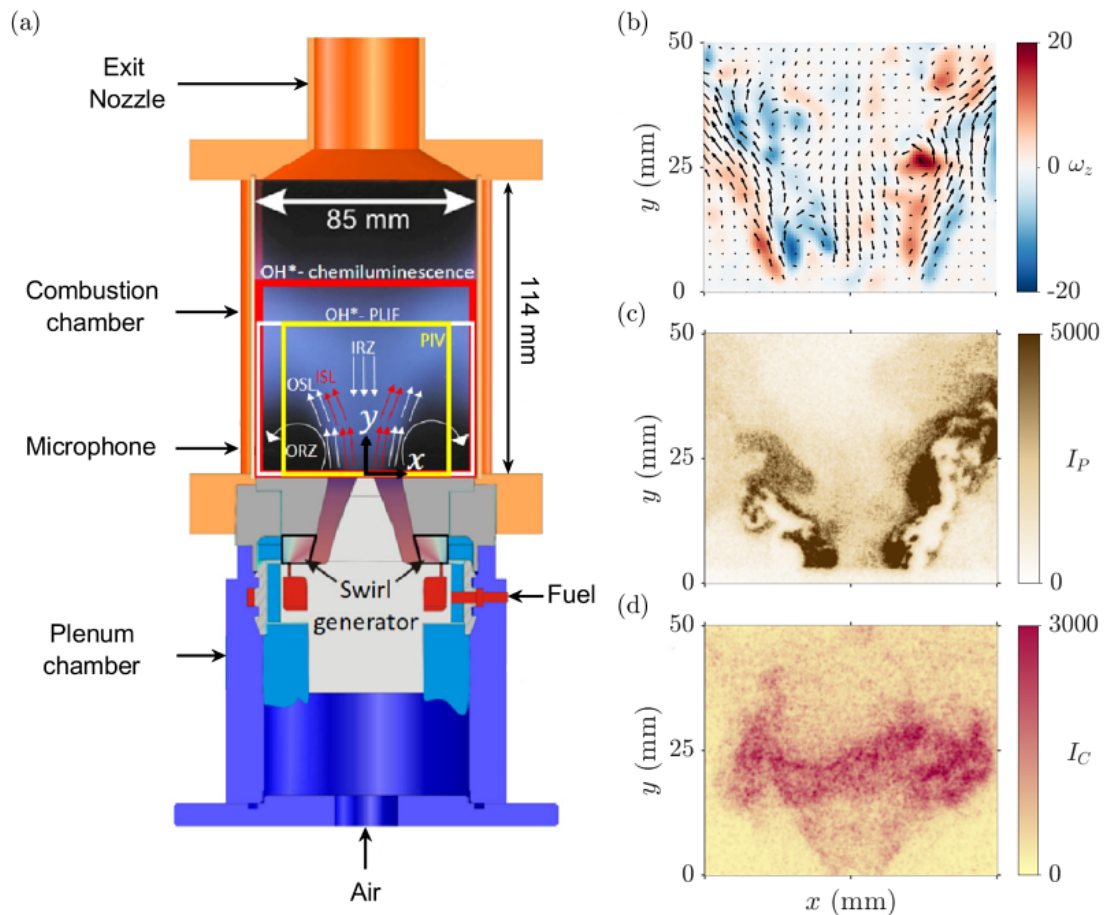


Figure 2.1: (a) Schematic of the experimental setup of the technically premixed gas turbine model combustor. Different regions and shear layers are indicated with the abbreviations which are: OSL - Outer shear layer, ISL - Inner shear layer, ORZ - Outer recirculation zone and IRZ - Inner recirculation zone. Different coloured rectangles indicate the regions captured by different image-capturing techniques. Instantaneous (b) vorticity field, (c) OH-PLIF intensity showing the flame area, and (d) OH*-chemiluminescence field showing the heat release rate distribution are also shown for reference

Control of Combustion INSTAbilities in industrial gas turbines. The PRECCINSTA combustor features a cylindrical plenum through which air is introduced and subsequently directed through a swirl generator comprising 12 radial channels. Fuel, specifically methane with varying levels of hydrogen admixture, is injected into the swirl channels through orifices measuring 1 mm in diameter. The resulting flow of

swirling, partially premixed reactants then enters the combustion chamber via a nozzle characterized by an exit diameter (D_N) of 27.85 mm. Notably, this nozzle incorporates a conical centerbody. The combustion chamber possesses a square cross-section measuring $85 \times 85 \text{ mm}^2$ and a height of 114 mm. To facilitate optical observations, the chamber is equipped with side walls constructed from quartz glass, firmly held in place by metal posts positioned at the corners. The exit configuration of the combustor consists of a conical contraction followed by an exhaust duct with an inner diameter (D_e) of 40 mm.

2.2 ACOUSTIC SIGNAL ACQUISITION

Pressure signals originating from the combustion chamber were meticulously captured to gain insights into the dynamics of combustion. The pressure in the chamber was measured employing precision amplitude and phase-calibrated microphone probes, each equipped with B&K Type 4939 condenser microphones. The location of the probes involved situating one within the plenum and the other within the combustion chamber at a specific elevation of $y = 20 \text{ mm}$. To ensure synchronous data acquisition, a multichannel analog-to-digital (A/D) converter with a sampling frequency of 100 kHz was utilized. Notably, this study exclusively focused on analyzing the acoustic pressure signals acquired precisely at the inlet of the combustion chamber.

2.3 OPTICAL MEASUREMENTS

In order to study the effect of hydrogen enrichment on the flow and flame dynamics, different imaging techniques have been used. Using these imaging techniques, snapshots have been acquired simultaneously along with the acoustic signals to understand the variations with the changes in the acoustic pressure in the combustion chamber.

2.3.1 Stereoscopic particle image velocimetry (SPIV)

The quantification of three velocity components in a plane aligned with the center-line of the burner was accomplished through the utilization of stereoscopic particle image velocimetry (SPIV) methodology. This involved the implementation of a stereo-PIV system comprising a dual-cavity, diode-pumped solid-state laser (Edgewave, IS200-2-LD, capable of delivering up to 9 mJ/pulse at 532 nm) and a pair of CMOS cameras (Phantom v1212) positioned on opposing sides of the laser sheet, oriented towards the combustor chamber. For each operational state, a total of 10,000 PIV images were captured at a resolution of 640×800 pixels. The projected pixel resolution of the PIV system was 0.08 mm/pixel. The measurement domain of the PIV encompassed a region measuring $65 \times 50 \text{ mm}^2$, ($-32 < x < 32 \text{ mm}$ and $0 < y < 50 \text{ mm}$ in Fig. 2.1). A temporal separation of 10 ms (Δt) was chosen between consecutive frames. To

shape the laser beam into a sheet, a pair of cylindrical lenses ($f = -38$ mm and 250 mm) were employed, while a third cylindrical lens ($f = 700$ mm) was implemented to reduce its thickness at the focal point. In order to facilitate flow visualization, titanium dioxide particles with a nominal diameter of $1 \mu\text{m}$ were introduced into the airflow. The image mapping, calibration, and cross-correlation algorithm were performed using a commercial multi-pass adaptive window offset cross-correlation technique (LaVision DaVis 10). The final interrogation window size and overlap were set to 16×16 pixels and 50%, respectively, corresponding to a window size of 1.3 mm and a vector spacing of 0.65 mm. Based on correlation statistics obtained from DaVis, the estimated uncertainty in the instantaneous velocities was approximately 0.7 m/s for the in-plane components ($x - y$) and around 1.8 m/s for the out-of-plane component (z -axis).

2.3.2 OH*-Chemiluminescence

The line-of-sight integrated chemiluminescence arising from the self-excited OH* radical was visualized using an intensified high-speed CMOS camera (LaVision HSS 5 with LaVision HS-IRO). The camera was equipped with a fast UV objective lens (Halle, with a focal length (f) of 64 mm and an aperture of $f/2.0$) and a bandpass filter (300-325 nm) to selectively capture the desired wavelengths. The chemiluminescence was imaged over a resolution of 512×512 pixels. To accommodate varying signal

intensities, the intensifier gate time of the camera ranged from 25 to 50 μs . The camera's built-in memory allowed for the recording of 8192 frames in each capture, enabling a comprehensive dataset for analysis. The primary objective of OH-chemiluminescence images is to identify the region of high heat release rate distribution by detecting Hydroxyl radical (OH) in the combustor (He *et al.*, 2019; Liu *et al.*, 2020). To determine the global heat release rate (\dot{q}'), the intensity of all pixels in the captured frames was integrated, providing an overall measure of the local heat release rate released during combustion.

2.3.3 OH - planar laser-induced fluorescence (PLIF)

The OH-PLIF imaging system employed in this thesis utilized a frequency-doubled dye laser, pumped by a high-speed, pulsed Nd:YAG laser (Edgewave IS400-2-L, 150 W at 532 nm and 10kHz) and an intensified high-speed CMOS camera system. The dye laser system (Sirah Credo) generated an output power of 5.3 to 5.5 W at a wavelength of 283 nm, with a repetition rate of 10 kHz, resulting in a pulse energy of approximately 0.53-0.55 mJ. For excitation, the dye laser was tuned to target the $Q_1(6)$ line of the $A^2 \Sigma^+ - X^2 \Pi$ ($v'=1, v''=0$) band. Continuous monitoring of the laser wavelength during the experiments was achieved using a photo multiplier tube (PMT) equipped with WG-305 and UG-11 filters, along with a premixed, laminar reference flame. To

create an approximately 50 mm (high) \times 0.2 mm (thick) laser sheet for PLIF excitation at a wavelength of 283 nm, three fused-silica cylindrical lenses, all coated with anti-reflective material to maximize transmission, were utilized. The OH-PLIF and SPIV (stereoscopic Particle Image Velocimetry) systems had their laser sheets overlapped by passing the green (532 nm) PIV sheet through the final turning mirror of the OH-PLIF setup.

The OH-PLIF fluorescence signal was captured using a high-speed CMOS camera (LaVision HSS6) and an external two-stage intensifier (LaVision HS-IRO) positioned opposite to the OH camera relative to the combustor. An additional fast UV objective lens (Cerco) with a focal length (f) of 45 mm and an aperture of $f/1.8$, along with a bandpass filter (300-325 nm), were attached to the OH-PLIF camera. The camera had an array size of 768×768 pixels, resulting in a projected pixel resolution of 0.115 mm/pixel. The OH-PLIF images covered a measurement domain spanning the entire width ($-42.5 < x < 42.5$ mm) and extended axially from $0 < y < 50$ mm. The objective of OH-PLIF imaging in combustion is to visualize and quantify the distribution of OH radicals, which are important markers for heat release and flame structure (Ryan *et al.*, 2009). OH-PLIF is used to study flame structure, combustion dynamics, and the characteristics of turbulent jet flames (Singla *et al.*, 2006).

		$\phi = 0.65$			$\phi = 0.8$		
\mathcal{P} (kW) (\rightarrow)		10.5	15.6	20.8	10.5	15.6	20.8
HFF (\downarrow)							
0%		CO1	P2	P2	CO1	P2	P2
10%		I	P2	P2	CO1	P2	CO2
20%		P1	P2	P2	CO1	CO2	CO2
30%		P1	P2	P2	CO1	CO2	CO2
40%		P1	P2	I	I	CO2	CO2
50%		P1	P2	P1	I	P1	CO2
60%		P1	CO2	NA	I	P1	CO2
70%		P1	CO2	NA	I	CO2	NA
80%		P1	CO2	NA	NA	CO2	NA

Table 2.1: Different dynamical states observed by increasing HFF (%) for $\mathcal{P} = 10.5$ kW, 15.6 kW, and 20.8 kW for $\phi_g = 0.65$ and 0.8. The expanded forms of the abbreviations used in the table are provided in the Abbreviations section (see pages xix-xx). NA refers to non-availability of data at that conditions due to the breakage of the quartz window allowing optical access to the combustor.

Simultaneously, at a sampling rate of 10 kHz, the OH*-chemiluminescence, OH-PLIF, and stereo-PIV images were acquired together with the microphone measurements, ensuring synchronized data capture across multiple diagnostic techniques.

2.4 OPERATIONAL CONDITIONS

Data were collected at three thermal load conditions, $\mathcal{P} = 10.5, 15.6$ and 20.8 kW. and two equivalence ratios, $\phi_g = 0.65$ and 0.8 (see Table 2.1). The thermal power shown in the Table 2.1, is the mean value of the thermal powers for each column, using the calculations given in Appendix A.2. The equivalence ratio and thermal power are maintained constant by appropriate mass balancing amongst the reactants. For each combination of thermal load and equivalence ratio, the fraction of hydrogen in the fuel

was varied from 0 – 80%, in increments of 10%. Apart from these conditions, three data sets were acquired at $\mathcal{P} = 25.3$ kW and $\phi_g = 0.65$ with hydrogen variation of 0% (CO1), 20% (CO1) and 40% (CO1), which are not shown in table 1. This gives a parameter space of 51 operational test conditions.

The hydrogen fuel fraction (FFF) can be defined as, $FFF = \dot{V}_{H_2}/(\dot{V}_{H_2} + \dot{V}_{CH_4})$.

Here, \dot{V}_{H_2} and \dot{V}_{CH_4} represent the standard volume flow rate in hydrogen and methane, respectively. Hereon, low/high FFF implies that the volume flow rate of hydrogen is less/more than that of methane. Various dynamical states result in a parameter space of many operational test circumstances, however, several of dynamical states elicited powerful thermoacoustic pulsations that shattered the glass of the combustion chamber, making measurement impossible.

CHAPTER 3

METHODOLOGIES FOR ANALYSES

In this chapter, we will discuss different methods to analyze the experimental data obtained from Dr. Isaac Boxx. To understand nonlinear behaviour of the temporal data, we have used the reconstructed phase-space, power spectrum and continuous wavelet transformation. For identifying the characterizing features of different dynamical states, we also investigated the high-speed images, acquired applying various techniques. We have examined the instantaneous images for defining features such vortices, ISL, OSL, IRZ, ORZ. We have also used a data-driven method (proper orthogonal decomposition and its extended version) to understand the coupled interaction between the dominating structures from different spatial data acquired simultaneously.

3.1 NONLINEAR TIME SERIES ANALYSIS (NTSA)

Nonlinear time-series analysis (NTSA) represents one of the most efficient techniques available for comprehending the characteristics of nonlinear time series data (Small, 2005; Kabiraj and Sujith, 2012). NTSA, which originated in the 1980s from dynamical systems theory, has evolved significantly and found applications in examining various engineered and natural phenomena, such as electronic circuits (Hegger *et al.*, 1998),

aerodynamic flutters (Perets *et al.*, 2018), and hydrodynamically self-excited jets (Li and Juniper, 2013), wakes (de Paula and Möller, 2018) and flames (Zhou *et al.*, 2017).

3.1.1 Phase-space reconstruction

It is mentioned in the Introduction (chapter 1) of this thesis that TAI manifests as high amplitude acoustic oscillations in different thermoacoustic systems. In most physical systems, the state variables, which are the minimum set of variables that fully describe the state of a system mathematically, are either unknown or cannot be measured directly. Due to the unavailability of sufficient state variables, the phase space cannot be constructed. In general, acoustic pressure which is a scalar time series, is measured in different thermoacoustic systems. By using Taken's time-delay embedding theorem (Takens, 1981), time series data of the acoustic pressure fluctuations can be used to reconstruct the phase space to understand the global dynamics of the dynamical systems.

In NTSA, there are mainly two parameters used for the reconstruction of phase-space (Small, 2005; Kabiraj and Sujith, 2012). The first parameter is the time delay (τ) for embedding. Although τ can theoretically assume any value, it is crucial to carefully select an appropriate value for practical applications in order to optimize the unfolding of an attractor (Milnor, 1985). An attractor is a collection of numerical values which

asymptotically attracts or repels any neighbouring trajectories that cross across its basin of attraction. Selecting a small value of τ encourages strong correlation among the elements of the reconstructed phase space, resulting in their accumulation along the diagonal of the embedding space. Conversely, if τ is assigned a large value, the elements of the reconstructed phase space become more susceptible to noise, resulting in random correlations among these elements. This occurrence emerges due to the increased time lag between neighboring points in the time series, causing their dynamics to diverge further and occupy distinct regions in the phase space. Therefore, careful selection of the appropriate τ in NTSA is crucial for obtaining a meaningful representation of the underlying attractor structure, balancing the trade-off between excessive noise and excessively compact dynamics in the reconstructed phase space.

To determine the optimal value of τ , there are various methods by utilising the value of the lag where auto-correlation (AC) function crosses the first zero ([Small, 2005](#); [Kabiraj and Sujith, 2012](#)) or where the average mutual information (AMI) function attains its first local minima with respect to different lags ([Fraser and Swinney, 1986](#)). In our studies, since the AMI function can take into consideration both linear and nonlinear correlations, it is preferred over the auto-correlation function. For a time series $p'(t)$ having a total number of N point, the AMI can be calculated by -

$$I(\tau) \equiv \sum_{t=1}^N Pr(p'(t), p'(t + \tau)) \log_2 \left[\frac{Pr(p'(t), p'(t + \tau))}{Pr(p'(t))Pr(p'(t + \tau))} \right] \quad (3.1)$$

where, $Pr(p'(t))$ and $Pr(p'(t + \tau))$ are the marginal probabilities, and $Pr(p'(t), p'(t + \tau))$ is the joint probability of observing $p'(t)$ and $p'(t + \tau)$.

The second important parameter is the embedding dimension (d). The original phase space is projected onto the embedding dimension of the hyperspace. It is necessary to have a suitably large dimension in which the attractor is unfolded. To ensure the existence of true neighbours of each trajectory in the reconstructed phase space, removing the false crossings is crucial. To ensure the optimal embedding dimension, there are many methods such as false nearest neighbour (FNN) ([Kennel *et al.*, 1992](#)) and Cao's method ([Cao, 1997](#)).

In order to calculate the minimum embedding dimension (d), we first understand the false nearest neighbouring (FNN). The fundamental concept underlying this method is to mitigate spurious crossings of phase space trajectories, which can result from the projection of a higher-dimensional original attractor onto a lower-dimensional reconstructed phase space, rather than being indicative of inherent dynamics. To eliminate the false crossing of the phase space trajectories, the FNN method quantifies the closeness, measured by Euclidean distances, between neighboring points along

a trajectory in a given dimensional space and compares it with the subsequent dimensional space. If the ratio of these distances exceeds a predefined threshold, attributed to a change in dimensionality, the trajectory's neighbors are identified as false neighbors (Kennel *et al.*, 1992). The chosen threshold value must be sufficiently large to enable the exponential divergence of the chaotic signal. Typically, in practical applications, the threshold value is selected within the range of 10 to 50 (Abarbanel *et al.*, 1993).

Consider an attractor with dimension d , a time delay of T , and let $y^{(r)}$ represent the r^{th} nearest neighbour of the reconstructed vector $y(n)$. The computation involves determining the square of the Euclidean distance between the points $y(n)$ and $y^{(r)}(n)$,

$$R_d^2(n, r) = \sum_{k=1}^d [x(n + kT) - x^{(r)}(n + kT)]^2, \quad (3.2)$$

where $y(n) = [x(n), x(n + T); \dots; x(n + (d + 1)T)]$ and $n = 1, 2, \dots, N - (d - 1)T$.

In the $(d+1)$ dimensional space, the separation between these points is determined as follows:

$$R_{d+1}^2(n, r) = \sum_{k=1}^{d+1} [x(n + kT) - x^{(r)}(n + kT)]^2. \quad (3.3)$$

On arranging the terms,

$$R_{d+1}^2(n, r) = R_d^2(n, r) + [x(n + kT) - x^{(r)}(n + kT)]^2, \quad (3.4)$$

An augmented Euclidean distance between $y(n)$ and $y^{(r)}(n)$ upon transitioning from dimension d to $(d+1)$ indicates that the specified neighbour is deemed a false neighbour within the d -dimensional space. The criterion to detect false neighbours:

$$\frac{[R_{d+1}^2(n, r) - R_d^2(n, r)]^{1/2}}{R_d^2(n, r)} = \frac{|x(n + dT) - x^{(r)}(n + dT)|}{R_d(n, r)} > R_T \quad (3.5)$$

where R_T represents a threshold that determines the erroneous nature of the nearest neighbors.

For the determination of the minimum embedding dimension, [Cao \(1997\)](#) proposed a function $E(d)$ which involves the dimension (d) and the optimum time lag (τ),

$$E(d) = \frac{1}{N - d\tau} \sum_{i=1}^{N-d\tau} \frac{\|P'_i(d+1) - P'_{n(i,d)}(d+1)\|}{\|P'_i(d) - P'_{n(i,d)}(d)\|}, \quad (3.6)$$

where $\|\circ\|$ is the Euclidean distance, and $n(i, d)$ is the index for which $P'_{n(i,d)}(d)$ is the nearest neighbour of $P'_i(d)$. The minimum embedding dimension is the threshold value of d at which the ratio $E1(d) = E(d+1)/E(d)$ converges to 1.

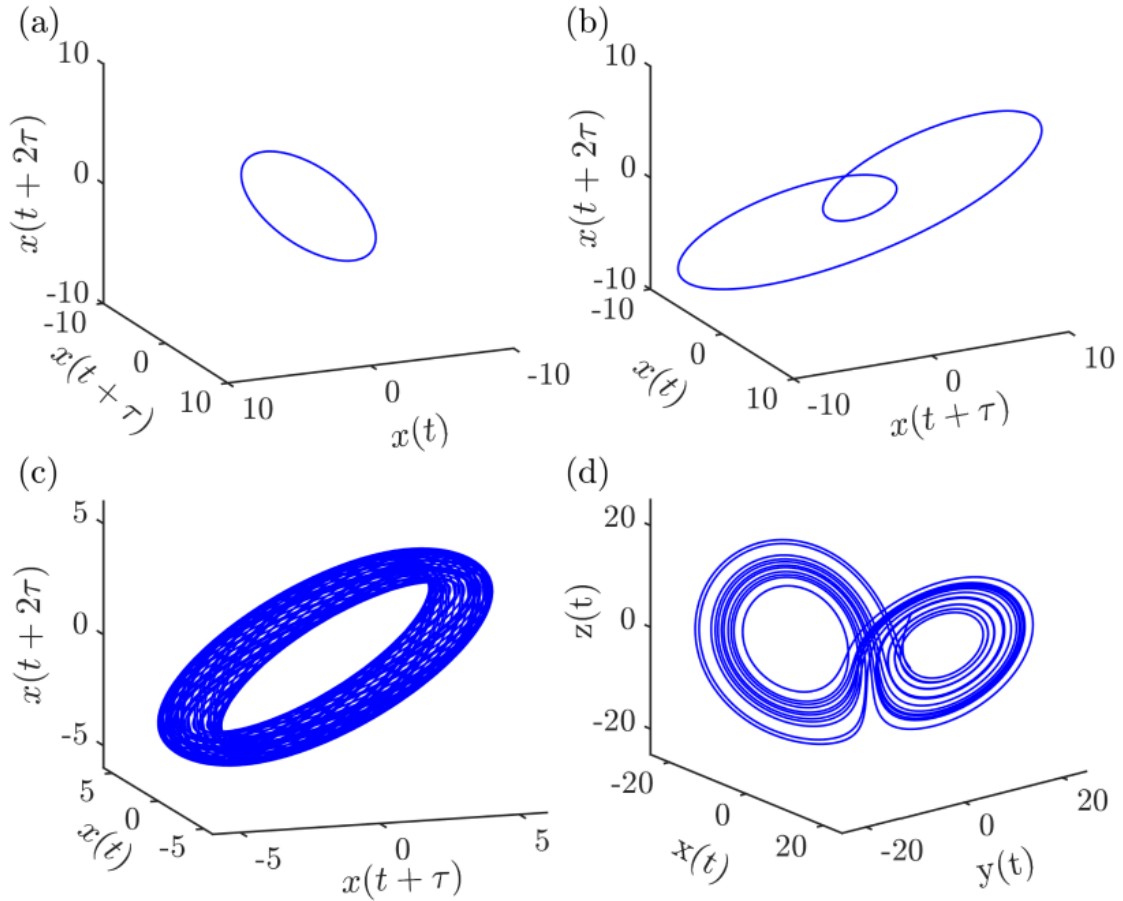


Figure 3.1: 3-dimensional phase portrait of (a) period-1, (b) period-2, and (c) quasi-periodic signals using sinusoidal waves, and (d) Lorenz attractor are obtained through phase space reconstruction.

In this study, the FNN method is used, that is based on calculating the percentage of erroneous crossings for an embedding dimension. If this percentage does not fall to zero since the dimension is insufficient for reconstructing the phase space, a higher dimension will be needed. The optimum embedding dimension is the dimension for which this percentage approaches zero. [Kabiraj *et al.* \(2012a\)](#) employed the FNN method to determine the minimal embedding dimension of the acoustic pressure signals for the investigation of a thermoacoustic system.

Once the optimal values of the time delay and embedding dimension have been determined, the next step involves performing phase-space reconstruction for different dynamical states. Various phase portraits for different kinds of signal are shown in Fig. 3.1. For period-1 and period-2 signals (Fig. 3.1a,b), we observe a single loop and a double loop attractor, respectively in phase space. However, the non-repeating trajectories of quasi-periodic signal occupy the surface of a torus (Fig. 3.1c). For chaotic signal, Lorenz attractor is shown in Fig. 3.1d, exhibiting a butterfly shaped structure in phase space.

3.2 OTHER METHODS FOR ANALYSIS

In addition to phase space reconstruction, we also employed power spectrum analysis and continuous wavelet transformation (CWT) to investigate the nonlinear behavior in our experimental data. These methods provide complementary information about the time-frequency characteristics of the data, which can be used to better understand the underlying dynamics.

3.2.1 Power spectrum

The power spectrum, also known as the power spectral density (*PSD*), is a mathematical representation of the distribution of power or energy contained within

a signal as a function of frequency. It provides information about the frequency content and the relative strength of different frequency components present in a given signal.

The following steps are used to calculate the power spectrum of a given time series $x(t)$ having a total number of N points:

Step 1. By leveraging the property of Parseval's theorem (Mitra, 2001), the time-domain signal can be transformed into the frequency domain through the utilization of Discrete Fourier Transform (DFT),

$$\sum_{t=1}^N |x(t)|^2 = \frac{1}{N} \sum_{f=0}^{N-1} |X(f)|^2 \quad (3.7)$$

where $X(f)$ is the discrete Fourier transform of $x(t)$. Here, t is time index of the time series $x(t)$ and f is frequency index of $X(f)$. The MATLAB[®] `fft` function is used to compute the fast Discrete Fourier Transform of the temporal signals of the acoustic pressure oscillations.

Step 2. Multiply both sides of the above by $\frac{1}{N}$:

$$\frac{1}{N} \sum_{t=1}^N |x(t)|^2 = \frac{1}{N^2} \sum_{f=0}^{N-1} |X(f)|^2 \quad (3.8)$$

Step 3. $|x(t)|^2$ is the instantaneous power of the time signal. So the left side of the

equation (3.8) is just the average power of the signal over the N samples. Then, for each DFT bin, we can say,

$$P_{bin}(f) = \frac{1}{N^2} \sum_{f=0}^{N-1} |X(f)|^2 \quad (3.9)$$

Here, P_{bin} is the power spectrum of the time signal.

Step 4. If $x(t)$ is real, then $X(f)$ is symmetric about $f_s/2$, with each side containing half of the power. Here, f_s is the sampling frequency of the signal. In that case, we can choose to keep just the one-sided spectrum (with positive values of frequencies), and multiply P_{bin} by 2,

$$\text{one-sided } P_{bin}(f) = \frac{2}{N^2} \sum_{f=0}^{N-1} |X(f)|^2 \quad (3.10)$$

In summary, the power spectrum provides a quantitative description of the power or energy distribution across different frequencies within a signal. It is obtained by applying the Fourier transform to the signal and calculating the squared magnitude of its frequency domain representation. Using the aforementioned steps, we have calculated the power spectrum for our experimental data and described for different dynamical states.

3.2.2 Continuous wavelet transform (CWT)

To understand the spectral behaviour of the time series with better localization of coarse and fine frequency components at different instants, continuous wavelet transform (CWT) is used (Torrence and Compo, 1998). “Wavelet transform is known as a mathematical microscope, which provides a multi-resolution analysis of the data under consideration” (Gharekhan *et al.*, 2010). The CWT allows a stationary as well as non-stationary time signal to be represented at multiple scales for different windows of the time signal. This window is known as wavelet (Shoeb and Cliord, 2005). In addition to translating the time signal into frequency domain, CWT also allows for window lengthening or shortening based on wavelet scale that emphasises that the sensitivity to changes in frequency increases as the scale is lowered. The CWT is described by:

$$C(a, \tau) = \int \frac{1}{\sqrt{s}} \psi\left(\frac{t - \tau}{s}\right) x(t) dt \quad (3.11)$$

where C is the transformation, τ is the translation time, s is the scale factor, $x(t)$ is the time series and ψ is the wavelet function.

In order to analyze the data, the CWT changes the analysis window size and modifies its temporal and frequency resolution automatically. The term ‘scalogram’ refers to the

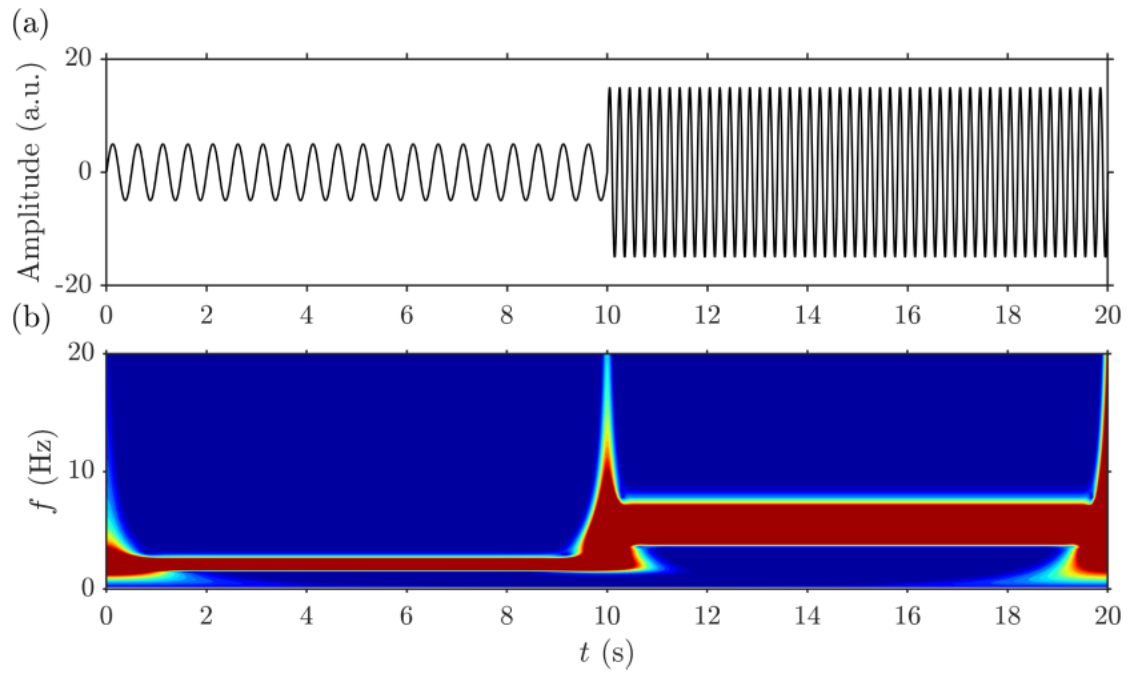


Figure 3.2: (a) Sinusoidal waves with two different frequencies (2 Hz and 5 Hz) for different time intervals and, (b) the corresponding scalogram are shown.

graphical representation that depicts the correlation between the signal and the wavelets scaled throughout time using the absolute value of the continuous wavelet transform coefficients of the signal (Shoeb and Cliord, 2005). The scalogram of the signal $x(t)$ is defined by:

$$S(s, \tau) = |C(s, \tau)|^2 \quad (3.12)$$

Applying the above analysis, we have analyzed the experimental data to plot the scalograms for different dynamical states using the MATLAB[®] `cwt` function. In figure 3.2(a), a time series with two frequencies (2 Hz and 5 Hz in the left and right halves respectively) is shown. The corresponding scalogram is calculated using the equations 3.11 and 3.12. In scalogram (Fig. 3.2(b)), there are two spectral bands: one at 2 Hz

for half time-interval and one at 5 Hz for remaining time interval. At the middle, the transition between the signal can also be noticed.

3.3 PROPER ORTHOGONAL DECOMPOSITION (POD)

Proper orthogonal decomposition (POD) is a data-driven modal decomposition technique to reduce large-scale, high-dimensional processes or datasets into low-dimensional deterministic modes. POD involves decomposing snapshots of space and time-dependent observables into orthogonal modes, sorting them based on their energy, and extracting the spatial structures. Here, we use the snapshot POD method suggested by [Sirovich \(1987\)](#). It has a spatial average operator to extract coherent structures from the time-resolved snapshots of fields such as velocity, pressure, temperature and concentration. The method uses \mathbf{L}^2 norm for classifying the modes, which is equivalent to the fluctuating kinetic energy for the velocity field ([Sieber *et al.*, 2017](#)) and the variance of the OH*-chemiluminescence.

The velocity fluctuations (u') can be decomposed in terms of the spatial modes (ψ_i) and temporal modes (\mathbf{a}_i) in the following manner:

$$u'(x, y, t) := u(x, y, t) - \bar{u}(x, y) := \sum_{i=1}^N \mathbf{a}_i(t) \Psi_i(x, y), \quad (3.13)$$

where, \bar{u} refers to the time average of the instantaneous velocity field $u(x, y, t)$ where N is the number of images for velocity field, m and n represent the number of rows and columns in each image. Here, we reshape each image as a row and form a two-dimensional matrix that has a size of $N \times (m \times n)$. Each snapshot is considered to be an element of the square-integrable vector field $\mathbf{L}^2(\xi)$ specified in the Hilbert space. The class of square-integrable functions is unique for compatibility with an inner product, which allows notions like angle and orthogonality. The inner product of two vector $\boldsymbol{\alpha}$ and $\boldsymbol{\beta}$ fields in the Hilbert space is defined as

$$(\boldsymbol{\alpha}, \boldsymbol{\beta})_{\xi} = \int_{\xi} \boldsymbol{\alpha} \cdot \boldsymbol{\beta} d\boldsymbol{x}, \quad (3.14)$$

where \boldsymbol{x} denotes a point in a spatial domain $\xi \subset \mathbf{R}^3$, and the corresponding norm $\|\boldsymbol{\alpha}\|_{\xi}$ is given by

$$\|\boldsymbol{\alpha}\|_{\xi} := \sqrt{(\boldsymbol{\alpha}, \boldsymbol{\alpha})_{\xi}}. \quad (3.15)$$

Usually, the number of spatial points is much higher than the number of snapshots. So, we quantify the relation between individual snapshots by formulating the correlation matrix $\mathbf{R}_{(N \times N)}$

$$R_{i,j} := \frac{1}{N} \left[\mathbf{u}'(\mathbf{x}, t_i), \mathbf{u}'(\mathbf{x}, t_j)^T \right]. \quad (3.16)$$

Here, each snapshot is stored in $\mathbf{x} = x_i$ after reshaping from size $(m \times n)$, and T indicates the transpose of the matrix. The matrix \mathbf{R} has a size of $N \times N$.

Using eigenvalue decomposition, we calculate the eigenvalues and eigenvectors of the correlation matrix \mathbf{R}

$$\mathbf{R}\mathbf{a}_i = \lambda_i \mathbf{a}_i. \quad (3.17)$$

The matrix \mathbf{R} possesses eigenvalues that are both real and non-negative, denoted as $\lambda_i \geq 0$. To simplify the analysis, we assume that the eigenvalues are arranged in descending order: $\lambda_1 \geq \lambda_2 \geq \lambda_3 \geq \dots \geq \lambda_N$, without any loss of generality. The eigenvectors \mathbf{a}_i are called the temporal coefficients and follow the orthogonality condition

$$\frac{1}{N} \sum_{k=1}^N \mathbf{a}_i(t_k) \mathbf{a}_j(t_k) = \lambda_i \delta_{ij}, \quad (3.18)$$

where, δ_{ij} is the Kronecker Delta function.

Using the projection of the snapshots on the temporal coefficients, the spatial modes are obtained as

$$\Psi_i(\mathbf{x}) = \frac{1}{N\lambda_i} \sum_{j=1}^N \mathbf{a}_i(t_j) u'(\mathbf{x}, t_j). \quad (3.19)$$

Sr. No.	H ₂ (%)	Re($\times 10^4$)	ϕ_g	\mathcal{P} (kW)	p'_{rms} (kPa)	Dynamical state
1	0	2.41	0.65	25.31	0.09	Chaotic
2	20	2.74	0.65	22.26	0.91	P2 LCO
3	50	2.64	0.65	22.50	0.71	P1 LCO

Table 3.1: The values of different operating parameters during the experiments. Keys: H₂(%) - Volumetric percentage of H₂ in the fuel; Re - Nominal Reynolds number; ϕ_g - Global equivalence ratio; \mathcal{P} - Thermal power rating (kW) and dynamical states. The experimental cases analysed here are shown.

The spatial modes are orthogonal by constructions. After reshaping $\Psi_i(\mathbf{x})$, we can get spatial modes $\Psi_i(x, y)$ having m and n as rows and columns, respectively. In order to study the coherent structures and their coupled behaviour with the structures from other fields such as OH-PLIF and OH*-chemiluminescence, we select specific cases showing different dynamical states, tabulated in the table 3.1.

3.4 EXTENDED PROPER ORTHOGONAL DECOMPOSITION (EPOD)

In addition to investigating coherent flow structures, POD method has been utilized to investigate the correlations between the coherent structures from the flow velocity field and the dominating structures from other measured quantities such as concentration, temperature, or pressure. The extended POD analysis, initially introduced by Borée (2003), facilitates this capability. The principal objective of employing EPOD methodology is to provide a common basis for the dominant structures from OH-PLIF and OH*-chemiluminescence fields (Antoranz *et al.*, 2018). This establishment enables

a comparative analysis of the spatial distribution of the dominant structures of the flame surface and the heat release rate distribution fields in correlation with the structures derived from the dominant Proper Orthogonal Decomposition (POD) modes inherent to the flow velocity field. The absence of a common basis precludes the comparison of dominant structures across two or more spatiotemporal datasets, even if acquired simultaneously.

To elucidate this concept further, let us consider a collection of intensity field, denoted as $I(\mathbf{x}, t)$, which are simultaneously measured alongside the velocity field $u(\mathbf{x}, t)$. The intensity field $I(\mathbf{x}, t)$ can be decomposed into an average component $\bar{I}(\mathbf{x}, t)$ and a fluctuating part $I'(\mathbf{x}, t)$

$$I(\mathbf{x}, t) = \bar{I}(\mathbf{x}) + I'(\mathbf{x}, t). \quad (3.20)$$

Similar to the spatial modes $\Psi(\mathbf{x})$ of velocity, a set of extended POD modes $\Omega_i(\mathbf{x})$ is now defined as:

$$\Omega_i(\mathbf{x}) = \frac{1}{N\lambda_i} \sum_{j=1}^N \mathbf{a}_i(t_j) I'(\mathbf{x}, t_j), \quad (3.21)$$

where $\mathbf{a}_i(t_j)$ are the temporal coefficients computed using the POD of velocity fields.

[Sieber *et al.* \(2017\)](#) showed that the part of the simultaneously measured field (I) that

is correlated with the spatial modes of velocity could be obtained by the product of the temporal coefficients of the spatial modes of velocity and the spatial mode of $I'(\mathbf{x}, t)$.

3.5 HILBERT TRANSFORM AND ANALYTICAL SIGNALS

Proper orthogonal decomposition (POD) and extended POD analysis are used to quantify the spatial extent of the flow and the flame structures. These methods decompose the data into a set of orthogonal modes, each of which represents a spatial structure. The temporal interactions of these spatially extended modes are equally important, and we quantify these interactions based on their synchronization characteristics. This is achieved by time series analysis of the POD temporal coefficients along with pressure and global heat release rate fluctuations.

We compute the instantaneous phase using the concept of analytic signals and by utilizing the Hilbert transform (Rosenblum *et al.*, 1996). For a given signal $x(t)$ normalized by its global maxima, the instantaneous amplitude $A(t)$ and phase $\phi(t)$ can be obtained from the complex analytic signal

$$\xi(t) = x(t) + i\mathcal{H}(x(t)) = A(t) \exp(i\phi(t)), \quad (3.22)$$

where $A(t)$ and $\phi(t)$ denote the instantaneous amplitude and phase of the analytic

signal, respectively. The Hilbert transform is $\mathcal{H}(x(t)) = 1/\pi \int_{-\infty}^{\infty} x(\tau)/(t - \tau)d\tau$, where the integral is evaluated at the Cauchy principle value. The analytic nature of temporal coefficients is verified for different states by plotting the phase space trajectory of $\xi(t)$ and adjudging its center of rotation. For periodic signals, there is a unique center of rotation, allowing us to uniquely specify the phase of the signal. As instantaneous phase is a monotonically increasing or decreasing quantity, it is first wrapped to the interval $[-\pi, \pi]$. Finally, synchronization among pairs of signals are evaluated by measuring the instantaneous phase difference: $\Delta\phi_{x_1, x_2} = \phi_{x_1}(t) - \phi_{x_2}(t)$. Signals are considered to be phase locked when the difference $\Delta\phi_{x_1, x_2}$ becomes bounded to a small interval ϵ ($\leq 2\pi$) around the mean phase C , to with $|\Delta\phi_{x_1, x_2}(t) - C| = |\phi_{x_1} - \phi_{x_2} - C| \leq \epsilon$ (Pikovsky *et al.*, 2001).

The temporal interactions of the identified structures are further visualised using the phase portraits or Lissajous plots for pair of signals. The exact relation between the temporal signals are inferred based on the dominant frequencies (f_1, f_2) of the signals and the mean phase difference ($\Delta\phi_m$). This is done by constructing the pair of analytical signals based on superposition of the dominant frequencies,

$$\begin{aligned}
 x_1 &= A_1 \sin(2\pi f_1 t + \Delta\phi_m) + A_2 \sin(2\pi f_2 t + \Delta\phi_m), \\
 x_2 &= B_1 \sin(2\pi f_1 t) + B_2 \sin(2\pi f_2 t),
 \end{aligned}
 \tag{3.23}$$

where, f_1 is the dominating frequency of the signal and f_2 is the multiple of f_1 , i.e., $f_2 = 2f_1$. A_1, A_2, B_1 and B_2 are the amplitudes associated with the dominant modes f_1 and f_2 for different pair of signals.

3.6 QUANTIFYING CHAOTIC BEHAVIOR OF TEMPORAL DYNAMICS

In order to quantify the chaotic time evolution of coherent structures, we perform 0 – 1 test which quantifies the unbounded growth of phase space trajectories typical of chaos (Gottwald and Melbourne, 2004). For any input time series $\gamma(t)$, the first step is to compute the translation variables $x(n)$ and $y(n)$ such that

$$x(n) = \sum_{j=1}^n \gamma(t) \cos(tc), \quad y(n) = \sum_{j=1}^n \gamma(t) \sin(tc) \quad (3.24)$$

where, $n = 1, 2, \dots, N$, where N denotes the number of the data points in the temporal signal. For our analysis, we have selected the value of c in the interval $(\pi/5, 4\pi/5)$ (Nair *et al.*, 2013). The behavior of these two translation variables helps in determining the existence of chaos in the system. For periodic or quasi-periodic oscillations, the variables show bounded behavior. However, for chaotic dynamics, their behavior is unbounded and irregular. The behavior of the trajectory in the $x - y$ plane for increasing n can be computed with the help of modified mean square displacement $M(n)$ as follows (Ashwin *et al.*, 2001):

$$M(n) = \frac{1}{N} \sum_{j=1}^n [(x(j+n) - x(j))^2 + (y(j+n) - y(j))^2] - \frac{1}{N} \sum_{j=1}^n \gamma(t) \frac{1 - \cos(jc)}{1 - \cos(c)} \quad (3.25)$$

For a chaotic state, the displacement $M(n)$ between the translational variables grows monotonically with n , while it becomes nearly constant for regular states. The asymptotic growth rate (K) of the mean displacement is computed with the help of linear regression, as follows:

$$K = \lim_{n \rightarrow \infty} \frac{\log M(n)}{\log n}. \quad (3.26)$$

[Gottwald and Melbourne \(2009\)](#) pointed that for the small values of n , the linear regression methods results in altering the K values. To estimate the K value, we use a correlation method which performs better than the linear regression method. In this method, K is the correlation coefficients for the vectors

$$\zeta = (1, 2, 3, \dots, n)^T \quad (3.27a)$$

and

$$\Delta = (M(1), M(2), M(3), \dots, M(n))^T \quad (3.27b)$$

The correlation coefficient can be defined as

$$K = \text{corr}(\zeta, \Delta) = \frac{\text{cov}(\zeta, \Delta)}{\sqrt{\text{var}(\zeta)\text{var}(\Delta)}} \in [-1, 1] \quad (3.28)$$

Here,

$$\text{cov}(\zeta, \Delta) = \frac{1}{n} \sum_{j=1}^n (\zeta(j) - \bar{\zeta})(\Delta(j) - \bar{\Delta}), \text{var}(\zeta) = \text{cov}(\zeta, \zeta),$$

and

$$\bar{\zeta} = \frac{1}{n} \sum_{j=1}^n \zeta(j).$$

The value of K resides within the range of 0 and 1. In the case of a chaotic signal, K tends to approach 1, while for a regular signal, it tends to approach a value closer to 0.

CHAPTER 4

CHARACTERIZATION OF DYNAMICAL STATES AND TRANSITION DUE TO H₂ ENRICHMENT

In this chapter, we study the effect of hydrogen addition on the dynamics of a swirl-stabilized combustor for two equivalence ratios and three thermal powers. We perform a detailed characterization of each dynamical state observed in the combustor. Later, we study the transition between different states of thermoacoustic instabilities through the state of chaotic oscillations. We observe that the addition of hydrogen in the fuel alters the combustion dynamics significantly. This is reflected in the occurrence of several rich dynamical states in the acoustic pressure fluctuations (p') of the combustor. In Table. [2.1](#), we have shown the different dynamical states observed in the p' signal due to an increase in HFF in the fuel under different operating conditions.

When the combustor is operated at low thermal power ($\mathcal{P} = 10.5$ kW) for both $\phi_g = 0.65$ and 0.8, we observe the emergence of periodic acoustic oscillations with the enrichment of H₂ in the fuel. We notice the presence of low amplitude chaotic state-1 oscillations (CO1), low amplitude P1 LCO, and intermittency for increasing HFF . As the thermal

This chapter is published in A. Kushwaha, K. Praveen, Samadhan A. Pawar, R. I. Sujith, I. Chtere, and I. Boxx (2021). Dynamical characterization of thermoacoustic oscillations in a hydrogen-enriched partially premixed swirl-stabilized methane/air combustor. *Journal of Engineering for Gas Turbines and Power*, **143**(12): , 121022 (11 pages)

power is increased to a higher value ($\mathcal{P} = 15.6$ kW), for values of $\phi_g = 0.65$ and 0.8 at 0% *HFF*, we observe the simultaneous excitation of two modes (f_1 and f_2 being the frequency of the two modes, respectively) in the system. As these modes are rationally related to each other in a ratio of $f_1/f_2 = 2$, we refer to them as period-2 (P2) LCO. For $\phi_g = 0.65$, we notice that the system stays in the state of P2 LCO for lower *HFF*; however, it exhibits chaotic state-2 (CO2) oscillations for higher *HFF*. In contrast, at a higher value of $\phi_g = 0.8$, the system shows P2 LCO for lower *HFF*, that transition to P1 LCO via chaotic oscillations (CO2) as *HFF* is increased. We observe only CO2 oscillations at higher *HFF*. At the higher thermal power ($\mathcal{P} = 20.8$ kW) and $\phi_g = 0.65$, the system exhibits low amplitude chaotic oscillations (CO1) for lower *HFF*, while P2 LCO and P1 LCO are noticed at higher *HFF*. For $\phi_g = 0.8$, we notice CO2 oscillations in the acoustic pressure at all hydrogen enrichment levels.

Thus, the overall comparison of the results for different operating conditions suggests that the addition of H_2 to the fuel at different operating conditions generates or suppresses thermoacoustic instabilities, or leads to the complex dynamics resulting from the interaction of modes in the combustor.

Now, we perform a detailed characterization of the temporal dynamics in the combustor using the time series of acoustic pressure fluctuations. Additionally, we also study the

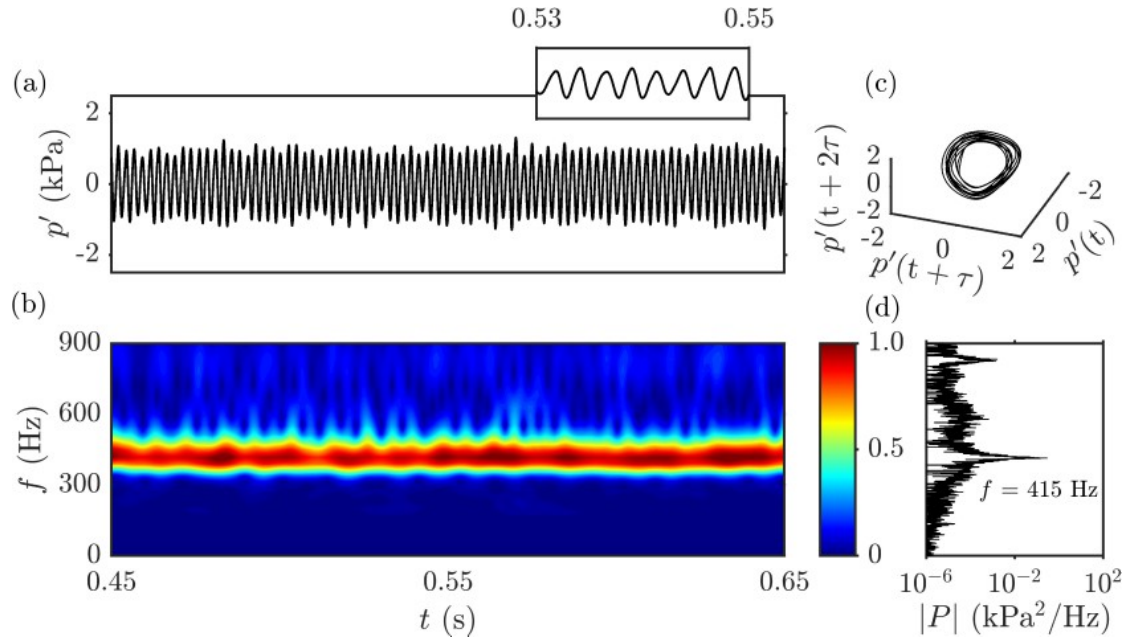


Figure 4.1: (a) The time series (b) scalogram, (c) three-dimensional phase space, and (d) power spectrum of p' during the state of P1 LCO, observed for $\mathcal{P} = 20.8$ kW, $\phi_g = 0.65$, $HFF = 50\%$, and $Re = 2.64 \times 10^4$.

flow and flame dynamics corresponding to key dynamical states observed in the system due to hydrogen enrichment in the fuel.

4.1 PERIOD-1 LIMIT CYCLE OSCILLATIONS

Initially, we discuss the most common state of thermoacoustic instability that is characterized by period-1 oscillations and observed in various appliances like gas turbine engines, rocket engines etc. Figure 4.1a represents the p' signal observed when the system operates at the condition of TAI. During this dynamical state, we observe the presence of large amplitude periodic oscillations. The power spectrum of this signal exhibits a dominant peak at 415 Hz and a small magnitude peak at its super harmonic observed at 830 Hz (Fig. 4.1d). The periodic oscillations having a single dominant

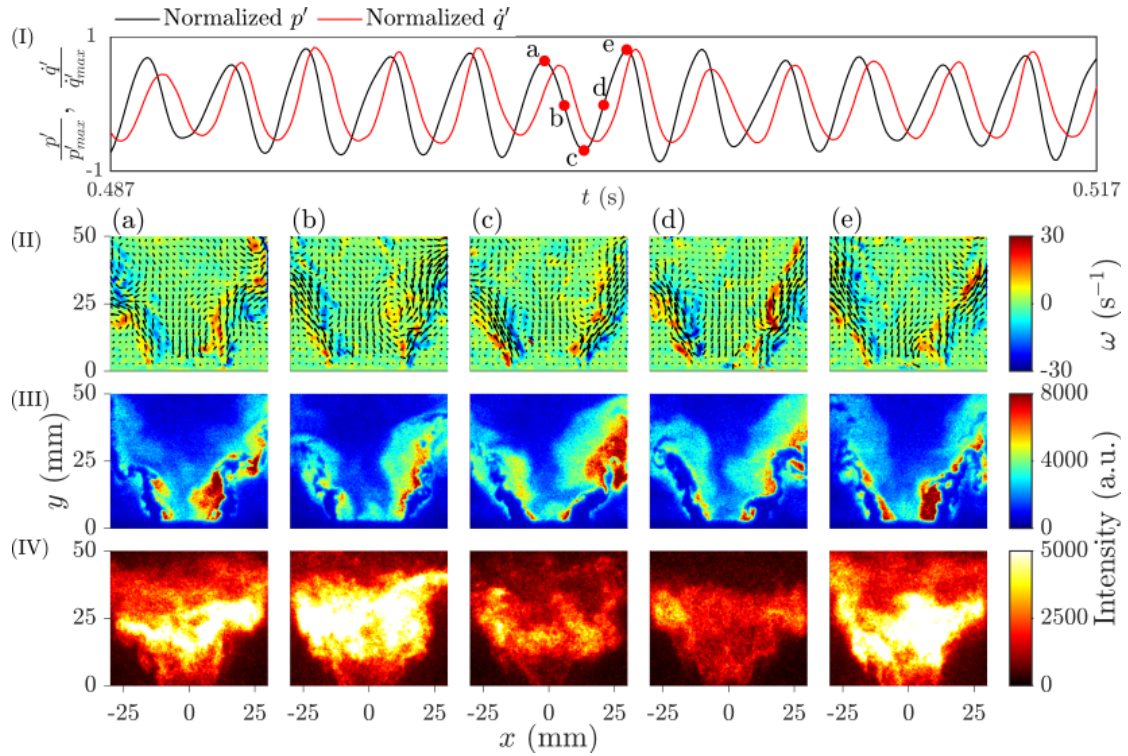


Figure 4.2: (I) The overlapped time series of normalized p' and q' fluctuations during the state of P1 LCO. The instantaneous (II) PIV images, (III) OH-PLIF images, and (IV) OH*-chemiluminescence images corresponding to five instants (a-e) over a cycle of p' signal are shown.

frequency is further confirmed by the corresponding scalogram (Fig. 4.1b), which shows the presence of a constant range of high magnitude for 415 Hz throughout the signal. The reconstructed phase space of this state shows a ring-like structure (Fig. 4.1c), typically observed for P1 LCO (Kabiraj *et al.*, 2012a).

The normalized p' and q' signals show a phase difference of around 28° , indicating the presence of in-phase synchronous oscillations during the state of P1 LCO (Fig. 4.2I).

This behaviour is in accordance with the Rayleigh criterion (Rayleigh, 1878). During this state, we observe large-sized vortices shed periodically along the ISL in the flow

field (Fig. 4.2II). We observe significant intensity variations in the flame stabilized in the region between the ISL and OSL along the two branches (Fig. 4.2III), as the pressure amplitude varies between its maxima to minima. When the pressure amplitude is near its maxima (Fig. 4.2Ia), we observe nearly a symmetric generation of vortices in ISLs from the dump plane (Figs. 4.2IIa,e) and a very high flame intensity in the flow field (Figs. 4.2IVa,b). The flame is wider and appears asymmetric across all time instants (Fig. 4.2III). As the pressure goes from minima to maxima (Figs. 4.2Ic-e), we notice a pronounced wrinkling along the flame (see Fig. 4.2IIId) as the vortices convect downstream. Simultaneously, we also notice an increase in the flame intensity from its minima to maxima (Figs. 4.2IVc-e). This flame behavior is observed to repeat for each cycle.

4.2 PERIOD-2 LIMIT CYCLE OSCILLATIONS

Apart from the most widely studied P1 LCO characterized by a single timescale in swirl combustors (Gotoda *et al.*, 2014; Pawar *et al.*, 2018), we also observe the presence of limit cycle oscillations characterized by two dominant timescales (Fig. 4.3) in our system. We refer to such oscillations as period-2 limit cycle oscillations. During this state, we notice the repetition of the signal behaviour for every two cycles of oscillations. The power spectrum of this state shows two frequencies ($f_1 = 283$ Hz,

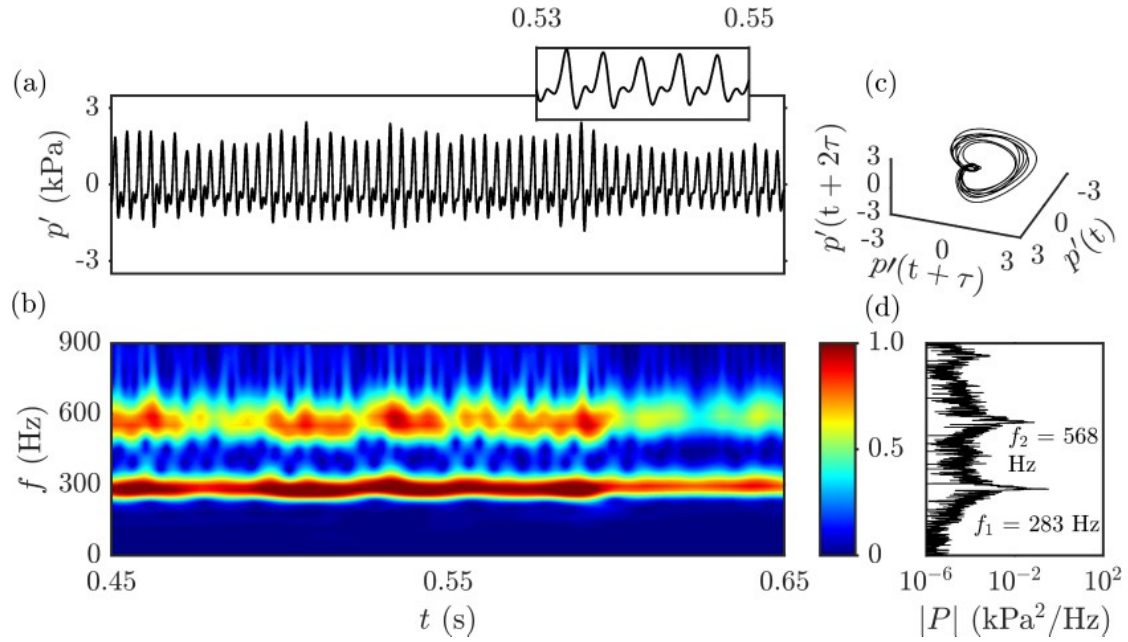


Figure 4.3: (a) The time series, (b) scalogram, (c) three-dimensional phase space, and (d) power spectrum of p' signal during the state of P2 LCO observed for $\mathcal{P} = 20.8$ kW, $\phi_g = 0.65$, $HFF = 20\%$, and $Re = 2.72 \times 10^4$.

$f_2 = 568$ Hz, and $f_2/f_1 \approx 2$) of comparable amplitudes (Fig. 4.3d). From the scalogram plot (Fig. 4.3b), we observe that these two frequencies are continuously present in the signal. However, the amplitude at $f_2 = 568$ Hz is time-varying, while $f_1 = 283$ Hz exhibits a near constant amplitude throughout the signal in the scalogram (Fig. 4.3b). Such behavior could lead to variable amplitude loading in the combustor (Suresh, 1998). In the corresponding phase space of this state (Fig. 4.3c), we observe that the phase space trajectory performs a smaller inner loop for every revolution around the bigger outer loop, typical of P2 LCO (Kabiraj *et al.*, 2012a).

During P2 LCO state, we observe notable alterations in the flow and flame dynamics in comparison to those observed during the P1 LCO state. When the pressure amplitude

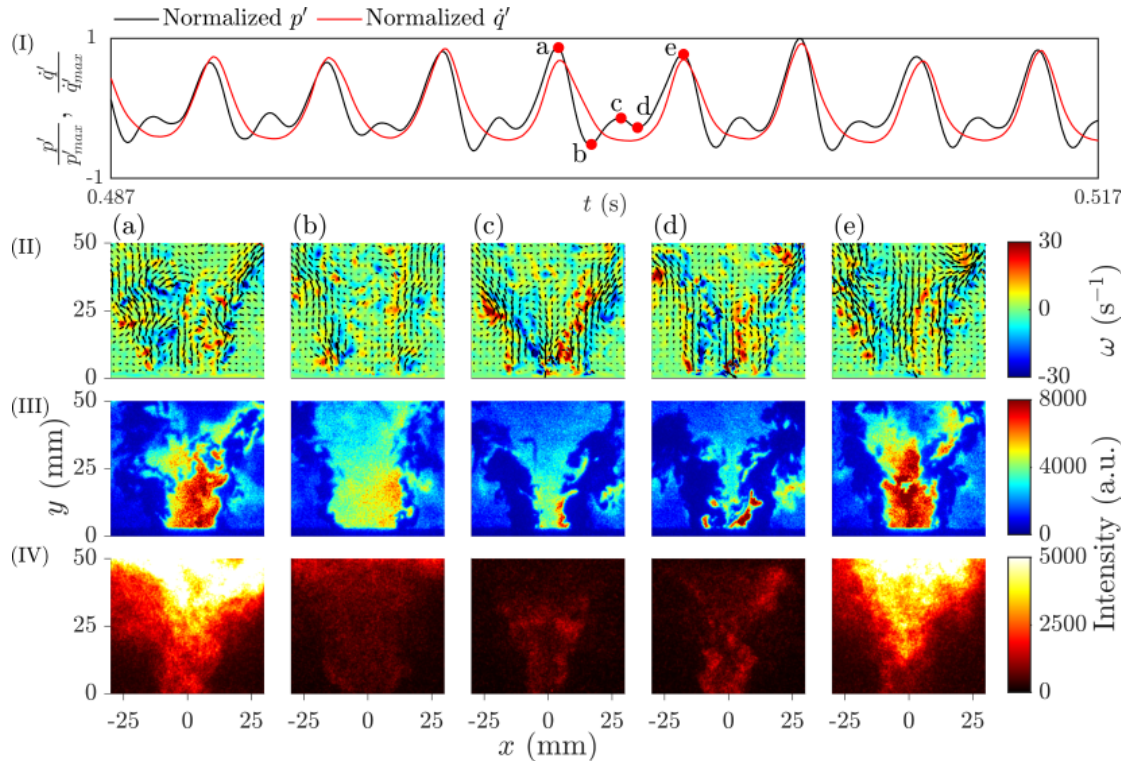


Figure 4.4: (I) The overlapped time series of normalized p' and q' fluctuations during the state of P2 LCO. The instantaneous (II) PIV, (III) OH-PLIF, and (IV) OH*-chemiluminescence images corresponding to five instants (a-e) over a cycle of the p' signal are shown.

is at the first local maxima (point a in Fig. 4.4I), we notice that most of the heat release rate happens far downstream of the inlet of the combustion chamber (Fig. 4.4IVa). The distribution of OH-field is observed to be very high near the inlet in the IRZ of the flame (Fig. 4.4IIIa). As the pressure approaches the first local minima (point b in Fig. 4.4I), the heat release rate is low in the combustion chamber (Fig. 4.4IVb). The corresponding distribution of OH-field appears to be nearly uniform in the central plane (Fig. 4.4IIIb). As the pressure reaches the second local maxima and the second local minima (points c and d in Fig. 4.4I), the flame exhibits a thin jet-like structure (Figs. 4.4IVc,d), while we see low concentration of OH-field scattered over small regions (Figs. 4.4IIIc,d). The

PIV images of the flow field show that when the pressure is at the first local minima (Fig. 4.4IIb), a vortex is shed along the OSL from the dump plane. This vortex then grows to its maximum size as the pressure reaches the second local minima (Fig. 4.4IIc). After this instant, this vortex breaks down and causes an increase in the local heat release rate in the system, coinciding with the pressure maxima (Fig. 4.4IIe). This behavior of the flame repeats for every two oscillation cycles in the system.

4.3 INTERMITTENCY

In Fig. 4.5, we show the state of intermittency observed in the combustor. The state of intermittency, as described by [Nair *et al.* \(2014\)](#), is distinguished by the presence of epochs featuring low amplitude aperiodic oscillations interspersed with bursts of large-amplitude periodic oscillations. These occurrences appear to transpire in a seemingly random manner (Fig. 4.5a). Such oscillations have been reported in many turbulent thermoacoustic systems previously ([Nair *et al.*, 2014](#); [Nair and Sujith, 2015](#); [Pawar and Sujith, 2018](#); [Dutta *et al.*, 2019](#); [Aoki *et al.*, 2020](#)). The scalogram (Fig. 4.5b) corresponding to this state shows the intermittent occurrence of the dominant frequency at $f = 351$ Hz in the signal. In the accompanying power spectrum (Fig. 4.5d), we notice the presence of broadband frequencies having a peak around 351 Hz. Figure 4.5c shows the reconstructed phase portrait during the state of intermittency. We observe a

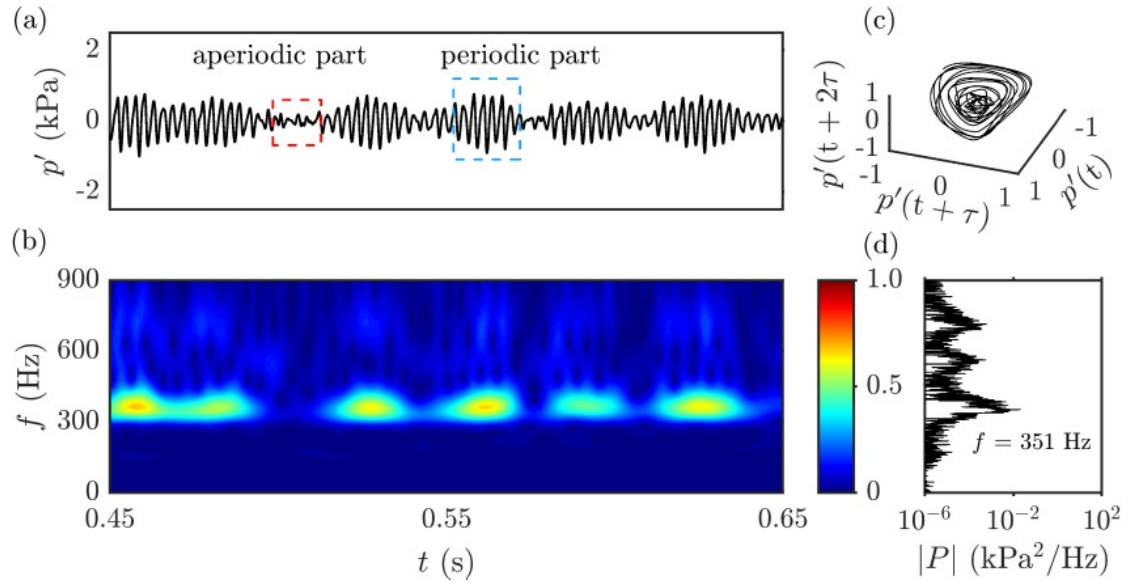


Figure 4.5: (a) The time series, (b) scalogram, (c) three-dimensional phase space, and (d) power spectrum of p' signal during the state of intermittency for $\mathcal{P} = 20.8$ kW, $\phi_g = 0.65$, $HFF = 40\%$, and $Re = 2.68 \times 10^4$.

clutter of trajectories at the centre of the phase portrait due to aperiodic oscillations. These trajectories then spiral towards the distant regular ring-like attractor during the occurrence of bursts of periodicity in the signal, before being re-injected back to the center of the ring at the end of the burst. The flow and flame dynamics corresponding to this state need to be studied separately during aperiodic and periodic epochs.

Figure 4.6 shows the normalized p' and \dot{q}' signals (Fig. 4.6-I) with instantaneous vorticity fields obtained from PIV (Figs. 4.6-II), the heat release rate region of the flame measured over the central plane using from OH-PLIF (Figs. 4.6-III), and the line-of-sight integrated heat release rate measurements obtained from the OH*-chemiluminescence snapshots (Figs. 4.6-IV). These images correspond to five time

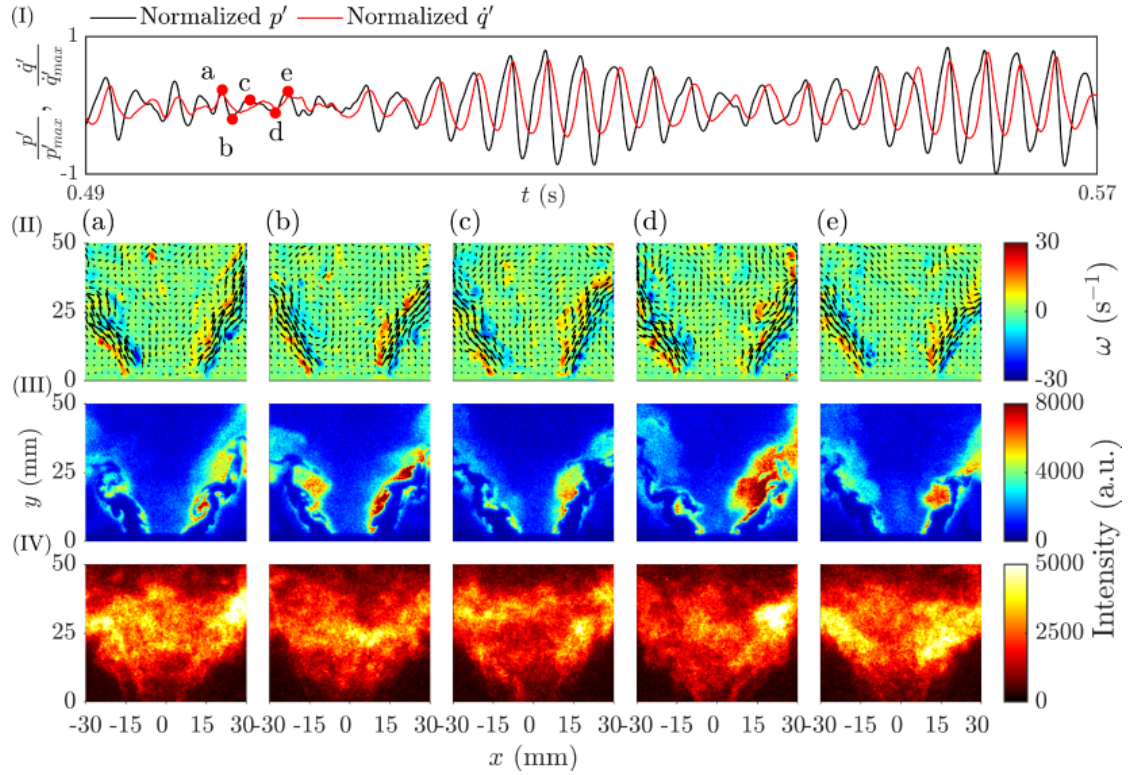


Figure 4.6: (I) The time series of normalized p' and q' fluctuations during the aperiodic epoch in the state of intermittency. The corresponding (II) PIV (III) OH-PLIF, and (IV) OH*-chemiluminescence images are shown.

instants (a - e) marked on the p' signal in Fig. 4.6-I during the epoch of low amplitude aperiodic oscillations of the intermittency state that exhibits a switching between epochs of aperiodic and periodic oscillations. From Fig. 4.6-II, we observe that the asymmetric generation of small-scale vortices continuously along the inner shear layer (ISL) and outer shear layer (OSL) of both the left and right branches of the flame. We also notice that the flame is always stabilized between the inner shear layer and the outer shear layer along the two branches (Figs. 4.6-IIIa-e). We observe a moderate wrinkling on the flame front due to the swirling in the flow. We do not observe significant variations of the flame size and length during the aperiodic epoch of oscillations (Figs. 4.6-III).

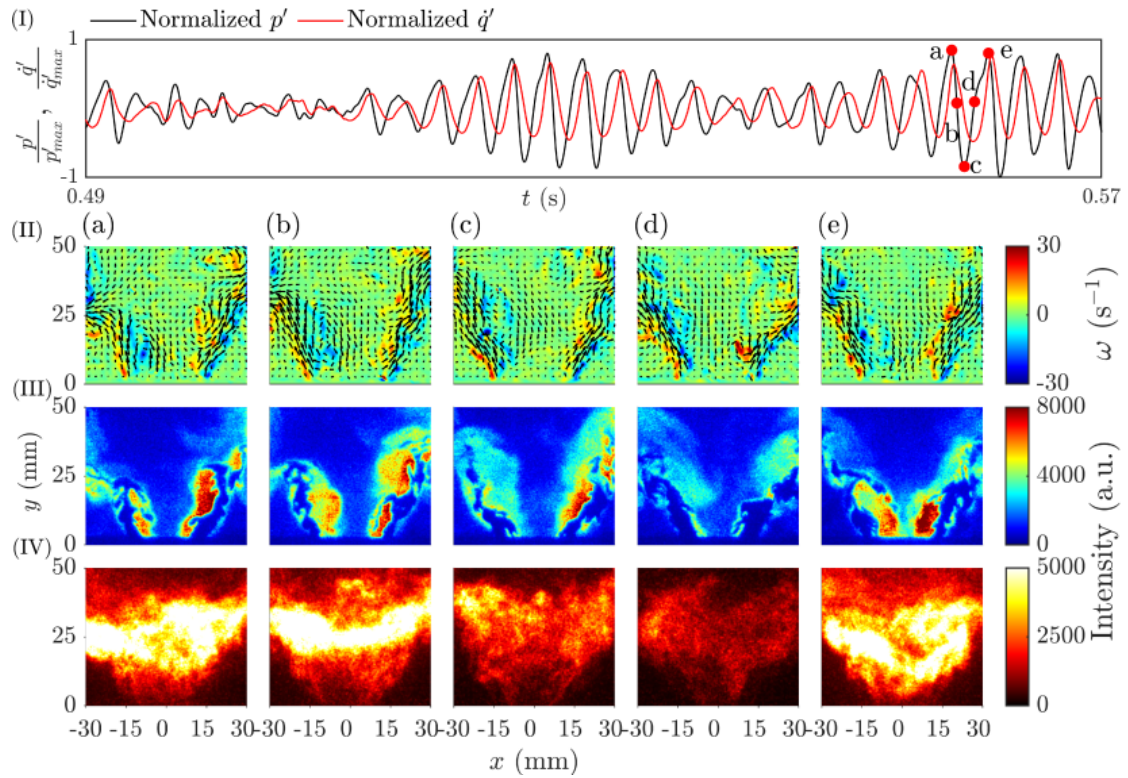


Figure 4.7: (I) The time series of normalized p' and q' fluctuations for five instants (a-e) during one periodic cycle in the state of intermittency. The corresponding (II) PIV, (III) OH-PLIF, and (IV) OH*- chemiluminescence images are shown.

From the corresponding OH*- chemiluminescence images of the flame (Figs. 4.6-IVa-e), we notice that the flame behavior is similar across different time instances as we do not see any significant variations in the shape of the flame. However, at the instances of high positive amplitude oscillations (Figs. 4.6-IVa,e), we observe a small increase in the flame intensity at some spatial locations.

We observe that there is a phase difference between normalized p' and q' during the P1 oscillations (periodic epochs) in intermittent state switching between aperiodic and periodic oscillations (Fig. 4.7-I). Here, we notice larger vorticities compared to the

flow field during the aperiodic region (Figs. 4.7-IIa-e). We observe significant intensity variations in the flame stabilized in the region between the ISL and OSL along both the branches (Figs. 4.7-IIIa-e) with the variation of the pressure from its maxima to minima. When the pressure amplitude is near to its maxima (Fig. 4.7-Ia), we observe the asymmetric emergence of vortices in ISLs (Figs. 4.7-IIa,d and e) and very high flame intensity (Figs. 4.7-IIIa,e). The flame shape widens from maxima to minima of p' . As the pressure reaches its minima (Fig. 4.7-Ic), the thickness of OSL increases while the inner recirculation zone (IRZ) remains unchanged (Fig. 4.7-IIIc). Due to phase shift, we observe the minimum flame intensity (Fig. 4.7-IIId) at instant d, which is very near to the minima of the heat release rate (Fig. 4.7-IVd).

4.4 CHAOTIC OSCILLATIONS

We observe two kinds of chaotic oscillations in the combustor. We refer to these two states as chaotic state-1 (CO1) and chaotic state-2 (CO2) oscillations, respectively. The reasons behind making the distinction between the two chaotic states will become apparent after their descriptions.

In Figs. 4.8a, we show the p' signal and the scalogram corresponding to chaotic state-1 oscillations (CO1). The amplitude of the acoustic pressure does not fluctuate significantly. However, we show that the frequency of these oscillations shows a

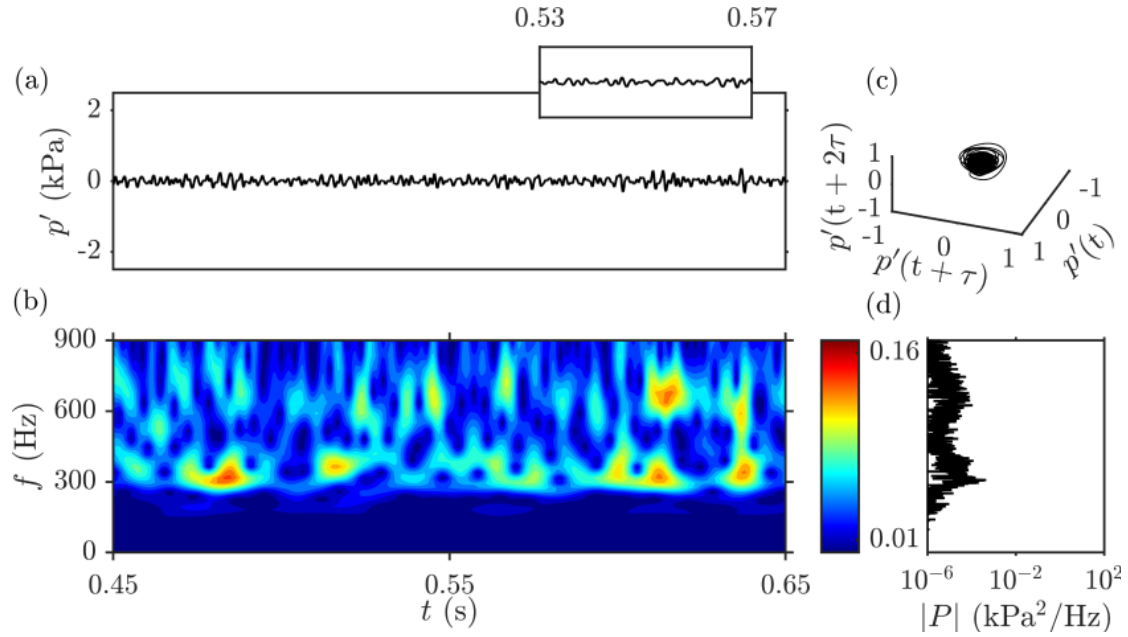


Figure 4.8: (a) The time series, (b) scalogram, (c) three-dimensional phase space, and (d) power spectrum of p' during chaotic state-1 (CO1), observed for $\mathcal{P} = 20.8$ kW, $\phi_g = 0.65$, $HFF = 0\%$, and $Re = 2.41 \times 10^4$.

significant variation in time, shown in Fig. 4.8b. The corresponding power spectrum shows several broadband frequencies without any distinguishable peak (Fig. 4.8d). In the reconstructed phase space (Fig. 4.8c) of this state, we observe the phase space trajectory spiralling inwards and outwards in a haphazard manner.

In Figs. 4.9a,b, we show the p' signal and the scalogram corresponding to chaotic state-2 oscillations (CO2). The amplitude of acoustic pressure during CO2 is appreciably higher than that recorded during CO1. Furthermore, the frequency does not vary considerably in time. As a result, from the corresponding power spectrum (Fig. 4.9d), we see distinct frequency peaks. However, the reconstructed phase space (Fig. 4.9c) of

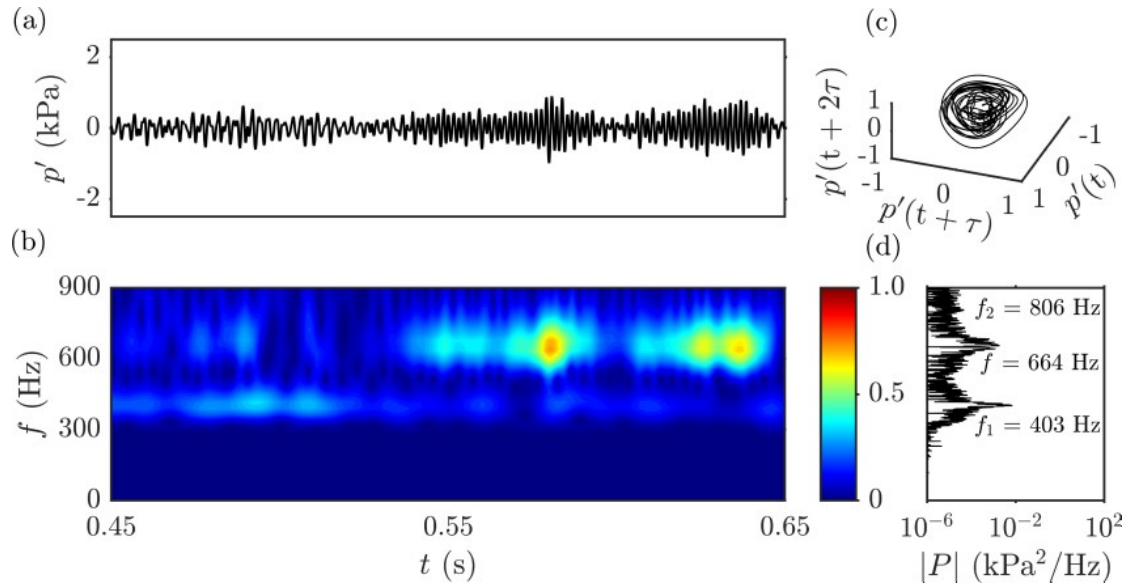


Figure 4.9: (a) The time series, (b) scalogram, (c) three-dimensional phase space, and (d) power spectrum of p' signal during chaotic state-2 (CO₂) for $\mathcal{P} = 15.6$ kW, $\phi_g = 0.8$, $HFF = 70\%$, and $Re = 1.42 \times 10^4$.

this state is similar to that observed in CO1.

In Fig. 4.10, we show the results obtained from the 0-1 test (described Section 3.6)

for the optimally undersampled pressure signal obtained during CO1 and CO2 states.

The trajectories in the $x(n) - y(n)$ plane (Figs. 4.10a(i),b(i)) show a near random

behavior for both states. The variation of $M(n)$ with n exhibits an increasing trend

(Figs. 4.10a(ii),b(ii)). Further, the value of K shows fluctuations near 1 (Figs. 4.10

a(iii), b(iii)). The median value of K is observed to be 0.99 and 0.98 for CO1 and CO2,

respectively.

We also confirmed the existence of chaos with the help of the recently developed *Chaos*

Decision Tree algorithm by [Toker et al. \(2020\)](#). Following this algorithm, we obtained

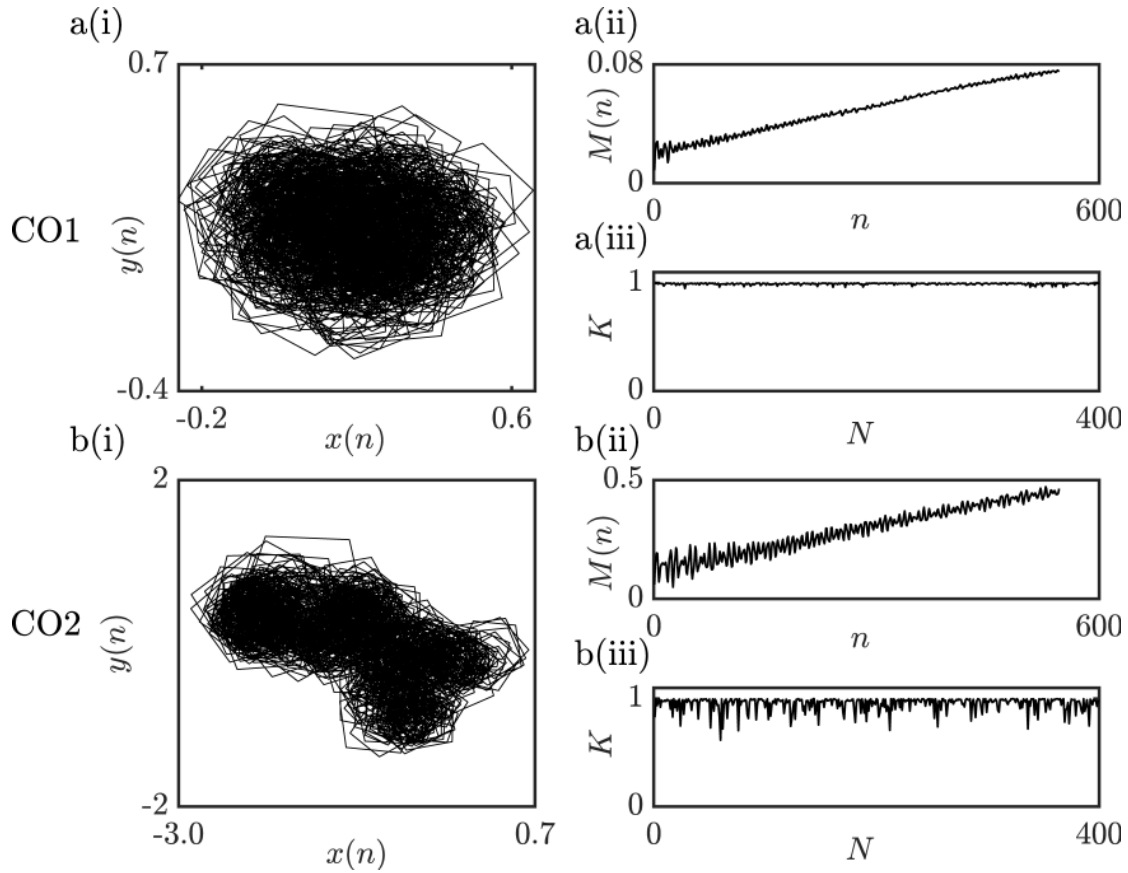


Figure 4.10: 0-1 test performed for chaotic state-1 (Fig. 4.8a) and chaotic state-2 (Fig. 4.9a). (i) The plot between the translation variables $x(n)$ and $y(n)$, (ii) the behaviour of mean square displacement $M(n)$ with n , and (iii) the variation of the growth rate K with N .

$K = 0.99$ and 0.93 for CO1 and CO2 states, respectively. Therefore, the results from the 0-1 test as well as the *Chaos Decision Tree algorithm* substantiate the presence of chaos in the acoustic pressure time series exhibited by the combustor during the CO1 and CO2 states.

In order to understand the chaotic oscillations spatiotemporally, we plot the instantaneous images of the velocity, flame and heat release rate distribution fields for 5 different instants. Figure 4.11 shows the normalized p' and q' signals (Fig. 4.11-I),

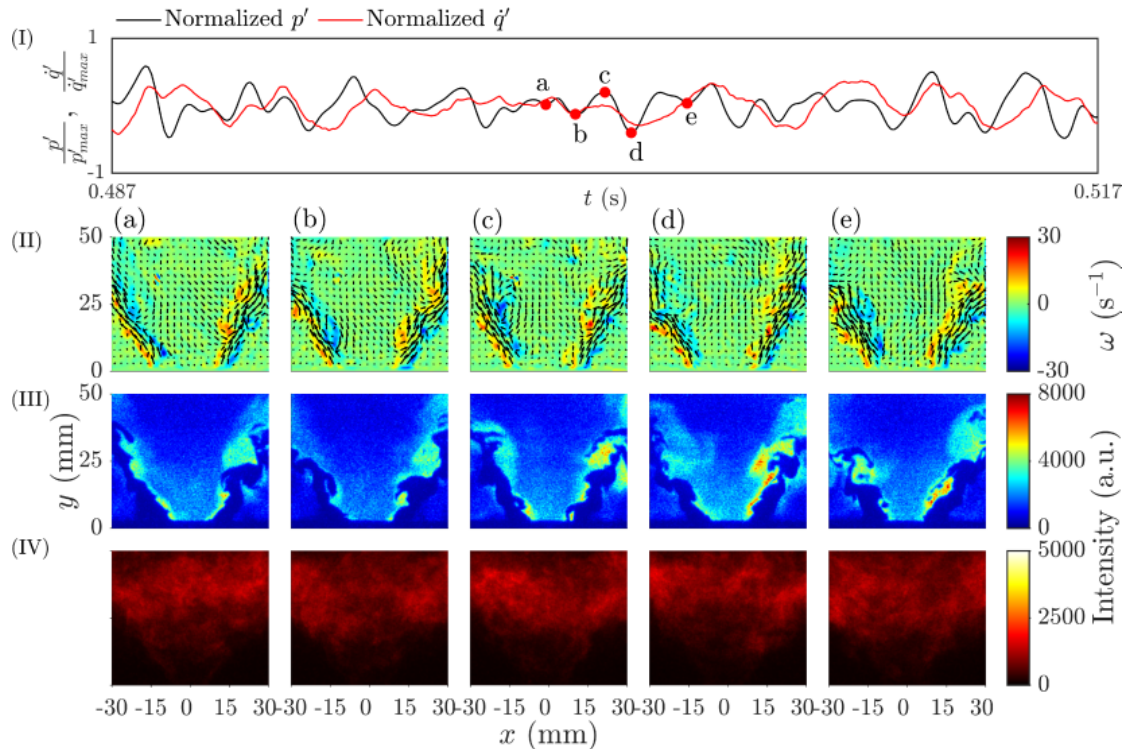


Figure 4.11: (I) The time series of normalized p' and q' fluctuations for five time instants (a-h) during different instants indicating the local maxima and minima in chaotic state-1. The corresponding (II) PIV (III) OH-PLIF, and (IV) OH*-chemiluminescence images are shown.

instantaneous images of the flow and vorticity fields obtained from PIV (Fig. 4.11-II), the distribution of OH radicals over the central plane using OH-PLIF (Fig. 4.11-III), and the line of sight integrated OH*-chemiluminescence field (a measure of heat release rate distribution) during chaotic state-1 (CO1) in the system (Fig. 4.11-IV). These images correspond to five time instants (a)-(e) marked on the p' signal (Fig. 4.11-I). Only the common regions covered by all the three imaging techniques (section 2.3) are shown. From Fig. 4.11-II, we observe that several small-scale vortices are generated irregularly along the inner and outer shear layers in both the left and right flame branches. We also notice that the V-shaped flame is always stabilized in the region between the inner shear

layer (ISL) and outer shear layer (OSL) along the two branches (Fig. 4.11-III). We observe moderate wrinkling of the flame front due to the swirling action in the flow. We do not observe significant changes in the flame size and length over time (Fig. 4.11-III). From the corresponding OH*-chemiluminescence images of the flame (Fig. 4.11-IV), we observe that the flame behavior is similar across different time instants as we do not see any significant change in the flame intensity.

The flame stabilizes in both IRZ and ORZ along two separate branches of the flame front (Figs. 4.12-IIIa-h) for all time instants during the state of chaotic state-2 (CO₂).

When the pressure is at its first maxima (Fig. 4.12-Ia), we do not observe any vortex with a significant magnitude of vorticity (Fig. 4.12-IIa). The corresponding flame image (Fig. 4.12-IIIa) shows a moderate intensity. The chemiluminescence image at this instant (Fig. 4.12-IVa) shows that the flame is compact and the heat release rate distribution is concentrated at a small distance from the inlet of the combustion chamber. As the pressure reaches its first minima (Fig. 4.12-Ib), the vorticity (Fig. 4.12-IIb) and the flame intensity in the IRZ do not change significantly (Fig. 4.12-IIIc).

The corresponding chemiluminescence image (Fig. 4.12-IVb) indicates a reduction in the heat release rate distribution. On proceeding to the second maxima (Fig. 4.12-Ic) and second minima (Fig. 4.12-Id) on the p' signal, the vortices with symmetric behavior

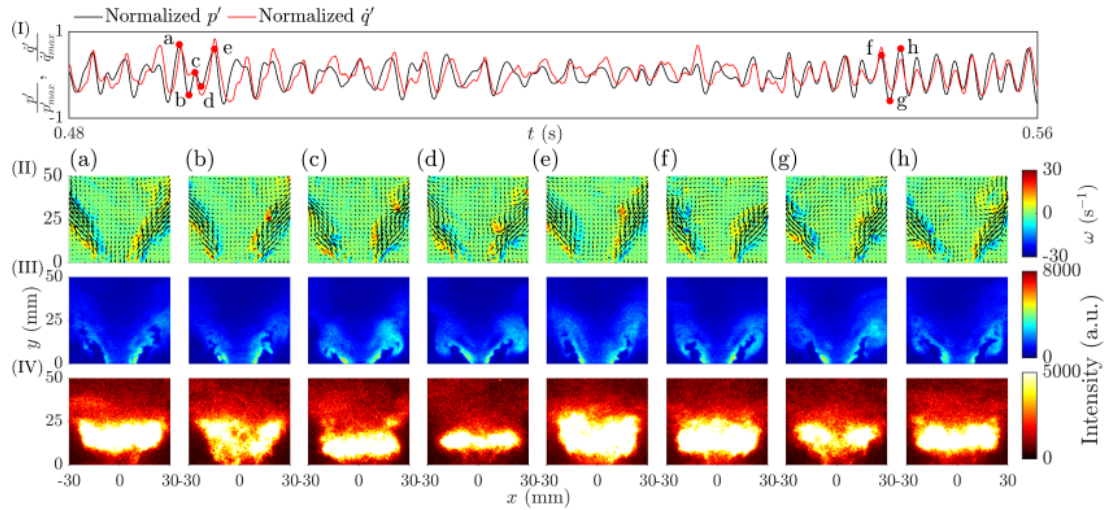


Figure 4.12: (I) The time series of normalized p' and q' fluctuations for eight time instants (a-h) during different instants indicating the local maxima and minima in chaotic state-2 (CO₂). The corresponding (II) PIV, (III) OH-PLIF, and (IV) OH*-chemiluminescence images are shown.

are observed in the spatial field (Figs. 4.12-IIIc,d) and the flame gradually widens (Figs. 4.12-IVc,d). The heat release rate distribution becomes compact and is shifted to near the inlet of the combustion chamber (Fig. 4.12-IVc) and again shifted to slight away from the dump plane (Fig. 4.12-IVd). After the pressure crosses its second minima, we observe that the vortices that were initially shed at the second maxima, convect outside the window.

During another instants (f-h) in chaotic state-2, we observe that p' and q' are almost phase-locked (Fig. 4.12-I). Here, we see vortices with low vorticity in the flow field (Figs. 4.12-IIa-e). we observe moderate intensity in the flame stabilized in the region between the ISL and OSL along both the branches (Figs. 4.12-III f-h) with pressure

variation. The corresponding chemiluminescence images show compact behavior of the heat release rate distribution near the dump plane (Figs. 4.12-IVf,h). When the pressure amplitude is at its maxima (Fig. 4.12-If), we notice the asymmetric emergence of vortices in ISLs and moderate flame intensity in the flow field (Figs. 4.12-III f,h). The flame shape is not changing significantly with change in pressure. As the acoustic pressure fluctuations nears its minima (Fig. 4.12-Ig), again a pair of vortices is observed to be shed. The heat distribution appears to be divided into two regions (Fig. 4.12-IVg). As the acoustic pressure fluctuations again increases, we see the regions of the heat release rate distribution unite (Fig. 4.12-IVh).

Overall, we observe dramatic changes in the flame and flow dynamics during chaotic state-2, which is completely different from the state of TAI with period-1 and period-2 oscillations.

4.5 TRANSITION FROM P2 LCO TO P1 LCO

In this section, we discuss the transition of dynamics in the combustion chamber as HFF is increased from 0% to 60% while maintaining the same equivalence ratio and thermal power. Figure 4.13 represents the effect of increase in HFF for the operating conditions of $\mathcal{P} = 15.6$ kW and $\phi_g = 0.8$ mentioned in Table 2.1. For $HFF = 0\%$,

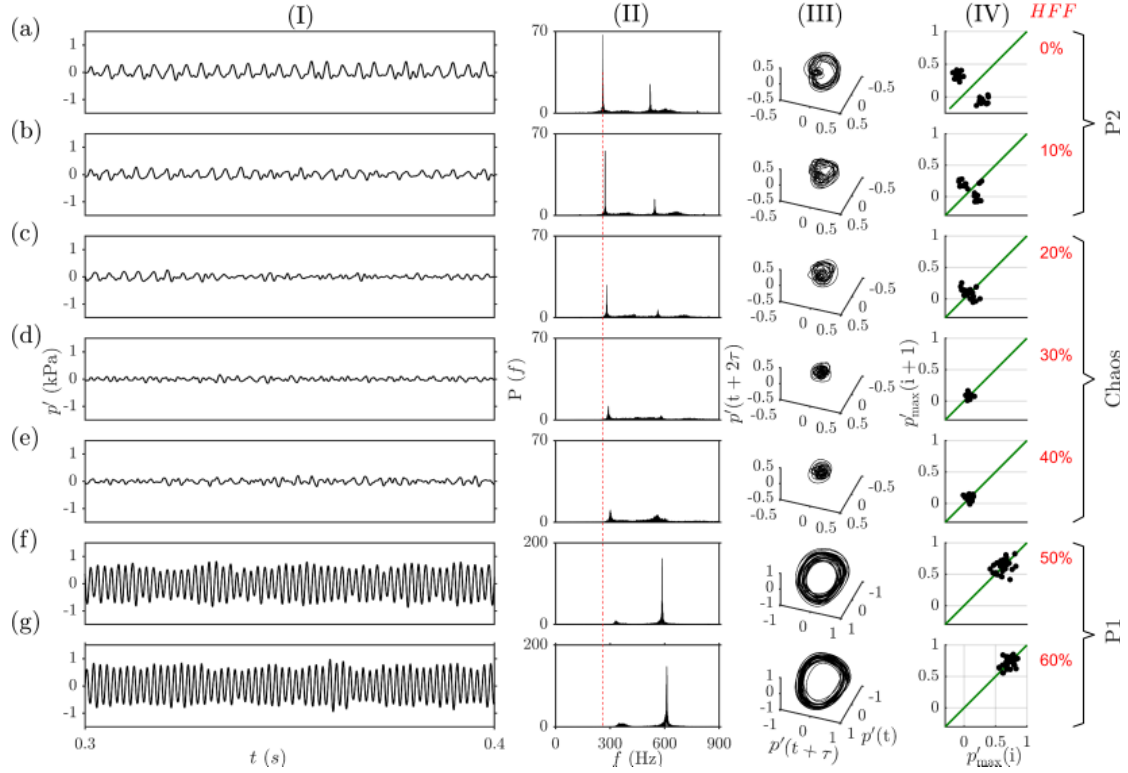


Figure 4.13: The effect of increasing HFF in the fuel on the acoustic pressure oscillations is presented using (I) time series, (II) amplitude spectrum, and (III) three-dimensional phase space, and (IV) first return map of p' oscillations. HFF is varied from 0% to 60% in steps of 10% while maintaining $\mathcal{P} = 15.6$ kW and $\phi_g = 0.8$. The red colored dotted line in (II) represents the frequency of the fundamental mode in the combustor for 0% HFF .

p' show the characteristics of P2 oscillations (Fig. 4.13Ia). We also plot the amplitude spectrum (Fig. 4.13IIb) which exhibits the presence of two peaks ($f_1 = 260$ Hz and $f_2 = 520$ Hz) with comparable amplitude ($P(f_1)/P(f_2) < 5$). Accordingly, the phase space trajectory is bounded by a double-looped attractor (Fig. 4.13IIIa) and the first return map contains two clusters (Fig. 4.13IVa). Here, the return map (Nayfeh and Balachandran, 2008) is obtained by plotting the successive local maximas of the p' signal in time. A small addition of HFF leads to a reduction in the amplitude of

P2 oscillations (Fig. 4.13Ib). On further increase in HFF beyond 10%, we observe a significant decrease in the amplitude of frequencies at both modes of the p' signal (Figs. 4.13IIc to 4.13IIe). As a consequence, we notice a change in the system dynamics from P2 LCO to chaotic state-2. The amplitude spectrum (Figs. 4.13IIc to 4.13IIe) shows the shift in both peaks to a higher value. The phase space trajectories of this state show a cluttered behavior due to the interaction of multiple broadband frequencies (Figs. 4.13IIIc to 4.13IIIe). The first return map exhibits a cluster of points that align along the diagonal line (Figs. 4.13IVc to 4.13IVe).

For $HFF = 50\%$, we notice the occurrence of a considerably high amplitude P1 LCO in the system (Fig. 4.13If). The corresponding amplitude spectrum (Fig. 4.13IIIf) displays a dominant frequency at ($f = 586$ Hz) with very high amplitude. The phase space (Fig. 4.13IIIIf) of this state exhibits a ring-like attractor. The first return map for this case shows a cluster of points on the diagonal for larger amplitudes (Fig. 4.13IVf). Similar behavior is also observed for $HFF = 60\%$ (Fig. 4.13Ig). Therefore, we observe the change of the system behavior from P2 to P1 oscillations via chaotic oscillations as HFF is increased.

We also notice a gradual increase in the frequencies of the fundamental and harmonic modes due to the increasing content of H_2 in the fuel (see Fig. 4.13III). The rise in the

unstable frequencies of the system occurs as a result of the escalation in the adiabatic temperature of the flame (refer to Appendix B). The adiabatic flame temperature increases by about 100 K as HFF is increased from 0% to 80%. Thus, hydrogen enrichment of methane results in the occurrence of different dynamical states in the system, which leads to the progressive shifting of the frequency and the interaction of unstable acoustic modes of the combustor.

4.6 INTERIM SUMMARY

In this chapter, we have characterized different dynamical states exhibited by the combustor as a result of hydrogen enrichment at constant global equivalence ratio and thermal power. Based on different methods including time series analysis, phase space reconstruction, power spectrum and continuous wavelet transformation, we have categorized the experimental data into mainly four dynamical states: chaotic oscillations (CO1 and CO2), intermittency, period-1 limit cycle oscillations and period-2 limit cycle oscillations.

In order to understand different dynamical states thoroughly, we also studied the spatiotemporal behaviour of the combustor during different dynamical states using the instantaneous images acquired simultaneously through various high-speed imaging techniques. Using PIV images, we discussed the emergence of vortices and their growth

at various regions such as the inner recirculation region and the outer recirculation region. Using the PLIF images, we showed the stabilization and shape of the flame at the center plane of the combustion chamber for each dynamical state. Generally, the flame stabilizes along the shear layers visualizing either M or V shape. However, during the states of P2-LCO, the flame exhibits columnar shape (a thin jet-like structure) and stabilizes in the inner recirculation region. With the help of OH*-chemiluminescence images, we discussed the heat release rate distribution and flame intensity using OH* radicals. During the periodic signals (P1-LCO, P2-LCO and periodic burst of intermittency), we see the periodic increase and decrease in the flame intensity. However, the flame intensity does not exhibit any variation during the chaotic state-1 oscillations and aperiodic signal of intermittency. For the state of CO₂, area of high flame intensity varies over time with low variation in flame intensity.

Finally, we analyzed the transition of dynamical states from P2-LCO to P1-LCO through chaos (chaotic state-2 oscillations) due to addition of hydrogen while maintaining a constant global equivalence ratio and thermal power. We used time series analysis along with the corresponding power spectra, phase-space reconstructions and first return map. In the absence of hydrogen in the fuel, the combustor exhibits period-2 limit cycle oscillations, represented by a double loop attractor having two

frequencies with the same order of spectral amplitude and two clusters of points in the first return map. With the addition of 20% to 40% hydrogen by volume in the fuel, chaotic dynamics is seen in the acoustic pressure signals exhibited by the combustor. We observed suppression of spectral power at dominating frequency in power spectra, clutters of trajectories in phase space with clusters of points having low values in first return maps. The combustor exhibits period-1 limit cycle oscillations with 50% and 60% hydrogen in the fuel. These signals show single loop attractors in phase space, single frequency with spectral amplitude in power spectra and cluster with high values in first return maps. With the addition of hydrogen, the flame temperature increases (shown in Fig. B.1) which leads to increase in the speed of sound and results in the shifting of the dominating frequencies of the dynamical states in the combustor.

In the next chapter, we introduce the Lissajous patterns and study the frequency locking behaviour between acoustic pressure, heat release rate and flow velocity fluctuations for the states of chaotic oscillations (CO1) and thermoacoustic instabilities with period-1 and period-2 limit cycle oscillations.

CHAPTER 5

FREQUENCY LOCKING AMONG ACOUSTIC PRESSURE, HEAT RELEASE RATE AND FLOW VELOCITY

As we know, a positive feedback (or mutual synchronization) between p' and \dot{q}' fluctuations is mostly responsible for the occurrence of TAI (Pawar *et al.*, 2017, 2019). In this chapter, we discuss the temporal signals and analyze the coupled interactions of flow velocity fluctuations with acoustic pressure and heat release rate fluctuations during distinct dynamical states, i.e., CO1, P1 and P2 LCOs, present in the PRECCINSTA burner. In order to define the flow velocity fluctuations, we use a data-driven method known as proper orthogonal decomposition (POD) (see Section 3.3). Using POD, we calculate the temporal coefficients of each dominating modes for different dynamical states such as CO1, P1 and P2 LCOs.

5.1 CHAOTIC STATE-1 OSCILLATIONS

First, to understand the temporal dynamics of chaotic behaviour in the combustion chamber, we discuss the characteristics of the temporal signals for the state of chaotic state-1 (CO1) oscillations. Figure 5.1 displays the normalized time series of the

Some sections of this chapter are published in A. Kushwaha, K. Praveen, Samadhan A. Pawar, R. I. Sujith, I. Chterevev, and I. Boxx (2021). Dynamical characterization of thermoacoustic oscillations in a hydrogen-enriched partially premixed swirl-stabilized methane/air combustor. *Journal of Engineering for Gas Turbines and Power*, **143(12)**: , 121022 (11 pages)

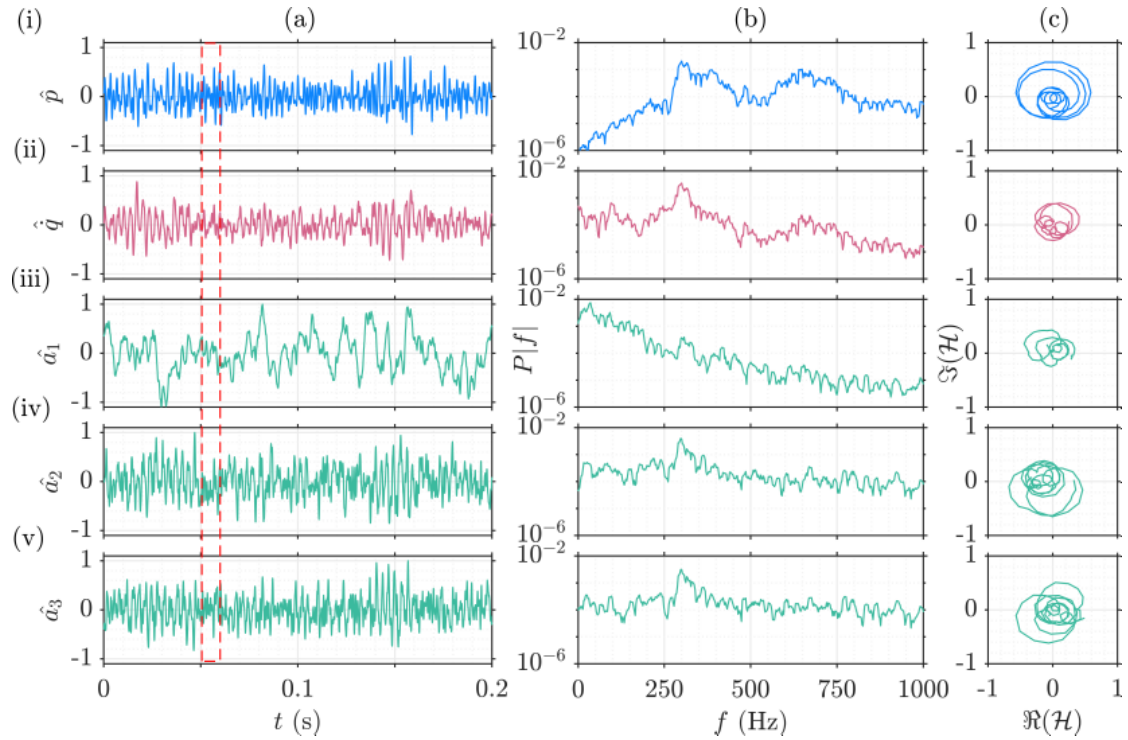


Figure 5.1: Characterization of the thermoacoustic response during the state of chaotic oscillations. (a) Time series and (b) power spectra of fluctuations in acoustic pressure, heat release rate and the temporal coefficients of the first three POD modes. (c) Phase space trajectory in the complex analytical plane for the part of the signals indicated in panel (a).

acoustic pressure (p') and the heat release rate fluctuations (q'), along with the temporal coefficients corresponding to the first three POD modes. Here, $q'(t)$ is obtained by a global summation from individual chemiluminescence images. Each of the time series are normalized by their respective maxima to aid comparison. The aim is to relate the manner in which the spatial modes of velocity fields evolve in time and relate to fluctuations in p' and q' . In each case, the temporal signals are characterized by the power spectral density in the frequency domain and the phase portrait of the analytic signal defined according to Eqn. (3.22).

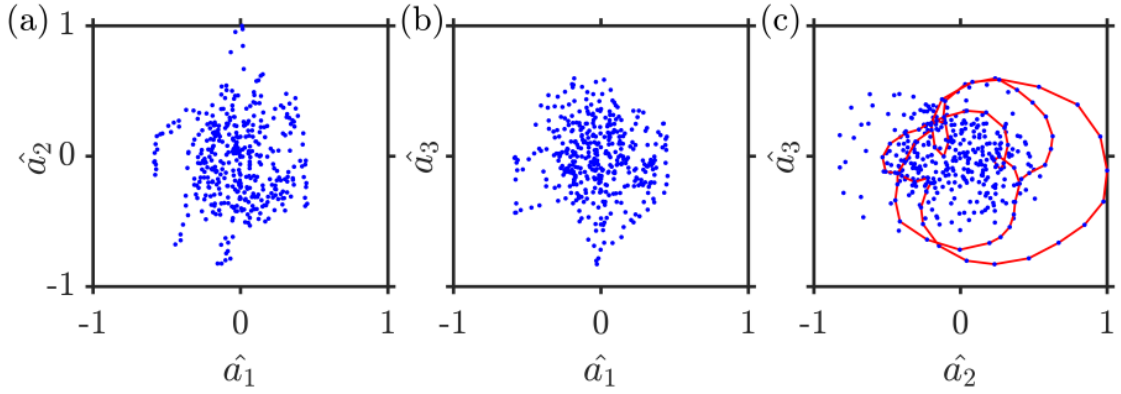


Figure 5.2: (a-c) Phase portrait of the pairs of temporal coefficients ($a_1 - a_3$) of the first three POD modes of the velocity field for the state of chaotic oscillations. The red lines indicate a few periodic orbits.

The state of chaotic state-1 oscillations corresponds to the low-amplitude stable operation of the combustor. The acoustic pressure and the heat release rate oscillations during this baseline case remain chaotic. This can be observed in Fig. 5.1b where the power spectral density for p' , q' and the temporal coefficients (a_1, a_2, a_3) depict a broadband behavior. In addition, the phase portrait featuring the analytic representation of these signals depict the absence of a unique center of rotation. Hence, the signals are non-analytic, and a phase cannot be ascribed to these signals using the Hilbert transform.

We perform the 0-1 test (described in §3.6) for these signals to ascertain whether their dynamics is chaotic or not. The value of the asymptotic growth rate K of the displacement M between translational variables is tabulated in Table 5.1. We note here that all the signals display values which are close to unity, implying chaotic evolution of each of these quantities. Thus, the heat release rate and acoustic pressure oscillations

Signals ↓ \ Dynamical states →	Chaotic oscillations	P1-LCO	P2-LCO
p'	0.99	0.08	0.01
q'	0.98	0.11	0.05
a_1	0.62	0.15	0.27
a_2	0.99	0.12	0.32
a_3	0.99	0.61	0.79

Table 5.1: Results of the 0-1 test for different signal during all the dynamical states discussed in this paper. The values close to 1 indicate the existence of chaos in the signal. The signal with regular dynamics show the values close to 0.

display chaos during stable combustor operation, thus corroborating past results (Nair and Sujith, 2014).

In Fig. 5.2, we show the phase portraits generated with the pairs of first three temporal coefficients of dominating POD modes. The pairs of signal a_1 with a_2 and a_3 do not show any pattern indicating that there is no coupled interaction between these signal (Figs. 5.2a,b). However, the pair of signals a_2 and a_3 shows a pattern having a few periodic orbits indicating that these chaotic signals exhibit the same frequency for a small interval of time period.

5.2 1:1 FREQUENCY LOCKING

We first understand the coupled interaction between the fluctuations in acoustic pressure and heat release rate during the state of period-1 LCO. We generate overlapped time series plots of the normalized p' and q' signals during the P1 LCO state (Fig. 5.3a). The

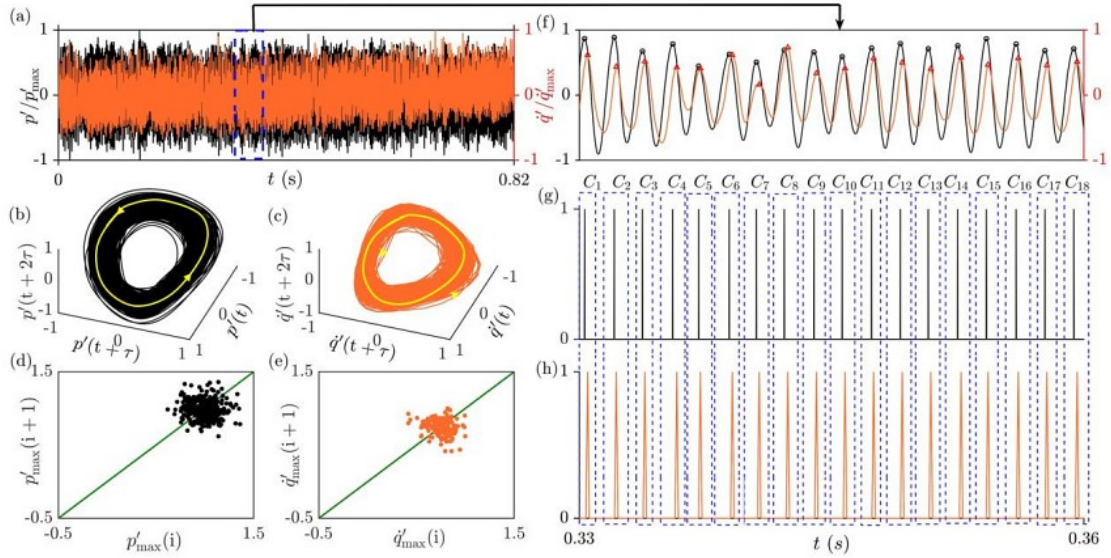


Figure 5.3: Illustration of 1:1 frequency locking between p' and q' signals during the state of period-1 LCO. (a) Time series of the normalized p' (black line) and q' (orange line) signals, (b, c) the corresponding phase spaces, and (d, e) first return maps for $\mathcal{P} = 15.6$ kW, $\phi_g = 0.8$ and $HFF = 50\%$. (f) The zoomed view of the signals with markers corresponding to the local maximas. (g, h) The spiking signals indicating the locations of local maximas in p' and q' oscillations, respectively. C_1, C_2, \dots in (g) represent the number of cycles, and blue dotted boxes contain the number of peaks in one oscillation cycle of p' and q' signals.

normalization is performed with respect to their respective maximum values. During this state, we observe that both p' and q' signals are in-phase synchronized, where every oscillation cycle of p' appears to be locked with that of q' , thus, satisfying the Rayleigh's criterion (Rayleigh, 1878). In Figs. 5.3g,h, we represent spikes of unit magnitude corresponding to the time instants at which the corresponding p' and q' signals (Fig. 5.3f) attain the local maximas, respectively. We observe single local peak from both the signals in each cycle (indicated by dashed boxes C_1, C_2, \dots, C_{18} in Figs. 5.3g,h). This is further confirmation of the fact that the p' and q' signals have

the same frequency (Figs. 5.3g,h). Thus, during the state of P1 LCO, both p' and q' signals exhibit 1:1 frequency locking (mutual synchronization). The corresponding phase spaces for p' and q' (Figs. 5.3b,c) contain a single ring-like attractor, indicative of LCO. The first return maps for p' and q' (Figs. 5.3d,e) exhibit a single cluster of points at the diagonal line with high amplitudes.

To study the temporal behaviour along with the flow velocity fluctuations during the state of TAI with P1-LCO, we plot the time series, power spectra and analytical signal of acoustic pressure, heat release rate and temporal coefficients of three dominating POD modes, shown in Fig. 5.4. The normalized time series of p' and q' show high amplitude fluctuations compared to that during the chaotic oscillations (Figs. 5.4ai to 5.4aaii). We also observe a distinct peak at 415 Hz and its higher harmonic at 827 Hz for the acoustic pressure and heat release rate signals (Figs. 5.4bi to 5.4bii). Moreover, the trajectories in the analytical plane show a unique center of rotation (Figs. 5.4ci to 5.4cii). The temporal coefficients of the first and second modes are periodic in nature (Figs. 5.4aiii to 5.4aiv) and exhibit distinct peak at 415 Hz (Figs. 5.4biii to 5.4biv). However, the third mode does not show periodic behaviour (Fig. 5.4av) and we observe a broadband power spectrum without any distinct peak (Fig. 5.4av). The analytical signal for the first and second mode signal have a particular origin of rotation which confirms that

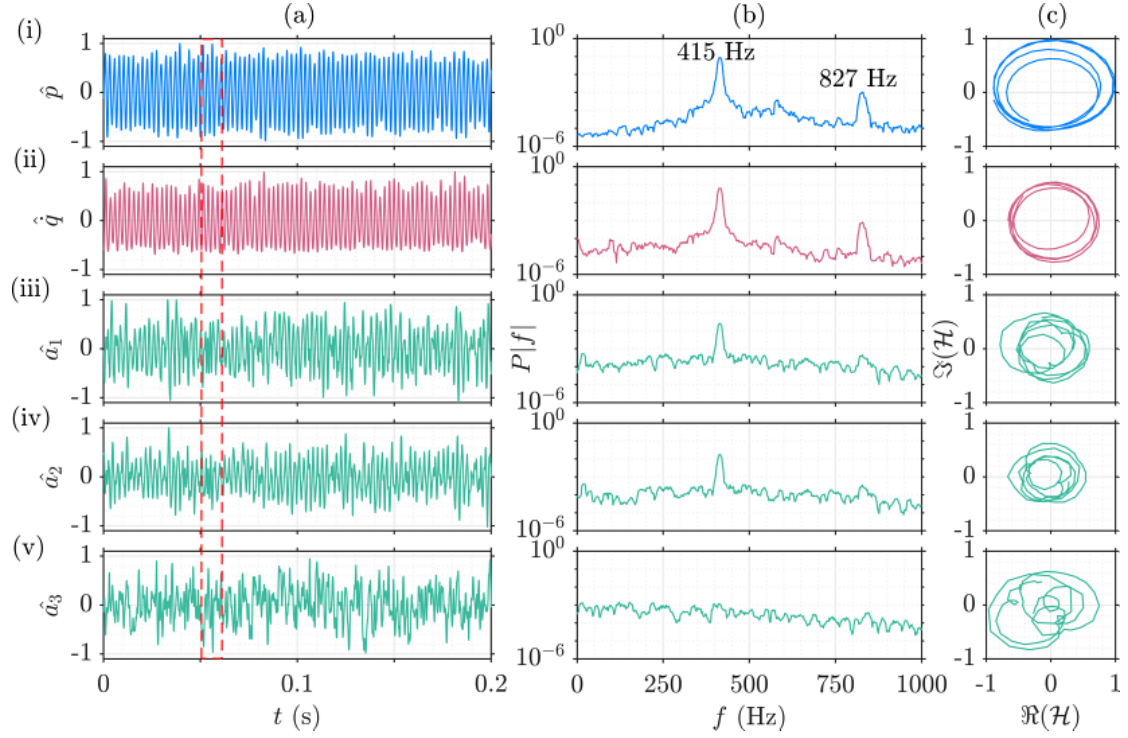


Figure 5.4: (a) time series of (i) acoustic pressure, (ii) heat release rate, (iii - v) temporal coefficients of first three POD modes normalised by their respective maxima values; (b) the corresponding power spectra and (c) the analytical signals in the complex plane, corresponding to the time series enclosed in the red dashed box during the state of period-1 limit cycle oscillations for $\mathcal{P} = 20.8$ kW, $\phi_g = 0.8$, $HFF = 50\%$, and $Re = 2.64 \times 10^4$.

we can calculate instantaneous phases of a_1 and a_2 using the Hilbert Transformation (see section 3.5) to understand the frequency locking behaviour with the help of the Lissajous patterns. The analytical signal of the third mode do not show a unique center of rotation for the trajectories which suggest that we cannot calculate the instantaneous phase using the Hilbert transform for the a_3 signal.

In order to understand the coupling behaviour among the time signals shown in Figs. 5.4ai to 5.4iv, we, firstly, normalize the signals with their respective maxima. Then, we

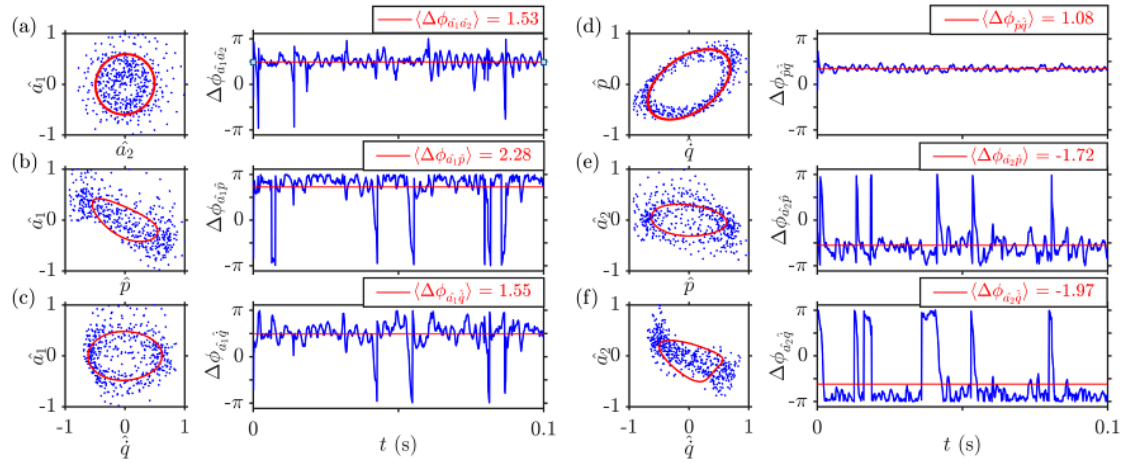


Figure 5.5: (a-f) Phase portrait of the temporal coefficients of the POD modes of the flow velocity field with respect to acoustic pressure and heat release rate along with analytical curves having the same dominating frequencies and phase differences as the original data and the corresponding phase difference with the red line indicating the mean value of phase difference, for the state of TAI with period-1 LCO.

choose a pair of signals and plot phase portrait (Figs. 5.5a to 5.5f). We also calculate and show the instantaneous phase difference between the signals for each pair (Figs. 5.5i to 5.5vi). We compute a mean of the instantaneous phase difference and show it with a red line. With the help of dominant frequencies and mean phase difference for each pair of signal, we generate the analytical curve (see section 3.5) and show it for each pair with red color. These analytical curves identify the pattern of each pair of the signals. We notice circular patterns in Figs. 5.5a,c as the mean phase difference value for these pairs is close to $\pi/2$ (Figs. 5.5i,iii). Apart from the circles, we also see the elliptical curves due to the mean phase difference values other than 0 and $\pi/2$. These patterns (circles and ellipses) are similar to the Lissajous patterns which indicate frequency locking in terms of ratio between the dominating frequencies of the pair of

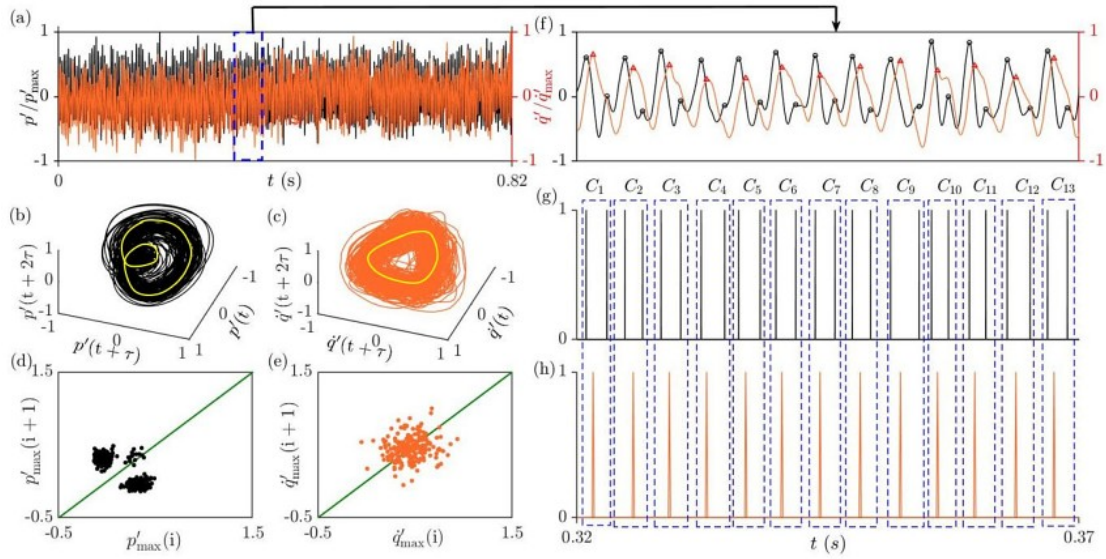


Figure 5.6: Depiction of 2:1 frequency locking between p' and q' signals during the state of P2 LCO. (a) Time series of normalized p' (black line) and q' (orange line) signals, (b, c) the corresponding phase spaces, and (d, e) first return maps for the conditions of $\mathcal{P} = 15.6$ kW, $\phi_g = 0.8$ and $HF\mathcal{F} = 0\%$. The description of (f, g, h) is the same as that in Fig. 5.3.

the signals. We see differences between the patterns from our experimental data and the traditional Lissajous patterns due to the existence of higher harmonics that affects the shape as well as the size of the patterns. These results identify 1:1 frequency locking behaviour among the acoustic pressure, the heat release rate and the flow field dynamics during the state of TAI with period-1 limit cycle oscillations.

5.3 2:1 FREQUENCY LOCKING

Next, we show the coupled dynamics of p' and q' signals observed during the state of TAI with period-2 LCO in Fig. 5.6. The magnified views (Fig. 5.6f) of these signals show markers corresponding to their local maxima, which are captured by the spiking

signals in Figs. 5.6g,h. From Figs. 5.6g,h, we observe that in one cycle (denoted by C_1, C_2, \dots, C_{13} in Figs. 5.6g,h), there are two peaks in the p' signal and one peak in the q' signal (see blue dashed rectangle in Figs. 5.6g,h). This means that the p' signal exhibits two oscillations in a single period, while q' signal exhibits a single oscillation in the same time period. This further indicates the presence of 2:1 frequency locking between p' and q' during the state of P2 LCO in the system. Note that both p' and q' signals have the same dominant frequency. The reconstructed phase spaces (Figs. 5.6b,c) and the first return maps (Figs. 5.6d,e) for p' and q' , also confirms this locking behavior of the signals. For p' signal, the phase space has a two looped structure (Fig. 5.6b); in contrast, for the q' signal, the phase space contains a single ring-like structure (Fig. 5.6c). For p' signal, the first return map exhibits two prominent clusters at off-diagonal locations, representing two loops in the phase space trajectories. Additionally, a minor scatter of points is observed along the diagonal line, attributed to the turbulent fluctuations underlying the system. In contrast, we notice a single cluster of points in the return map of q' signal.

The time series, the power spectra and the analytical signal are shown for the state of period-2 limit cycle oscillations in Fig. 5.7. The time series of p' has period-2 oscillations (Fig. 5.7ai). However, the signal of q' exhibits period-1 limit cycle

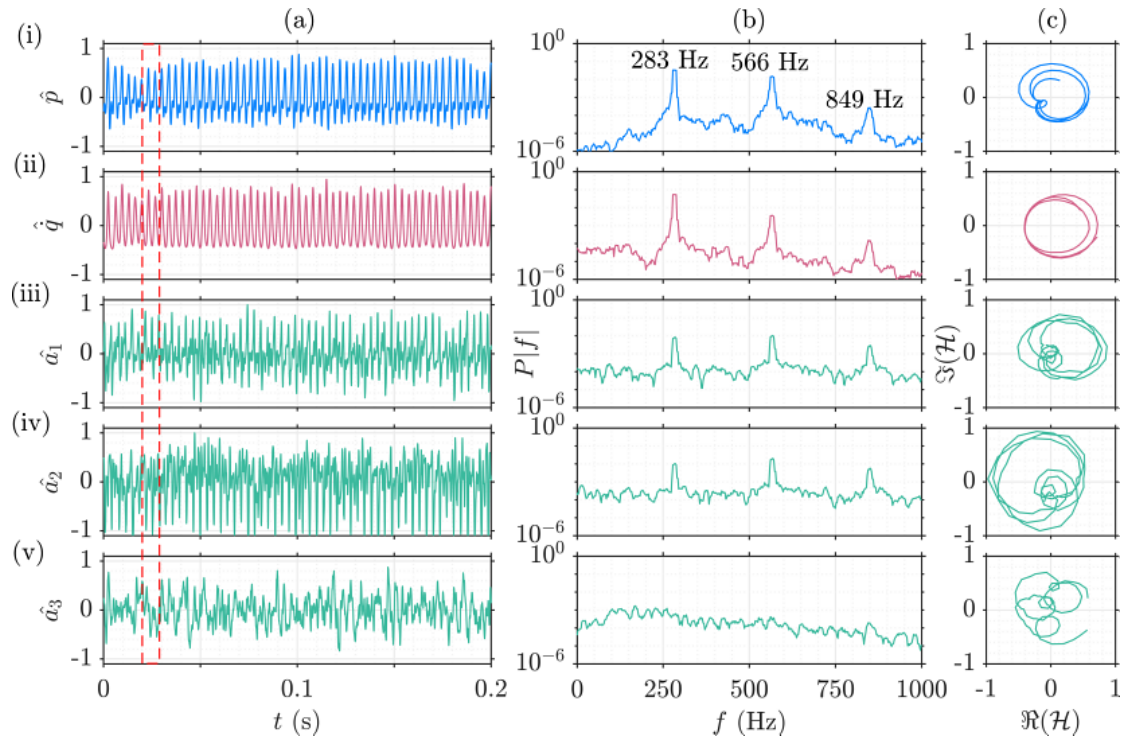


Figure 5.7: (a) time series of (i) acoustic pressure (ii) heat release rate (iii - v) temporal coefficients of first three POD modes normalised by their respective maxima values; (b) the corresponding power spectra and (c) the analytical signals in the complex plane, corresponding to the time series enclosed in the red dashed box during the state of period-2 limit cycle oscillations for $\mathcal{P} = 20.8$ kW, $\phi_g = 0.8$, $HFF = 20\%$, and $Re = 2.74 \times 10^4$.

oscillations (Fig. 5.7aii). The power spectra of both the signals show a distinct peak at 283 Hz with higher harmonics at 566 Hz and 849 Hz (Figs. 5.7bi,ii). In Fig. 5.7ci, the trajectory of the analytical signal forms a double-looped pattern on the complex plane. However, we observe a unique center of rotation for the trajectory for the analytical signal of q' (Fig. 5.7cii). Similar to the p' signal, we notice the period-2 nature in the time series of a_1 and a_2 (Figs. 5.7aiii,iv) with the distinguished peaks at 283 Hz, 566 Hz and 849 Hz in the power spectra, shown in Figs. 5.7biii,iv. We also observe the patterns with double loops formed by the trajectories of the analytical signals of time series of a_1

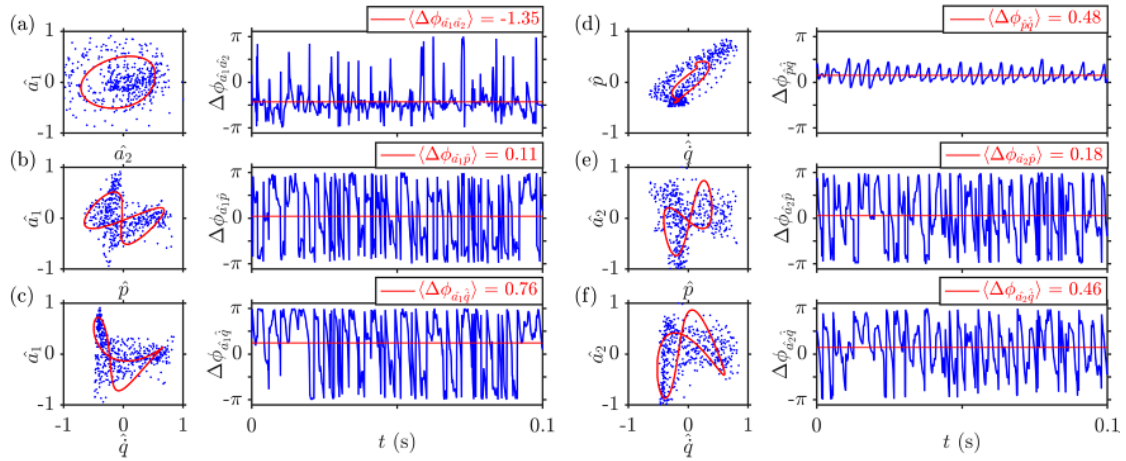


Figure 5.8: (a-f) Phase portrait of the temporal coefficients of the POD modes of the flow velocity field with respect to acoustic pressure and heat release rate along with analytical curves having the same dominating frequencies and phase differences as the original data and the corresponding phase difference with the red line indicating the mean value of phase difference, for the state of TAI with period-2 LCO.

and a_2 (Figs. 5.7ciii,iv). In case of the third mode, we do not see a periodic behaviour in the time series, shown in Fig. 5.7av. Further, we notice a broadband spectrum without any distinct peak in the power spectrum (Fig. 5.7bv) and also found that the trajectory of the analytical signal does not have a unique center of rotation (Fig. 5.7cv).

Unlike period-1 limit cycle oscillations, we observe different patterns similar to the Lissajous figures during period-2 limit cycle oscillations. For the pair of a_1 and a_2 , we see a circular pattern (Fig. 5.8a) as the mean phase difference is close to $\pi/2$ (Fig. 5.8i) which confirms 1:1 frequency locking between these signals. However, pairs of other signals exhibit patterns with two lobes which are traditionally observed for 2:1 frequency locking between the signals. The traditional 2:1 Lissajous patterns

has lobes with equal shape and size (at least symmetric about one axis). However, we observe patterns with unequal shape and size due to the presence of higher harmonics in the experimental data. These results verify that the temporal dynamics has both 1:1 and 2:1 frequency locking behaviour during the state of TAI with period-2 limit cycle oscillations.

5.4 INTERIM SUMMARY

In this chapter, we analyzed the time series and looked at the coupled interaction between the temporal coefficients of dominant POD modes of velocity field along with acoustic pressure and heat release rate during different dynamical states including chaotic state-1 oscillations and thermoacoustic instabilities with period-1 and period-2 limit cycle oscillations. During the chaotic state-1 oscillations, all the signals except the temporal coefficient of first dominating mode exhibited the chaotic behaviour without any distinct peak in power spectra. The temporal coefficient of first dominating mode showed aperiodic behaviour and shows the dominance of frequencies with very low values. These signals exhibited non-analytical behaviour, that was verified using the Hilbert transformation. Therefore, phase for these temporal signals cannot be calculated using the Hilbert transformation.

During period-1 limit cycle oscillations, we discussed the 1:1 frequency locking

behaviour between the acoustic pressure and heat release rate fluctuations with the help of the phase portraits and first return maps. The 1:1 frequency locking is confirmed with the spiking signals for the local maximas in the acoustic pressure and heat release rate fluctuations. Using the temporal coefficients of first three dominating POD modes, the temporal signals investigated and showed that the temporal coefficients of only first two modes show period-1 behaviour, indicated that the first modes of velocity field dictate the flow dynamics in the combustor. Using the Lissajous patterns, we showed 1:1 frequency locking behaviour of flow velocity fluctuations with acoustic pressure and heat release rate fluctuations.

Furthermore, we showed 2:1 frequency locking behaviour between the acoustic pressure and heat release rate fluctuations, confirmed with the spiking signals during the state of TAI with period-2 limit cycle oscillations. Similar to period-1 limit cycle oscillations, the investigation of temporal coefficients showed that only first two modes of velocity field dictate the flow velocity field and exhibit period-2 behaviour. The third temporal coefficient exhibited non-analytic behaviour. We investigated the coupled behaviour of flow velocity and showed 1:1 2:1 frequency locking behaviours between flow velocity fluctuations with acoustic pressure and heat release rate fluctuations using the Lissajous patterns. Furthermore, we have corroborated that the presence of higher harmonics in

the signals induces alterations in both the size and configurations of patterns, exhibiting a stark departure from the traditional Lissajous patterns.

CHAPTER 6

COUPLED LARGE-SCALE STRUCTURES FROM FLOW, FLAME AND HEAT RELEASE RATE DISTRIBUTION FIELDS

In this chapter, we describe the percentage of turbulent kinetic in different POD modes and the spatial modes obtained using proper orthogonal decomposition (POD) and its extended version (EPOD) for the states of chaotic oscillations and thermoacoustic instabilities with period-1 and period-2 limit cycle oscillations. We also analyze the correlations between the structures from the flow, the flame and the heat release rate distribution fields.

Firstly, we disentangle large-scale coherent structures in the flow velocity field and their impact on the flame surface and heat release rate field by performing proper orthogonal decomposition (see section 3.3) and extended POD analysis (see section 3.4). Large-scale structures in turbulent flows contain majority of the turbulent kinetic energy which commences the cascade process and turbulence phenomenology. Thus, POD modes with the largest kinetic energy content along with correlated flame structures dominate the flow and flame dynamics. This can be observed simply by noting that the turbulent kinetic energy E and fluctuating kinetic energy E_i contained in each POD mode are

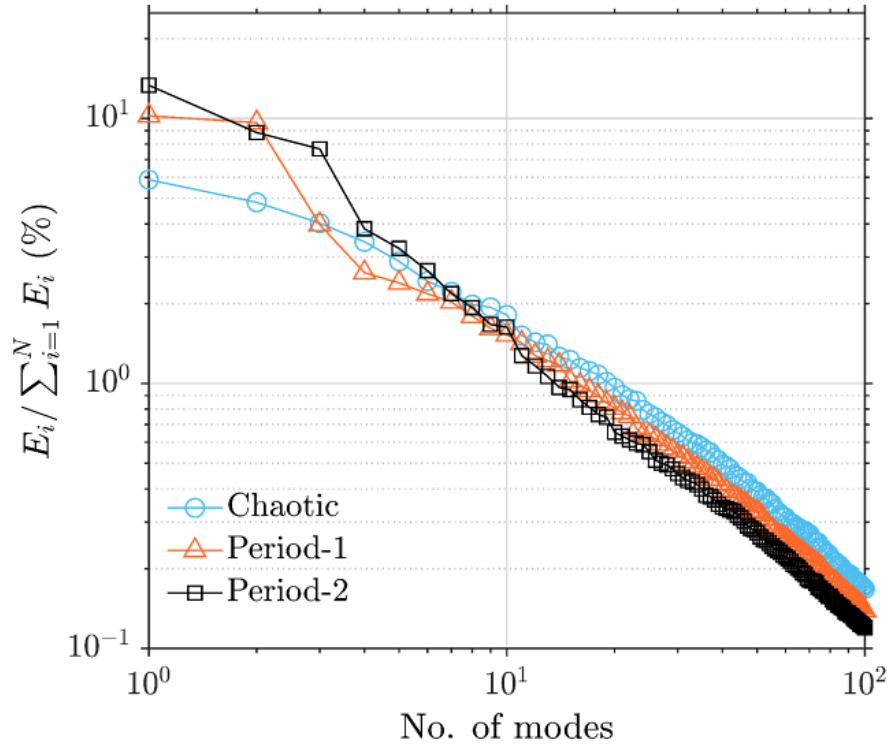


Figure 6.1: Fraction of the kinetic energy contained in the spectrum of POD modes (6.1) obtained from the flow velocity field (\mathbf{u}') for the three dynamical states highlighted in Table 3.1. The key role played by large-scale coherent structures during the states of thermoacoustic instabilities (period-1 and period-2) is depicted by the first two principal modes containing an order of magnitude higher kinetic energy than that observed during stable operation.

connected via the relations between the eigenvalues of the correlation matrix (3.16) and the flow field fluctuations:

$$E_i := \frac{1}{2} \overline{(\mathbf{u}', \Psi_i)^2} = \frac{1}{2} \lambda_i, \quad E = \sum_{i=1}^N E_i = \frac{1}{2} \sum_{i=1}^N \lambda_i. \quad (6.1)$$

Figure 6.1 shows the percentage of the turbulent kinetic energy (E_i/E) that the first 100 modes of the velocity field contain for different dynamical states. For all the cases, the first 100 modes contain over 90% of the turbulent kinetic energy, with the first

few principal modes accounting for a major fraction of the total kinetic energy. During chaotic oscillations, the first three POD modes contain 14.7% of the total kinetic energy. Further, for period-1 LCO, the first two modes contain 19.8% of the turbulent kinetic energy. The third mode contains an order of magnitude less fraction of the total energy. The energy content decreases drastically for higher POD modes. For period-2 LCO, the first three modes contain comparable proportion of the total kinetic energy, with the total amounting to around 29.8% of the total turbulent kinetic energy.

6.1 CHAOTIC OSCILLATIONS IN THE ABSENCE OF H₂

The flame and flow dynamics of the swirl combustor operating on CH₄ at $\phi = 0.65$ are shown in Fig. 6.2. The first row shows the mean of the transverse velocity component (\bar{u}_x), the flame brush obtained from time-averaged OH-PLIF imaging (\bar{I}_P) and the mean heat release rate obtained from OH*-chemiluminescence imaging (\bar{I}_C). The time averaging is performed over 3000 instantaneous images (or 0.3 seconds). Figure 6.2a shows high transverse velocity along the shear layers, with the opposite signs indicating the clockwise direction of the swirling flow. In addition, the flow shows low velocity fluctuations in the inner and the outer recirculation. Hence, the flame can be seen to stabilize along the inner shear layer, resulting in a characteristic V-shape of the turbulent flame brush (Fig. 6.2b). The thickness of the flame brush can also be seen to increase

downstream in comparison to the attachment point at the exit of the dump plane. As the chemiluminescence images are line-of-sight integrated in the out-of-plane direction, increased flame brush thickness can be seen to result in sustained, continuous band of heat release rate profile downstream of the combustor (Fig. 6.2c).

Figure 6.2d shows the first three POD modes of the transverse (u_x) velocity, together which account for 14.74% of TKE energy (Fig. 6.1). The first POD mode of the transverse velocity shows a coherent structure that grows in magnitude in the streamwise direction. The structure indicates a vortex bubble with positive velocity magnitude, depicting the overall direction of its motion. In contrast, mode 2 and mode 3 depict modes with same wavenumber and frequency, whose magnitude increases and then decays downstream. These structures are shifted in the streamwise direction by approximately quarter wavelength. Mode 2 and 3 are part of an oscillating process, linked to a helical mode instability around the recirculation bubble observed in POD mode 1. This can be observed in the Lissajous plot between mode coefficients $a_2 - a_3$ (Fig. 4.1). We further note here that the first three POD modes associated with u_y along the shear layer also indicate the presence of the same coherent structures with the same axial wavenumber with each mode shifted axially (Fig. 6.3). Additionally, all the three modes exhibit advection of the central recirculation zone.

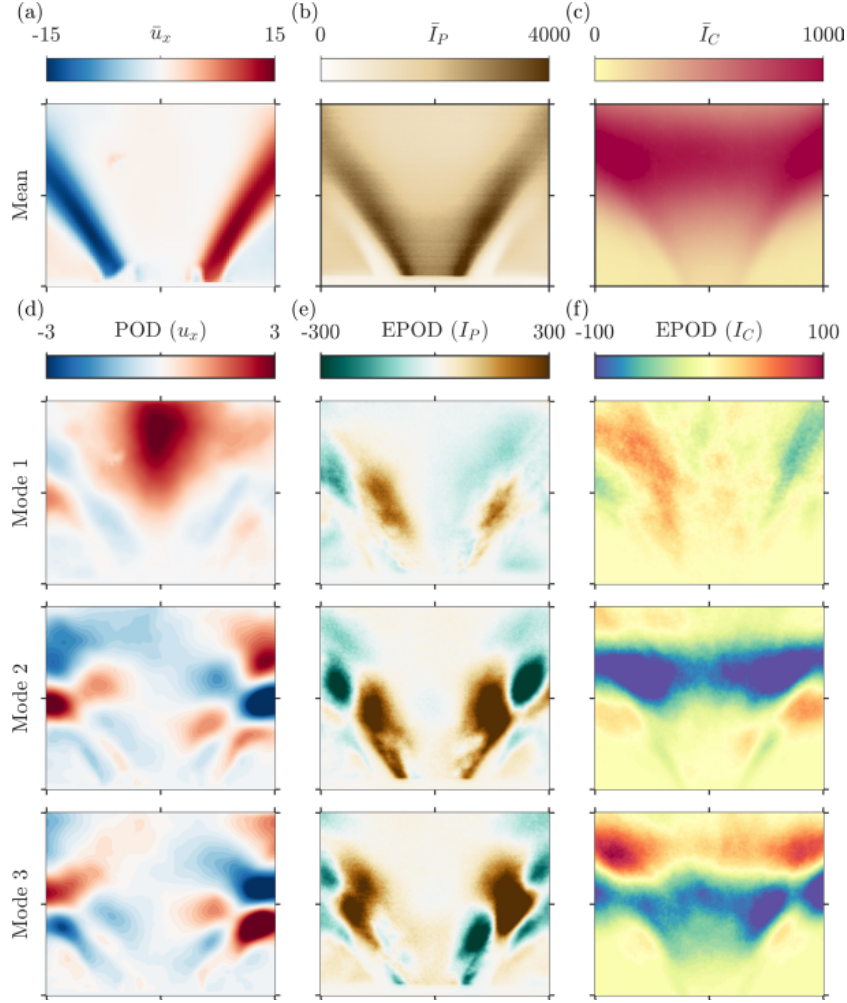


Figure 6.2: Flow and flame dynamics for the purely CH_4 -air flame for the baseline condition. Mean of the (a) transverse velocity component u_x , (b) flame brush obtained from OH-PLIF images, and (c) heat release rate fluctuations obtained from OH*-chemiluminescence. Panels (d-f) shows the first three POD modes of u'_x and the extended modes associated with I'_P and I'_C .

The extended POD modes of the flame profile (I_p) associated with the POD modes of u_x are also shown in Fig. 6.2e. We notice a number of salient features of the flame dynamics from the extended POD modes of the flame surface I_p in Fig. 6.2e. The dominant POD mode of u_x associated with the central recirculation bubble, does not correlate with extended POD modes of the flame surface. Only the small-scale structures along the shear layer are reflected in the extended POD modes of the flame

surface. This is due to the V-shaped flame (Fig. 6.2b) which stabilizes along the inner shear layer and does not extend into the inner recirculation zone. The increased activity in the flame surface is further emphasized in the second and third extended POD modes of the flame surface. The coherent structures present along the shear layer in the second and third POD modes of u_x are clearly correlated to the extended POD mode structures. The extended POD mode structure is also shifted by a quarter wavelength. The size of the structure can be seen to increase downstream of the flame attachment region, identifying regions contributing to the most of the changes in the flame dynamic. Interestingly, while the coherent structure is anti-symmetric (mode 2 & 3 in Fig. 6.2d) due to helicoidal instability in the flow field, the extended mode structure of the flame surface clearly retains axisymmetric.

The effect of these local flow and flame dynamics on the global heat release rate profile can be understood from the extended mode structure of the heat release rate distribution shown in Fig. 6.2f. As with the extended structure of flame surface, the first extended mode of heat release rate does not correlate with the central recirculating zone, corroborating the fact that the central vortex bubble arising due to the swirl does not affect the fluctuations in the heat release rate. The second and third extended modes on the other hand correlate well with the coherent structure present in the velocity

field. Indeed, we notice that structure of extended POD of heat release exists along the shear layers along with the extended mode structure of the flame surface. The second and third mode are again related to the same structure, only displaced by a quarter wavelength. The banded nature of these structures can be ascribed to the fact that the chemiluminescence imaging is line-of-sight integrated, revealing the annular region over which heat is release from the three dimensional flame structure. We note here that our observations remain the same when the axial velocity component u_y is used for obtaining extended POD modes from flame surface and heat release rate. These observations show that the structures from the heat release rate distribution and flame surface corresponding to the most dominant POD mode do not correlate. The coherent structures from other modes show some correlation with the structures from other fields. However, due to low turbulent kinetic energy of mode 2 and 3, their overall effect remains minimal.

In order to verify the differences in the EPOD modes based on transverse velocity component (u_x), we reconstructed the POD modes of the axial velocity for the state of chaotic oscillations. In Fig. 6.3, the first row shows the mean of the axial velocity component (\bar{u}_y), flame brush obtained from OH-PLIF images (\bar{I}_P) and the heat release rate obtained from OH*-chemiluminescence images (\bar{I}_C). Figure 6.3a shows the high

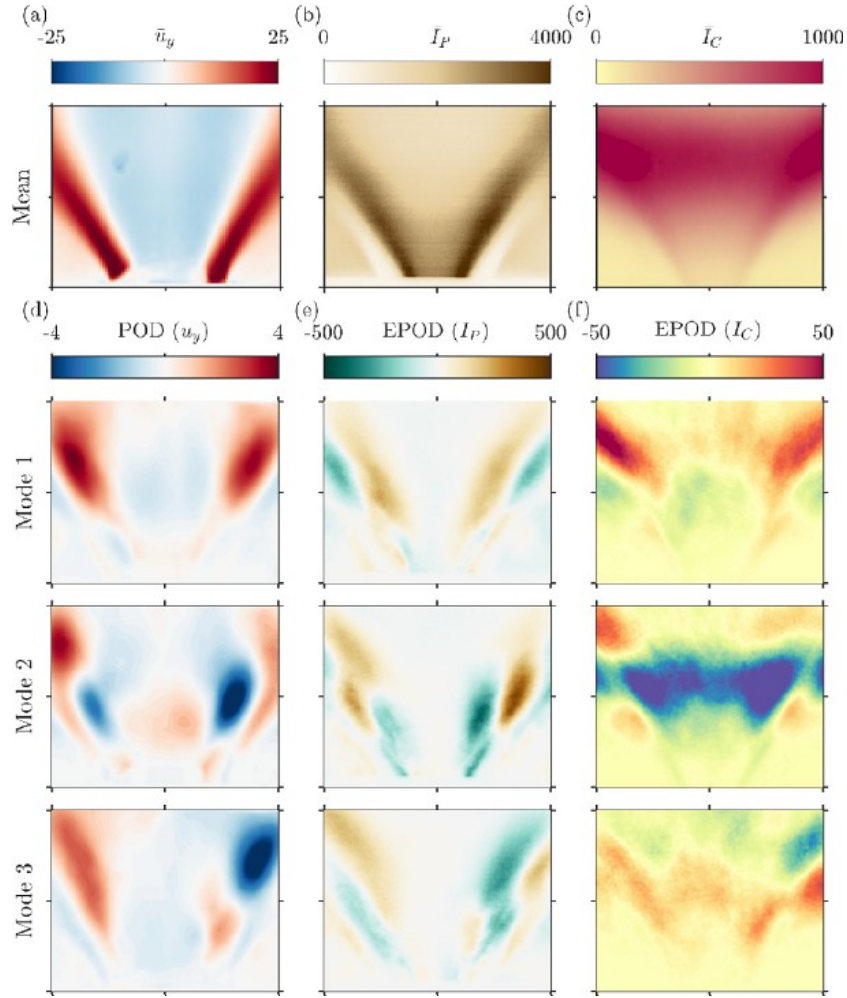


Figure 6.3: Flow and flame dynamics for the purely CH_4 -air flame. Mean of the (a) axial velocity component (u_y), (b) flame brush obtained from OH-PLIF images, and (c) heat release rate fluctuations obtained from OH*-chemiluminescence. Panels (d-f) shows the first three POD modes of u_y' and the extended POD modes associated with I_P' and I_C' .

velocity along the shear layers, elongated in the radial direction toward the wall of the combustor. In addition, the inner and the outer recirculation zones have low velocity fluctuations. The flame stabilises along the shear layers. The mean of the OH-PLIF intensity exhibits the V-shape of the flame, shown in Fig. 6.3b. with the increment in the flame brush thickness, most of the heat release rate occurs near the wall of the combustor (Fig. 6.3c) in the downstream.

Figure 6.3d shows the first POD mode of the axial component which has the high intensity structures along the shear layers, downstream of the combustor, indicating the swirling behaviour of the flow. These coherent structures grow in the axial direction and have high fluctuations near the wall of the combustor. Similarly, mode 2 and mode 3 exhibit coherent structures along the shear layers, having difference of approximately quarter wavelength (Fig. 6.3d). Moreover, the first EPOD mode of the flame surfaces (Fig. 6.3e) exhibits small scale structures along the shear layer. Further, in mode 2 and 3, we observe the structures near the inlet of the combustor (Fig. 6.3e). The first EPOD mode of the heat release rate distribution shows the structures along the shear layer near the wall of the combustion chamber (Fig. 6.3f). We also observe the structures in the EPOD modes of heat release rate distribution away from the inlet and near the wall of the combustor along the shear layers (Fig. 6.3f).

6.2 PERIOD-1 LIMIT CYCLE OSCILLATIONS AT 50% H₂ ENRICHMENT

The combustor shows the state of TAI with the addition of hydrogen (50%) at a constant equivalence ratio of $\phi = 0.65$ and a thermal power of $P = 20$ kW. We observe self-sustained, period-1 LCO with an amplitude of $p'_{\text{rms}} = 0.91$ kPa. Figure 6.4 shows the time-averaged velocity field, flame brush and heat released rate. Figure 6.4a shows high transverse velocity along the shear layers having opposite sign which indicates swirling

flow. The shear layer is much broader in comparison to the baseline case of the state of chaotic oscillations (Fig. 6.2). The flame also stabilizes along the shear layers and extends towards the outer recirculation zone, making it an M-shaped flame (Fig. 6.4b). The flame can be seen to be anchored very close to the dump plane. The time-averaged image of the heat release distribution field shows a concentrated region of high heat release rate. The location of the peak of \bar{I}_C is located much closer to the flame anchor point, in contrast to the baseline chaotic case where the peak occurred much further downstream.

Figure 6.4d shows the first three dominant POD modes associated with the transverse velocity fluctuations u'_x . These three modes collectively hold 30% of the total kinetic energy. The first and second POD modes indicate the presence of the same coherent structure in the form of a toroidal vortex of the same frequency and wavenumber. The modes can be seen to be shifted by a quarter of a wavelength and $\pi/2$ radians. In contrast to the baseline case, the dominant coherent structure during period-1 LCO comprises the helical toroidal vortex. The amplitude of the toroidal vortex can be observed to be much stronger than it was for the baseline case (cf. Fig. 6.2). The toroidal vortex can also be seen to extend to a much larger radial domain, with the anti-phase features alternating asymmetrically on each side of centre flow axis ($x = 0$). In

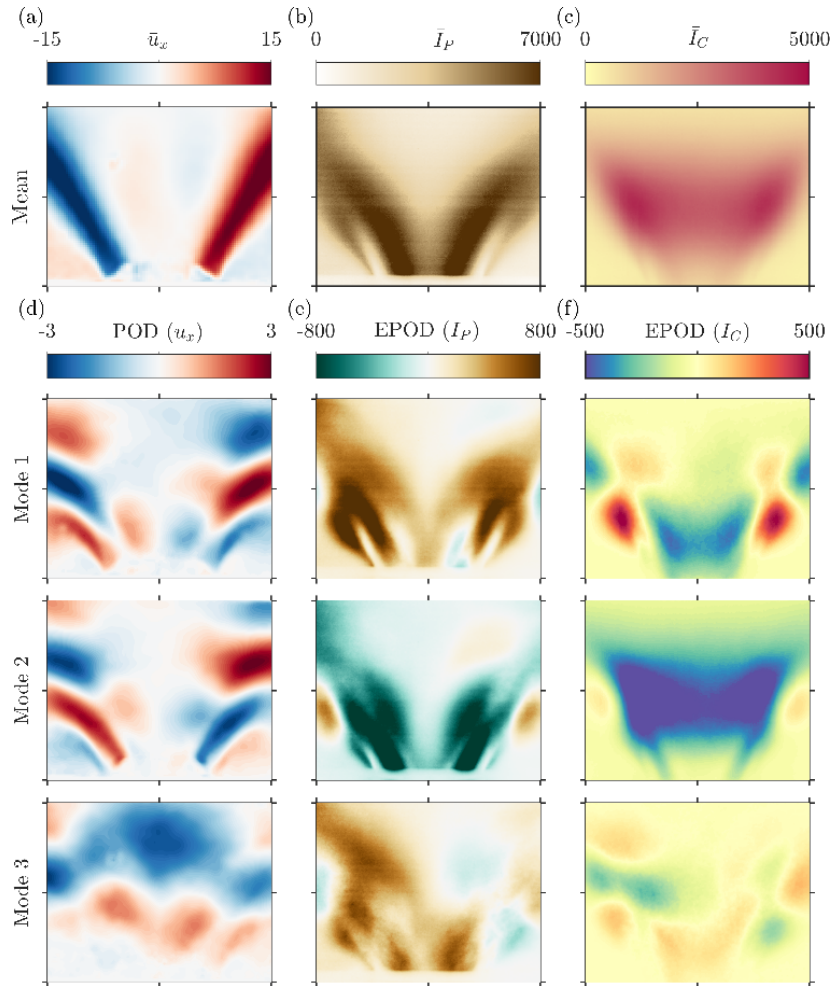


Figure 6.4: Flow and flame dynamics during Period-1 TAI with 50% hydrogen enrichment. Mean of the (a) transverse velocity component \bar{u}_x , (b) flame brush obtained from OH-PLIF images, and (c) heat release rate fluctuations obtained from OH*-chemiluminescence. Panels (d-f) shows the first three POD modes of u'_x and the extended modes associated with I'_P and I'_C .

addition to the toroidal vortex, the first two POD modes also show the presence of an anti-symmetric mode structure along the IRZ which convects in time. The third mode shows the presence of an axisymmetric coherent structure extending along the length of the combustor.

The extended POD modes of the flame surface is shown in Fig. 6.4e. For the first two

modes, we notice that the extended structure is distinctly M-shaped with branches of the flame surface extending along the nodal line of the toroidal as well as the inner coherent structure. The two extended modes, which are shifted by $\pi/2$ radians, are associated with positive and negative intensities, indicating the correlation between POD mode and the extended POD mode structure of the flame surface. In addition, the first and the second EPOD modes have the maximum intensity along the shear layers. However, we observe small scale structures in the third EPOD mode structure of the flame. Figure 6.4f present the EPOD modes of the heat release rate distribution. The first two EPOD modes show the structures in the IRZ and along the shear layer. The structures along shear layer confirm the existence of a toroidal vortex in the flow field (Fig. 6.4d). However, we do not observe the high intensity structure in the third EPOD modes of the OH-PLIF images and OH*-chemiluminescence. With the random arrangement of structures in the third extended modes of the flame surface and heat release rate, the coherent structures from the flow field do not correlate with the inner recirculating zone.

To understand the role of coherent structures from the axial velocity during the state of TAI, characterized with period-1 limit cycle oscillations, we show the spatial characteristics using the time-averaged mean of the axial velocity field, the flame surface and heat release rate distribution field (Fig. 6.5). We observe high velocity

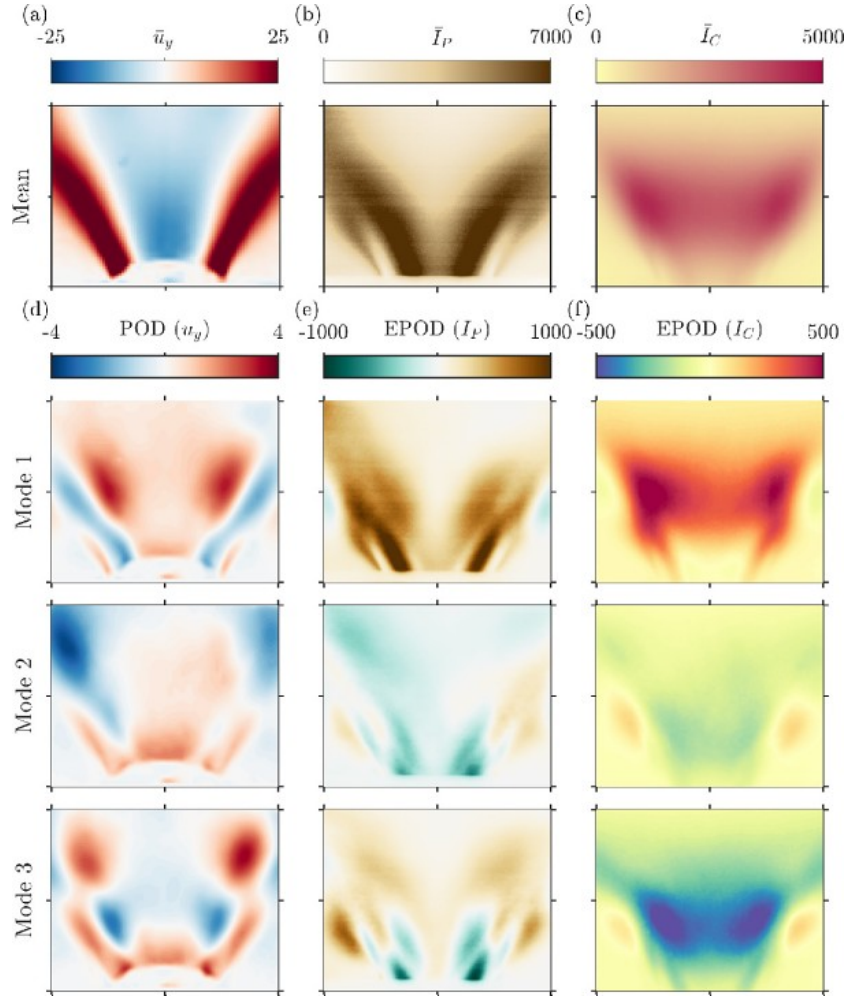


Figure 6.5: Flow and flame dynamics for 50% H₂-enriched CH₄-air flame. Mean of the (a) axial velocity component (u_y), (b) flame brush obtained from OH-PLIF images, and (c) heat release rate fluctuations obtained from OH*-chemiluminescence. Panels (d-f) shows the first three POD modes of u_y' and the extended POD modes associated with I_P' and I_C' .

fluctuations along the shear layer, shown in Fig. 6.5a. Moreover, we also see the velocity fluctuations in the inner recirculation zone. Simultaneously, we also notice the M-shape flame (Fig. 6.5b), anchored close to the dump plane of the combustor. Most of the heat release occurs in the inner recirculation zone (IRZ) and along the shear layers (Fig. 6.5c).

The first three modes of the axial component of velocity are shown in Fig. 6.5d. The oscillations in these modes are symmetric and are in-phase. In-phase refers the same velocity fluctuations in the coherent structures. All the modes show the high energy structures at the downstream of the combustor. Moreover, we also observe high velocity fluctuations in the inner recirculation zone, indicating the existence of toroidal vortex. The first and second EPOD modes of the flame surface have the maximum intensity along the shear layers (Fig. 6.5e), near the inlet of the combustor. However, we observed small scale structures in the third EPOD mode (Fig. 6.5e). Moreover, the first and third EPOD modes of the heat release rate distribution (OH*-chemiluminescence) field show structures along the shear layer and shows the presence of toroidal vortex (Fig. 6.5f). However, the second EPOD mode of heat release rate distribution field shows low intensity structures.

6.3 PERIOD-2 LIMIT CYCLE OSCILLATIONS AT 20% H2 ENRICHMENT

Let us now turn our attention to the coupled dynamics observed during the state of TAI with period-2 LCO when the combustor is operated at a constant equivalence ratio $\phi = 0.65$ and thermal power $P = 20$ kW with only 20% hydrogen. Like earlier, we plot the mean, POD modes and extended POD modes in Fig. 6.6.

In the mean transverse velocity field (Fig. 6.6a), we notice high velocity fluctuations

along the shear layers and the outer recirculation region (ORZ) with the opposite signs. The strength of fluctuations are lower than that observed during period-1 LCO (Fig. 6.4a). Moreover, the mean of the OH-PLIF image shows the presence of a columnar shaped flame having very high intensity stabilized along the inner recirculation zone of the combustor (Fig. 6.6b). Most of the heat release rate occurs along the inner recirculation zone and extends downstream of the combustor as shown in Fig. 6.6c. This is in contrast to the mean profile observed for the M-flame during period-1 oscillations (Fig. 6.4a). These results indicate that the flame surface shape and the heat release rate distribution are entirely changed from the state of period-1 LCO with small variation in the volume of hydrogen to the fuel.

To study the state of period-2 LCO thoroughly, the first three dominating POD modes of the transverse component are presented in Fig. 6.6d which cumulatively contains 23% of the total kinetic energy. The first two modes show that the coherent structures are symmetrically positioned on each side of the flow axis and have anti-phase behaviour. These coherent structures confirm the existence of the helical nature of the flow. Moreover, very low small-scale coherent structures with low velocity fluctuations can also be seen in IRZ. Unlike during period-1 LCO (Fig. 6.4d), the coherent structure can be seen to be limited only along the periphery and do not extend inwards along the shear

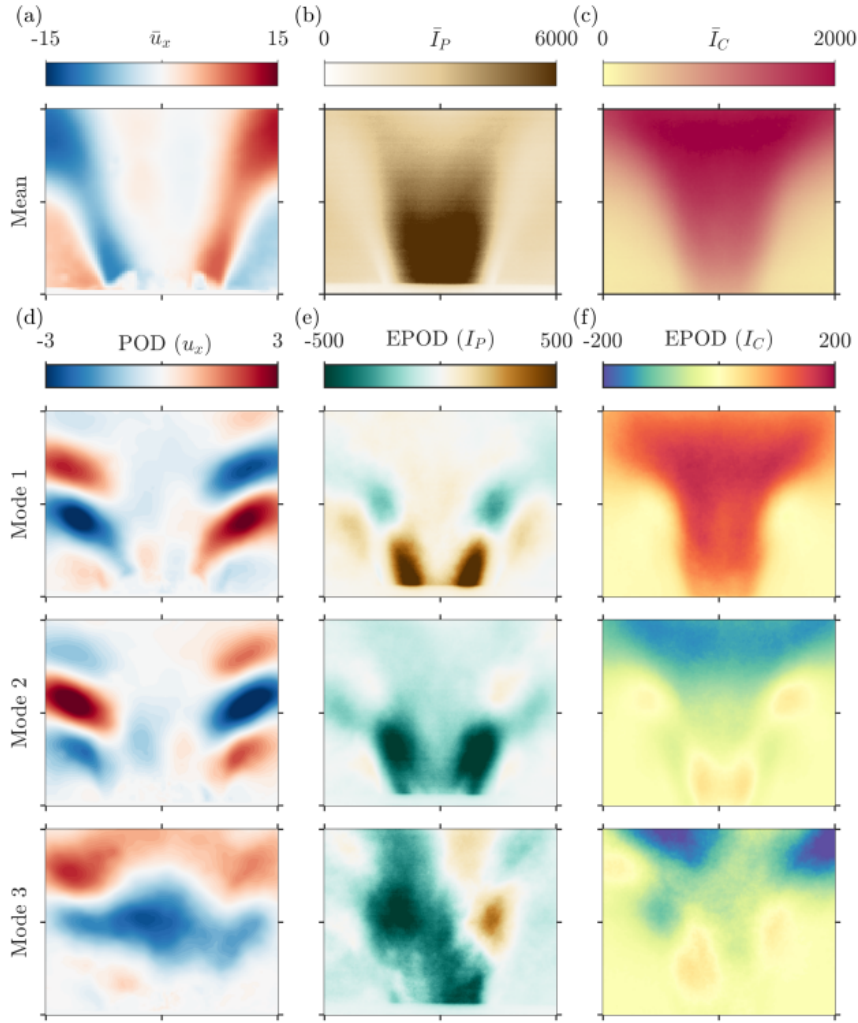


Figure 6.6: Mean of the (a) transverse velocity component u_x , (b) flame brush obtained from OH-PLIF images, and (c) heat release rate fluctuations obtained from OH*-chemiluminescence. Panels (d-f) shows the first three POD modes of u'_x and the extended modes associated with I'_P and I'_C . for the state of period-2 LCO with 20% hydrogen by volume of the fuel.

layer. However, the third mode shows the presence of a convecting structure along the axial direction (Fig. 6.6d). We also see similar elongated coherent structures in the POD modes of the axial velocity component (Fig. 6.7). These observations shows that the flow structures from the dominant modes confirm the existence of helical instability. However, the heat release rate field indicates that the maximum heat release occurs in

the IRZ and does not follow the path of the helical structures in the flow.

The EPOD modes of the flame surface corresponding to the first and second POD modes of the velocity field exhibit structures with high flame surface fluctuations along the shear layer near to the inlet of the combustor (Fig. 6.6e). That indicates a longer flame surface than that of in case of period-1 LCO due to low volume of hydrogen, as combustion with higher volume has smaller flame (Zhen *et al.*, 2012). The EPOD modes of the flame surface correlate well with the convecting coherent structure. Moreover, the third EPOD mode shows an asymmetrically distributed flame surface, convecting downstream with the flow (Fig. 6.6e). We also see similar structures near the IRZ in the extended modes of the flame surface using the axial velocity component of the flow (Fig. 6.7). The first two EPOD modes of the heat release rate distribution confirm that the maximum heat release rate occurs downstream of the combustor (Fig. 6.6f). The first two EPOD modes of heat release rate distribution are symmetrical about the axis at $x = 0$. Similar to the third EPOD mode of the OH-PLIF images, the structures occur without any pattern in the third EPOD mode of heat release rate distribution field. The results from the first two modes clarify that the spatial locations of the coherent structures do not match with the locations of structures from EPOD modes. The coherent structures in the POD modes of axial velocity component shares

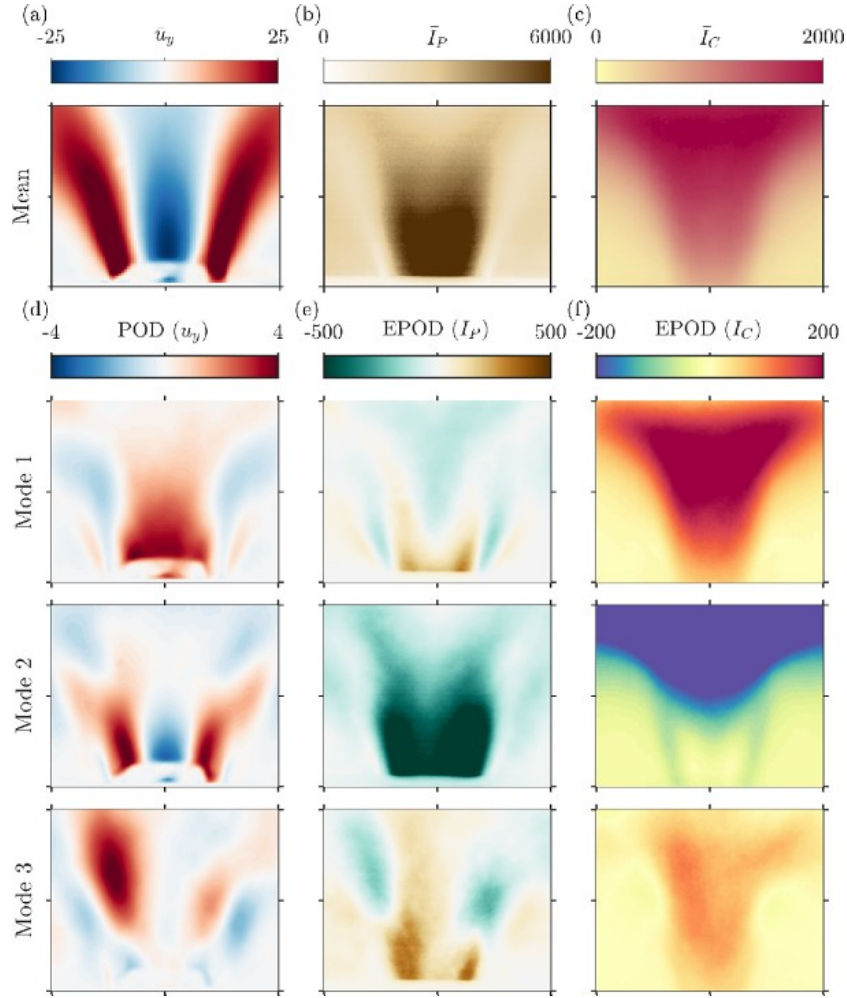


Figure 6.7: Flow and flame dynamics for 20% H₂-enriched CH₄-air flame. Mean of the (a) axial velocity component (u_y), (b) flame brush obtained from OH-PLIF images, and (c) heat release rate fluctuations obtained from OH*-chemiluminescence. Panels (d-f) shows the first three POD modes of u_y' and the extended POD modes associated with I_P' and I_C' .

the spatial positions with the structures from the corresponding EPOD of flame surface and heat release rate distribution fields (Fig. 6.7). Moreover, the structures from EPOD modes of flame surface and heat release rate distribution fields match.

In order to comprehend the effect of axial velocity component during the state of TAI with period-2 LCO, we plot the temporal mean of different spatial fields (Fig.

6.7). Figure 6.7a shows the high velocity oscillations along the shear layers and outer recirculation region (ORZ) in the mean velocity field. In Fig. 6.7b, the columnar shape flame having very high OH-PLIF intensity is observed near the inlet of the combustor. The most of the heat release rate occurs downstream of the combustor (Fig. 6.7c). Figure 6.7d show the first three dominating POD modes of the axial velocity modes. The first mode shows the high velocity fluctuations in the IRZ, anchored with the inlet of the combustor. We also observe structures with low energy along the shear layers (Fig. 6.7d), revealing the helical motion in the flow. The second POD mode shows high energy structures along the shear layers near the dump plane (Fig. 6.7d). The inner recirculation zone also exhibits high velocity fluctuations. Moreover, the third mode exhibits small as well as large structures along the shear layers. The first and second EPOD modes of the flame surface exhibit high intensity structures along the shear layer and in the inner recirculation zone near to the inlet of the combustor (Fig. 6.7e). The third EPOD mode shows small structures along the shear layers, indicating a longer flame surface (Fig. 6.7e). These structures correlate with the coherent structures of the axial velocity field. In Fig. 6.7f, the first and second EPOD of the heat release rate distribution field show that the most of the heat release rate occurs at downstream of the combustor, indicating the existence of toroidal vortex. In the third EPOD mode, we

observe some heat release rate occurring in a columnar shape at the IRZ (Fig. 6.7f), which is similar to the third EPOD of the flame surface.

6.4 INTERIM SUMMARY

In this chapter, we investigated the correlations between the dominating structures from different spatial fields (PIV, OH-PLIF and OH*-chemiluminescence) acquired simultaneously. We used proper orthogonal decomposition (POD) method to extract the dominant spatial modes of the flow velocity fields obtained through stereo-PIV. Additionally, the extended POD (EPOD) was utilized to determine the modes encompassing dominant structures within the OH-PLIF and OH*-chemiluminescence fields, corresponding to the POD modes observed within the velocity field.

During the state of chaotic oscillations, we showed using the mean of OH-PLIF field that the flame stabilizes along the inner shear layers and exhibits a V-shape. Using EPOD, our study revealed a notable absence of discernible correlations among the structures in the flow, the flame and the heat release rate distribution fields.

In the state of TAI characterized by period-1 limit cycle oscillations, the flame demonstrates stabilization along the shear layers and exhibits an M-shaped configuration, extending towards the outer recirculation zone. Additionally, our observations indicate a noteworthy association between the high-energy coherent

structures from flow field and the high-energy structures found on the flame surface and in the heat release rate distribution fields, as these structures manifest within the same spatial regions.

Moreover, we investigated thermoacoustic instability with period-2 limit cycle oscillations and noticed that the flame assumed a columnar morphology with significantly intensified characteristics, firmly stabilized along the inner recirculation zone of the combustor. Furthermore, we demonstrated a robust correlation between the structures identified on the flame surface and those discernible within the heat release rate field. However, it is noteworthy to mention that these structures contribute relatively less to the coherent structures observed in the velocity field.

CHAPTER 7

CONCLUSION AND SCOPE FOR FUTURE WORK

The enrichment of hydrogen in the fuel composition, specifically methane, induces alterations in the dynamics in a technically premixed turbulent combustor. With the addition of hydrogen in methane, we observe four major dynamical states exhibited by the combustor, i.e. chaotic oscillations (state-1 and states-2), intermittency, period-1 limit cycle oscillations and period-2 limit cycle oscillations. We use different methods including power spectrum analysis, reconstructed phase space analysis, and scalogram (graphical representation of continuous wavelet transformation) to detect these states from the experimental temporal and spatiotemporal data. By employing time series analysis and tools from synchronization theory, we provide the existence of 2:1 frequency locking between the acoustic pressure and heat release rate oscillations during the state of period-2 limit cycle oscillation state, which differs from the 1:1 frequency locking observed during period-1 limit cycle oscillation state. The occurrence of period-1 and period-2 limit cycle oscillations imposes different amplitude loading on the combustor walls, potentially necessitating additional structural reinforcements.

Firstly, we explain that the addition of hydrogen to the fuel under different operational conditions can induce or mitigate thermoacoustic instabilities or give rise to intricate

dynamics arising from the interaction among different modes. Furthermore, we show that at a specific operating conditions ($\mathcal{P} = 15$ kW and $\phi = 0.8$), an increase in hydrogen in the fuel causes the combustor to undergo a transition from a thermoacoustic instability state characterized by period-2 limit cycle oscillations to another state of thermoacoustic instability having period-1 limit cycle oscillations through chaotic oscillations.

Furthermore, we show that the flow and flame dynamics exhibit substantial variations contingent upon the prevailing dynamical state within the combustor. Specifically, when the combustor exhibits period-1 limit cycle oscillations, the flame intensity undergoes periodic shifts between the inner and outer shear layers. Conversely, during period-2 limit cycle oscillations, the flame primarily stabilizes within the inner recirculation zone, resulting in a markedly slender flame shape at its base. In comparison to period-1 limit cycle oscillations, we have observed that the region with the highest heat release rate moves downstream of the combustor during period-2 limit cycle oscillations.

Secondly, we present a comprehensive framework to analyze the synchronization characteristics of multiple concurrent flow parameters. This framework uses the extended proper orthogonal decomposition (POD) method to identify correlations between coherent structures observed in planar velocity field measurements and various

parameters such as heat-release rate distribution and flame surface. We utilize the POD technique to characterize the coherent structures present in the flow field and their corresponding temporal coefficients. Additionally, we describe the structures in the flame surface and heat-release rate distribution using the extended POD. This analysis is conducted under different dynamical states, including chaotic oscillations, thermoacoustic instability with period-1 and period-2 limit cycle oscillations.

We demonstrate that the temporal coefficients associated with the first two POD modes of flow velocity exert a dominant influence on the flow field during the states of period-1 and period-2 thermoacoustic instabilities. Furthermore, the phase portraits of pairs of distinct signal (acoustic pressure, heat release rate and temporal coefficients of first two POD modes of flow velocity) exhibit various patterns (similar to Lissajous patterns) and confirm a conspicuous 1:1 frequency locking phenomenon between the acoustic field, heat release rate, and flow field during period-1 limit cycle oscillations. Conversely, in the case of period-2 limit cycle oscillations, we observe both 1:1 and 2:1 frequency locking behaviors.

Finally, we elucidate the correlations among dominant structures derived from simultaneous acquisition of various spatial data through the application of extended proper orthogonal decomposition (EPOD). During the state of chaotic oscillations, we

hardly find correlations among the structures in the flow, the flame and heat release rate distribution fields. However, during the state of P1 LCO, we observe significant correlations between high-energy coherent structures and the corresponding structures in the flame surface and the heat release rate distribution fields, as the structures manifest in the same spatial regions. In the case of period-2 limit cycle oscillations, the structures from the flame surface are strongly correlated with the structures of the heat release rate field. However, the structures from flame and heat release rate distribution fields make less contribution to the coherent structures of the velocity field.

Thus, in this thesis, we have comprehensively demonstrated the temporal and spatiotemporal characteristics associated with various dynamical states resulting from the introduction of hydrogen into the fuel. We provide a framework to understand the synchronization of the flow velocity field with the acoustic pressure and the heat release rate distribution. Additionally, we find the correlations of the coherent structures in a flow field with the flame and heat release rate distribution field using the extended proper orthogonal modes of OH-PLIF images and OH*-chemiluminescence fields. These findings contribute to the fundamental understanding of the dominating structures exhibited in flow velocity and heat release rate distributions, thereby shedding light on the occurrence of different thermoacoustic instabilities that may manifest in practical

gas turbines.

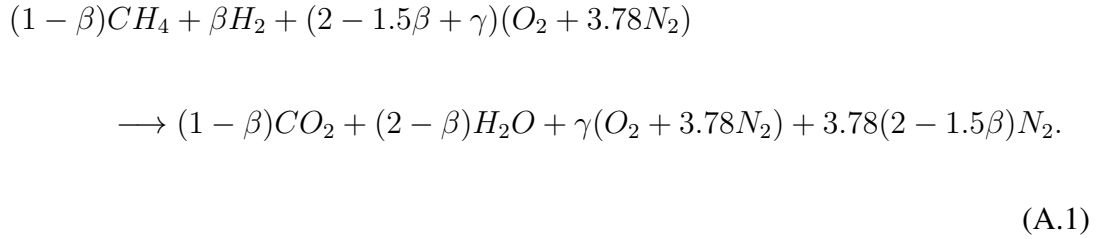
The present thesis opens up promising avenues for future research in the field of turbulent combustion. Notably, the investigation of correlations among dominating structures derived from simultaneous acquisition of various spatial data has yet to be explored in turbulent combustion studies. Additionally, acquiring a comprehensive understanding of the physical mechanisms governing the behavior of period-2 oscillations in various combustion systems is of paramount importance, given their occurrence in practical applications.

APPENDIX A

**GLOBAL EQUIVALENCE RATIO, THERMAL POWER
RATING AND VISCOSITY CALCULATION FOR A
 H_2 - CH_4 -AIR MIXTURE**

**A.1 CALCULATION OF GLOBAL EQUIVALENCE RATIO FOR H_2 - CH_4 -
AIR MIXTURE**

Various amounts of H_2 enrichment are investigated while keeping the same global equivalence ratio. By balancing the reaction of H_2 and CH_4 with extra air, the global equivalence ratio ϕ_g is determined (Halter *et al.*, 2005) which is based on the following equation:



where, γ is the amount of excess air in moles and β is the mole fraction of H_2 in the total mixture of CH_4 and H_2 , i.e., $\beta = N_{H_2}/(N_{H_2} + N_{CH_4})$. The global equivalence ratio is defined as:

$$\phi_g = \frac{(\dot{m}_a/\dot{m}_f)_{\text{stoich}}}{(\dot{m}_a/\dot{m}_f)_{\text{actual}}} = \frac{(\dot{m}_a/\dot{m}_f)_{\text{stoich}} \times (1 - \beta_m)MW_{CH_4} + \beta_m MW_{H_2}}{(2 - 1.5\beta_m + \gamma_m)(MW_{O_2} + 3.78MW_{N_2})} \quad (A.2)$$

Here we convert the mole based quantities such as β and γ into mass-based quantities, namely β_m and γ_m respectively. This conversion is made to use the mass flow rate of air and fuel directly to calculate the equivalence ratio.

A.2 DETERMINATION OF THERMAL POWER (\mathcal{P}) RATING FOR THE BURNER

On adding hydrogen with methane in various proportions, the thermal power generated by the combustor will vary. Using the mass flow rate of methane (\dot{m}_{CH_4}) and hydrogen (\dot{m}_{H_2}), we can determine the thermal power of the combustor with the following expression:

$$\mathcal{P} = (\dot{m}_{CH_4} * CV_{CH_4} + \dot{m}_{H_2} * CV_{H_2})/1000 \quad (\text{A.3})$$

where \mathcal{P} denotes the thermal power rating of the combustor in kW. CV_{CH_4} and CV_{H_2} are the higher calorific values of the methane (i.e., 55.5×10^6 J/Kg) and hydrogen (i.e., 141.7×10^6 J/Kg) at standard pressure and temperature (STP), i.e. $25^\circ C$ and 1 atm .

A.3 DETERMINATION OF NOMINAL REYNOLDS NUMBER (Re) H_2 - CH_4 -AIR MIXTURE

Due to variation of amount of CH_4 , H_2 and air, the nominal Reynolds number for each iteration changes and is calculated using the following expression:

$$Re = \frac{4\dot{m}_t}{\mu_m \pi L_c} \quad (\text{A.4})$$

where \dot{m}_t ($= \dot{m}_{CH_4} + \dot{m}_{H_2} + \dot{m}_a$) denoted the total mass flow rate in kg/s. μ_m is the dynamic viscosity of the mixture and its calculation is provides in Appendix A.4. The diameter of the inlet of the combustor chamber is used here as the characteristic length (L_c).

A.4 DETERMINATION OF VISCOSITY OF H_2 - CH_4 -AIR MIXTURE

The mixture viscosity of H_2 - CH_4 -air reactant is calculated (Wilke, 1950) using the following expression

$$\mu_m = \sum_i \frac{\mu_i}{1 + \sum_j x_j/x_i \Phi_{ij}}, \quad i, j = 1, 2, 3. \quad (\text{A.5})$$

where the indices i and j run over air, CH_4 and H_2 , μ_i is the kinematic viscosity and x_i the mole fraction of the i_{th} gas. The term Φ_{ij} involves the ratio of viscosity and molecular weight (M_i) of the different gases in the mixture. It is given in the general form (Wilke, 1950) as:

$$\Phi_{ij} = \frac{[1 + (\mu_i/\mu_j)^{1/2}(M_j/M_i)^{1/4}]^2}{(4/\sqrt{2})[1 + (M_i/M_j)]^{1/2}} \quad (\text{A.6})$$

The dynamic viscosity of the mixture measured from equation A.5 is then utilized for measuring the nominal Reynolds number Re using equation A.4.

APPENDIX B

ADIABATIC FLAME TEMPERATURE CALCULATION FOR A H_2 - CH_4 -AIR MIXTURE

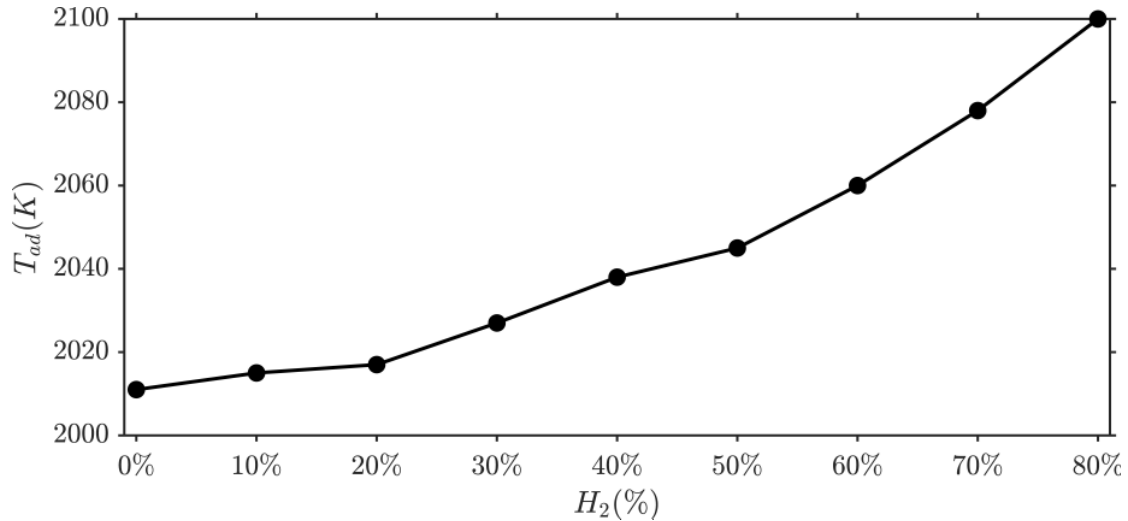


Figure B.1: Adiabatic flame temperature (in K) with increase HFF for the operating condition $\mathcal{P} = 15$ kW and $\phi = 0.8$.

We calculated the adiabatic flame temperature for all operating conditions investigated with increasing hydrogen fuel fraction (HFF) using the [GASEQ software](#). As we notice from figure B.1, with an increase in HFF for a particular thermal power ($P = 15$ kW) and equivalence ratio ($\phi = 0.8$), the adiabatic temperature of the flame continuously increases by about 100 K. As a result, the speed of sound also increases with the hydrogen-enrichment, leading to shift in the frequency of dominant modes of thermoacoustic oscillations to a higher value.

REFERENCES

1. **Abarbanel, H. D., R. Brown, J. J. Sidorowich, and L. S. Tsimring** (1993). The analysis of observed chaotic data in physical systems. *Reviews of modern physics*, **65**(4), 1331.
2. **Æsøy, E., J. G. Aguilar, S. Wiseman, M. R. Bothien, N. A. Worth, and J. R. Dawson** (2020). Scaling and prediction of transfer functions in lean premixed H₂/CH₄-flames. *Combust. Flame*, **215**, 269–282.
3. **Agostinelli, P., D. Laera, I. Chterev, I. Boxx, L. Gicquel, and T. Poinso** (2022). On the impact of H₂-enrichment on flame structure and combustion dynamics of a lean partially-premixed turbulent swirling flame. *Combustion and Flame*, **241**, 112120.
4. **Ananthkrishnan, N., S. Deo, and F. E. Culick** (2005). Reduced-order modeling and dynamics of nonlinear acoustic waves in a combustion chamber. *Combustion science and technology*, **177**(2), 221–248.
5. **Antoranz, A., A. Ianiro, O. Flores, and M. García-Villalba** (2018). Extended proper orthogonal decomposition of non-homogeneous thermal fields in a turbulent pipe flow. *International Journal of Heat and Mass Transfer*, **118**, 1264–1275.
6. **Aoki, C., H. Gotoda, S. Yoshida, and S. Tachibana** (2020). Dynamic behavior of intermittent combustion oscillations in a model rocket engine combustor. *Journal of Applied Physics*, **127**(22), 224903. DOI:<https://doi.org/10.1063/5.0001900>.
7. **Ashwin, P., I. Melbourne, and M. Nicol** (2001). Hypermeander of spirals: local bifurcations and statistical properties. *Physica D*, **156**(3-4), 364–382.
8. **Balachandran, R., B. Ayoola, C. Kaminski, A. Dowling, and E. Mastorakos** (2005). Experimental investigation of the nonlinear response of turbulent premixed flames to imposed inlet velocity oscillations. *Combust. Flame*, **143**(1-2), 37–55.
9. **Barenblatt, G., V. Librovich, and G. Makhviladze** (1985). The mathematical theory of combustion and explosions. *New York: Consultants Bureau*.
10. **Beita, J., M. Talibi, S. Sadasivuni, and R. Balachandran** (2021). Thermoacoustic instability considerations for high hydrogen combustion in lean premixed gas turbine combustors: A review. *Hydrogen*, **2**(1), 33–57.
11. **Bellows, B. D., M. K. Bobba, A. Forte, J. M. Seitzman, and T. Lieuwen** (2007). Flame transfer function saturation mechanisms in a swirl-stabilized combustor. *Proc. Combust. Inst.*, **31**(2), 3181–3188.
12. **Bénard, P., G. Lartigue, V. Moureau, and R. Mercier** (2019). Large-eddy simulation of the lean-premixed preceinsta burner with wall heat loss. *Proceedings of the Combustion Institute*, **37**(4), 5233–5243. DOI:<https://doi.org/10.1016/j.proci.2018.07.026>.

13. **Birbaud, A.-L., D. Durox, S. Ducruix, and S. Candel** (2007). Dynamics of confined premixed flames submitted to upstream acoustic modulations. *Proceedings of the Combustion Institute*, **31**(1), 1257–1265.
14. **Bloxside, G., A. Dowling, and P. Langhorne** (1988). Reheat buzz: an acoustically coupled combustion instability. part 2. theory. *Journal of fluid mechanics*, **193**, 445–473.
15. **Borée, J.** (2003). Extended proper orthogonal decomposition: a tool to analyse correlated events in turbulent flows. *Experiments in fluids*, **35**(2), 188–192.
16. **Boxx, I., M. Stöhr, C. Carter, and W. Meier** (2010). Temporally resolved planar measurements of transient phenomena in a partially pre-mixed swirl flame in a gas turbine model combustor. *Combust. Flame*, **157**(8), 1510–1525.
17. **Candel, S.** (2002). Combustion dynamics and control: progress and challenges. *Proceedings of the combustion institute*, **29**(1), 1–28.
18. **Cao, L.** (1997). Practical method for determining the minimum embedding dimension of a scalar time series. *Physica D: Nonlinear Phenomena*, **110**(1-2), 43–50.
19. **Cellek, M. S. and A. Pınarbaşı** (2018). Investigations on performance and emission characteristics of an industrial low swirl burner while burning natural gas, methane, hydrogen-enriched natural gas and hydrogen as fuels. *International Journal of Hydrogen Energy*, **43**(2), 1194–1207.
20. **Chiesa, P., G. Lozza, and L. Mazzocchi** (2005). Using hydrogen as gas turbine fuel. *J. Eng. Gas Turbines Power*, **127**(1), 73–80.
21. **Chtere, I. and I. Boxx**, Flame topology and combustion instability limits of lean premixed hydrogen enriched flames. In *27th International Colloquium on the Dynamics of Explosions and Reactive Systems, July 28 - August 2, Beijing, China*. 2019. DOI:<https://elib.dlr.de/130096/>.
22. **Chtere, I. and I. Boxx** (2020). Effect of hydrogen enrichment on the dynamics of a lean technically premixed elevated pressure flame. *Combustion and Flame*, **225**, 149–159.
23. **Chtere, I. and I. Boxx** (2021). Effect of hydrogen enrichment on the dynamics of a lean technically premixed elevated pressure flame. *Combustion and Flame*, **225**, 149–159.
24. **Chu, B.-T.** (1965). On the energy transfer to small disturbances in fluid flow (part i). *Acta Mechanica*, **1**(3), 215–234.
25. **Correa, S. M.** (1993). A review of NO_x formation under gas-turbine combustion conditions. *Combustion science and technology*, **87**(1-6), 329–362.
26. **Culick, F.** (1994). Some recent results for nonlinear acoustics in combustion chambers. *AIAA journal*, **32**(1), 146–169. DOI: 10.2514/3.11962.

27. **Culick, F.** and **V. Burnley**, The influences of noise on acoustic instabilities. *In 34th JANNAF Combustion Meeting*. 1999.
28. **Culick, F.** and **P. Kuentzmann** (2006). Unsteady motions in combustion chambers for propulsion systems. Technical report, NATO RESEARCH AND TECHNOLOGY ORGANIZATION NEUILLY-SUR-SEINE (FRANCE).
29. **Datta, S., S. Mondal, A. Mukhopadhyay, D. Sanyal, and S. Sen** (2009). An investigation of nonlinear dynamics of a thermal pulse combustor. *Combustion Theory and Modelling*, **13**(1), 17–38.
30. **Davis, D. W., P. L. Therkelsen, D. Littlejohn, and R. K. Cheng** (2013). Effects of hydrogen on the thermo-acoustics coupling mechanisms of low-swirl injector flames in a model gas turbine combustor. *Proceedings of the Combustion Institute*, **34**(2), 3135–3143.
31. **de Paula, A. V.** and **S. V. Möller** (2018). On the chaotic nature of bistable flows. *Experimental Thermal and Fluid Science*, **94**, 172–191.
32. **Di Sarli, V., A. Di Benedetto, E. J. Long, and G. K. Hargrave** (2012). Time-resolved particle image velocimetry of dynamic interactions between hydrogen-enriched methane/air premixed flames and toroidal vortex structures. *international journal of hydrogen energy*, **37**(21), 16201–16213.
33. **Dowling, A. P.** (1997). Nonlinear self-excited oscillations of a ducted flame. *Journal of fluid mechanics*, **346**, 271–290.
34. **Dowling, A. P.** and **Y. Mahmoudi** (2015). Combustion noise. *Proceedings of the Combustion Institute*, **35**(1), 65–100.
35. **Dutta, A. K., G. Ramachandran, and S. Chaudhuri** (2019). Investigating thermoacoustic instability mitigation dynamics with a kuramoto model for flamelet oscillators. *Physical Review E*, **99**(3), 032215. DOI:<https://doi.org/10.1103/PhysRevE.99.032215>.
36. **Duwig, C.** and **P. Iudiciani** (2010). Extended proper orthogonal decomposition for analysis of unsteady flames. *Flow, turbulence and combustion*, **84**(1), 25–47. DOI:<https://doi.org/10.1007/s10494-009-9210-6>.
37. **Elias, L., E. Ogryzlo, and H. Schiff** (1959). The study of electrically discharged o₂ by means of an isothermal calorimetric detector. *Canadian Journal of Chemistry*, **37**(10), 1680–1689.
38. **Emadi, M., D. Karkow, T. Salameh, A. Gohil, and A. Ratner** (2012). Flame structure changes resulting from hydrogen-enrichment and pressurization for low-swirl premixed methane–air flames. *International Journal of Hydrogen Energy*, **37**(13), 10397–10404.
39. **Figura, L., J. G. Lee, B. D. Quay, and D. A. Santavicca**, The effects of fuel composition on flame structure and combustion dynamics in a lean premixed combustor. *In Turbo Expo: Power for Land, Sea, and Air*, volume 47918. 2007. 10.1115/GT2007-27298.

40. **Filomeno, G., T. Capurso, M. Torresi, and G. Pascazio**, Numerical study of the lean premixed precessing burner with hydrogen enrichment. *In E3S Web of Conferences*, volume 312. EDP Sciences, 2021.
41. **Fiorina, B., R. Vicquelin, P. Auzillon, N. Darabiha, O. Gicquel, and D. Veynante** (2010). A filtered tabulated chemistry model for lean premixed combustion. *Combustion and Flame*, **157**(3), 465–475.
42. **Foust, M., D. Thomsen, R. Stickles, C. Cooper, and W. Dodds**, Development of the ge aviation low emissions turbo combustor for next generation aircraft engines. *In 50th AIAA aerospace sciences meeting including the new horizons forum and aerospace exposition*. 2012.
43. **Fraser, A. M. and H. L. Swinney** (1986). Independent coordinates for strange attractors from mutual information. *Physical review A*, **33**(2), 1134.
44. **George, N. B., V. R. Unni, M. Raghunathan, and R. I. Sujith** (2018). Pattern formation during transition from combustion noise to thermoacoustic instability via intermittency. *Journal of Fluid Mechanics*, **849**, 615–644.
45. **Gharekhan, A. H., S. Arora, P. K. Panigrahi, and A. Pradhan** (2010). Distinguishing cancer and normal breast tissue autofluorescence using continuous wavelet transform. *IEEE Journal of Selected Topics in Quantum Electronics*, **16**(4), 893–899.
46. **Gotoda, H., H. Nikimoto, T. Miyano, and S. Tachibana** (2011). Dynamic properties of combustion instability in a lean premixed gas-turbine combustor. *Chaos: An Interdisciplinary Journal of Nonlinear Science*, **21**(1), 013124.
47. **Gotoda, H., Y. Shinoda, M. Kobayashi, Y. Okuno, and S. Tachibana** (2014). Detection and control of combustion instability based on the concept of dynamical system theory. *Phys. Rev. E*, **89**(2), 022910.
48. **Gottwald, G. A. and I. Melbourne** (2004). A new test for chaos in deterministic systems. *Proceedings of the Royal Society of London. Series A: Mathematical, Physical and Engineering Sciences*, **460**(2042), 603–611. DOI:<https://doi.org/10.1098/rspa.2003.1183>.
49. **Gottwald, G. A. and I. Melbourne** (2009). On the implementation of the 0–1 test for chaos. *SIAM Journal on Applied Dynamical Systems*, **8**(1), 129–145.
50. **Greenslade Jr, T. B.** (1993). All about Lissajous figures. *Phys. Teach*, **31**(6), 364–370.
51. **Guo, H., B. Tayebi, C. Galizzi, and D. Escudie** (2010). Burning rates and surface characteristics of hydrogen-enriched turbulent lean premixed methane–air flames. *International journal of hydrogen energy*, **35**(20), 11342–11348.
52. **Halter, F., C. Chauveau, N. Djebaili-Chaumeix, and I. Gökalp** (2005). Characterization of the effects of pressure and hydrogen concentration on laminar burning velocities of methane–hydrogen–air mixtures. *Proceedings of the Combustion Institute*, **30**(1), 201–208.

53. **Halter, F., C. Chauveau, and I. Gökalp** (2007). Characterization of the effects of hydrogen addition in premixed methane/air flames. *International Journal of Hydrogen Energy*, **32**(13), 2585–2592.
54. **Hawkes, E. R. and J. H. Chen** (2004). Direct numerical simulation of hydrogen-enriched lean premixed methane–air flames. *Combustion and Flame*, **138**(3), 242–258.
55. **He, L., Q. Guo, Y. Gong, F. Wang, and G. Yu** (2019). Investigation of oh* chemiluminescence and heat release in laminar methane–oxygen co-flow diffusion flames. *Combustion and Flame*, **201**, 12–22.
56. **Heckl, M. A.** (1988). Active control of the noise from a rijke tube. *Journal of Sound and Vibration*, **124**(1), 117–133.
57. **Hegger, R., H. Kantz, F. Schmüser, M. Diestelhorst, R.-P. Kapsch, and H. Beige** (1998). Dynamical properties of a ferroelectric capacitor observed through nonlinear time series analysis. *Chaos: An Interdisciplinary Journal of Nonlinear Science*, **8**(3), 727–736.
58. **Higgins, B.** (1802). On the sound produced by a current of hydrogen gas passing through a tube. *Journal of natural philosophy, chemistry and the arts*, **1**(129-131), 2.
59. **Hong, S., S. J. Shanbhogue, R. L. Speth, and A. F. Ghoniem** (2013). On the phase between pressure and heat release fluctuations for propane/hydrogen flames and its role in mode transitions. *Combustion and Flame*, **160**(12), 2827–2842.
60. **Ilbas, M., A. P. Crayford, I. Yilmaz, P. J. Bowen, and N. Syred** (2006). Laminar-burning velocities of hydrogen–air and hydrogen–methane–air mixtures: an experimental study. *International Journal of Hydrogen Energy*, **31**(12), 1768–1779.
61. **International Energy Agency, I. E. A. and W. Bank**, *Sustainable Energy for All 2013-2014: Global Tracking Framework Report*. The World Bank, 2014.
62. **Jackson, G. S., R. Sai, J. M. Plaia, C. M. Boggs, and K. T. Kiger** (2003). Influence of H₂ on the response of lean premixed CH₄ flames to high strained flows. *Combustion and Flame*, **132**(3), 503–511. DOI: 10.1016/S0010-2180(02)00496-0.
63. **Jahnke, C. C. and F. E. Culick** (1994). Application of dynamical systems theory to nonlinear combustion instabilities. *Journal of propulsion and power*, **10**(4), 508–517.
64. **Jansohn, P.**, Overview of gas turbine types and applications. *In Modern Gas Turbine Systems*. Elsevier, 2013, 21–43.
65. **Janus, M. C., G. A. Richards, M. J. Yip, and E. H. Robey**, Effects of ambient conditions and fuel composition on combustion stability. *In Turbo Expo: Power for Land, Sea, and Air*, volume 78699. American Society of Mechanical Engineers, 1997.
66. **Julian, M.** (2000). Marpol 73/78: the international convention for the prevention of pollution from ships. *Maritime Studies*, **2000**(113), 16–23.

67. **Juniper, M. P.** and **R. I. Sujith** (2018). Sensitivity and nonlinearity of thermoacoustic oscillations. *Annu. Rev. Fluid Mech.*, **50**, 661–689.
68. **Kabiraj, L., A. Saurabh, P. Wahi,** and **R. I. Sujith** (2012a). Route to chaos for combustion instability in ducted laminar premixed flames. *Chaos: An Interdisciplinary Journal of Nonlinear Science*, **22**(2), 023129. DOI:10.1063/1.4718725.
69. **Kabiraj, L., R. Sujith,** and **P. Wahi** (2012b). Investigating the dynamics of combustion-driven oscillations leading to lean blowout. *Fluid Dynamics Research*, **44**(3), 031408.
70. **Kabiraj, L.** and **R. I. Sujith** (2012). Nonlinear self-excited thermoacoustic oscillations: intermittency and flame blowout. *J. Fluid Mech.*, **713**, 376–397.
71. **Karakaya, E., C. Nuur,** and **L. Assbring** (2018). Potential transitions in the iron and steel industry in sweden: towards a hydrogen-based future? *Journal of cleaner production*, **195**, 651–663.
72. **Karbasi, M.** and **I. Wierzba** (1998). The effects of hydrogen addition on the stability limits of methane jet diffusion flames. *International Journal of Hydrogen Energy*, **23**(2), 123–129.
73. **Kashinath, K., S. Hemchandra,** and **M. P. Juniper** (2013). Nonlinear thermoacoustics of ducted premixed flames: The influence of perturbation convection speed. *Combustion and Flame*, **160**(12), 2856–2865.
74. **Kashinath, K., I. C. Waugh,** and **M. Juniper** (2014). Nonlinear self-excited thermoacoustic oscillations of a ducted premixed flame: bifurcations and routes to chaos. *Journal of Fluid Mechanics*. DOI:.
75. **Kaskan, W.** and **A. Noreen** (1955). High-frequency oscillations of a flame held by a bluff body. *ASME Transactions*, **77**(6), 855–891.
76. **Kennel, M. B., R. Brown,** and **H. D. Abarbanel** (1992). Determining embedding dimension for phase-space reconstruction using a geometrical construction. *Physical review A*, **45**(6), 3403.
77. **Kim, H. S., V. K. Arghode, M. B. Linck,** and **A. K. Gupta** (2009). Hydrogen addition effects in a confined swirl-stabilized methane-air flame. *International journal of hydrogen energy*, **34**(2), 1054–1062. DOI: 10.1016/j.ijhydene.2008.10.034.
78. **King, L. V.** (1914). Xii. on the convection of heat from small cylinders in a stream of fluid: Determination of the convection constants of small platinum wires with applications to hot-wire anemometry. *Philosophical transactions of the royal society of London. series A, containing papers of a mathematical or physical character*, **214**(509-522), 373–432.
79. **Kochenburger, R. J.** (1950). A frequency response method for analyzing and synthesizing contactor servomechanisms. *Transactions of the American Institute of Electrical Engineers*, **69**(1), 270–284.

80. **Kuhlmann, J., A. Lampmann, M. Pfitzner, and W. Polifke** (2022). Assessing accuracy, reliability, and efficiency of combustion models for prediction of flame dynamics with large eddy simulation. *Physics of Fluids*, **34**(9).
81. **Landau, L. D.**, On the problem of turbulence. In *Dokl. Akad. Nauk USSR*, volume 44. 1944.
82. **Lazik, W., T. Doerr, S. v. Bake, R. vd Bank, and L. Rackwitz**, Development of lean-burn low-NOx combustion technology at rolls-royce deutschland. In *Turbo Expo: Power for Land, Sea, and Air*, volume 43130. 2008.
83. **Lee, T. and K. T. Kim** (2020). Combustion dynamics of lean fully-premixed hydrogen-air flames in a mesoscale multinozzle array. *Combust. Flame*, **218**, 234–246.
84. **Lei, S. and A. Turan** (2009). Nonlinear/chaotic behaviour in thermo-acoustic instability. *Combustion Theory and Modelling*, **13**(3), 541–557.
85. **Li, L. K. and M. P. Juniper** (2013). Lock-in and quasiperiodicity in a forced hydrodynamically self-excited jet. *Journal of Fluid Mechanics*, **726**, 624–655.
86. **Lieuwen, T. and Y. Neumeier** (2002). Nonlinear pressure-heat release transfer function measurements in a premixed combustor. *Proceedings of the Combustion Institute*, **29**(1), 99–105.
87. **Lieuwen, T., Y. Neumeier, and B. T. Zinn** (1998). The role of unmixedness and chemical kinetics in driving combustion instabilities in lean premixed combustors. *Combustion Science and Technology*, **135**(1-6), 193–211.
88. **Lieuwen, T., H. Torres, C. Johnson, and B. Zinn** (2001). A mechanism of combustion instability in lean premixed gas turbine combustors. *J. Eng. Gas Turbines Power*, **123**(1), 182–189.
89. **Lieuwen, T. C.** (2002). Experimental investigation of limit-cycle oscillations in an unstable gas turbine combustor. *Journal of Propulsion and Power*, **18**(1), 61–67.
90. **Lieuwen, T. C.**, *Unsteady combustor physics*. Cambridge University Press, 2021.
91. **Lieuwen, T. C. and V. Yang**, *Combustion instabilities in gas turbine engines: operational experience, fundamental mechanisms, and modeling*. American Institute of Aeronautics and Astronautics, 2005.
92. **Liu, Y., J. Tan, M. Wan, L. Zhang, and X. Yao** (2020). Quantitative measurement of OH^* and CH^* chemiluminescence in jet diffusion flames. *ACS omega*, **5**(26), 15922–15930.
93. **Lohrasbi, S., R. Hammer, W. Essl, G. Reiss, S. Defregger, and W. Sanz** (2021). A modification to extended proper orthogonal decomposition-based correlation analysis: The spatial consideration. *Int. J. Heat Mass Transfer*, **175**, 121065. DOI: 10.1016/j.ijheatmasstransfer.2021.121065.

94. **Lumley, J. L.** (1967). The structure of inhomogeneous turbulent flows. *Atmospheric turbulence and radio wave propagation*, 166–178.
95. **Matveev, K. I.** and **F. Culick** (2003). A model for combustion instability involving vortex shedding. *Combustion Science and Technology*, **175**(6), 1059–1083.
96. **McManus, K. R., T. Poinso**t, and **S. M. Candel** (1993). A review of active control of combustion instabilities. *Progress in Energy and Combustion Science*, **19**(1), 1–29.
97. **Meier, W., P. Weigand, X. Duan,** and **R. Giezendanner-Thoben** (2007). Detailed characterization of the dynamics of thermoacoustic pulsations in a lean premixed swirl flame. *Combustion and Flame*, **150**(1-2), 2–26. DOI:10.1016/j.combustflame.2007.04.002.
98. **Milnor, J.** (1985). On the concept of attractor. *Communications in Mathematical Physics*, **99**, 177–195.
99. **Mitra, S. K.,** *Digital signal processing: a computer-based approach.* McGraw-Hill Higher Education, 2001.
100. **Mondal, S., S. A. Pawar,** and **R. I. Sujith** (2017). Synchronous behaviour of two interacting oscillatory systems undergoing quasiperiodic route to chaos. *Chaos: An Interdisciplinary Journal of Nonlinear Science*, **27**(10), 103119.
101. **Mondal, S., S. A. Pawar,** and **R. I. Sujith,** Synchronization transition in a thermoacoustic system: Temporal and spatiotemporal analyses. *In Energy for Propulsion.* Springer, 2018, 125–150.
102. **Murugesan, M.** and **R. I. Sujith** (2015). Combustion noise is scale-free: transition from scale-free to order at the onset of thermoacoustic instability. *Journal of Fluid Mechanics*, **772**, 225–245.
103. **Nair, V.** and **R. Sujith** (2015). A reduced-order model for the onset of combustion instability: physical mechanisms for intermittency and precursors. *Proceedings of the combustion institute*, **35**(3), 3193–3200.
104. **Nair, V.** and **R. I. Sujith** (2014). Multifractality in combustion noise: predicting an impending combustion instability. *Journal of Fluid Mechanics*, **747**, 635–655.
105. **Nair, V., G. Thampi, S. Karuppusamy, S. Gopalan,** and **R. I. Sujith** (2013). Loss of chaos in combustion noise as a precursor of impending combustion instability. *Int. J. Spray. Comb. Dyn.*, **5**(4), 273–290.
106. **Nair, V., G. Thampi,** and **R. I. Sujith** (2014). Intermittency route to thermoacoustic instability in turbulent combustors. *Journal of Fluid Mechanics*, **756**, 470.
107. **Nakata, T., M. Sato,** and **T. Hasegawa** (1998). Reaction of fuel NO_x formation for gas turbine conditions.
108. **Nayfeh, A. H.** and **B. Balachandran,** *Applied nonlinear dynamics: analytical, computational, and experimental methods.* John Wiley & Sons, 2008.

109. **Noiray, N., D. Durox, T. Schuller, and S. Candel** (2008). A unified framework for nonlinear combustion instability analysis based on the flame describing function. *Journal of Fluid Mechanics*, **615**, 139–167. DOI:10.1017/S0022112008003613.
110. **NPTELHRD** (2012). Title. URL https://www.youtube.com/watch?v=IGXtrzu8zb8&list=PLbMVogVj5nJSHp0t4uPZBv9I-e7CTgV0t&index=32&ab_channel=npTELHRD.
111. **Oates, G. C.**, *The aerothermodynamics of aircraft gas turbine engines*, volume 2, chapter Afterburners. AIAA, 1978, 45–144.
112. **Oberleithner, K., M. Stöhr, S. H. Im, C. M. Arndt, and A. M. Steinberg** (2015). Formation and flame-induced suppression of the precessing vortex core in a swirl combustor: experiments and linear stability analysis. *Combustion and Flame*, **162**(8), 3100–3114.
113. **Otto, A., M. Robinius, T. Grube, S. Schiebahn, A. Praktiknjo, and D. Stolten** (2017). Power-to-steel: Reducing CO₂ through the integration of renewable energy and hydrogen into the German steel industry. *Energies*, **10**(4), 451.
114. **Palies, P., M. Ilak, and R. Cheng** (2017). Transient and limit cycle combustion dynamics analysis of turbulent premixed swirling flames. *Journal of Fluid Mechanics*, **830**, 681–707.
115. **Pawar, S. A., S. Mondal, N. B. George, and R. I. Sujith**, Synchronization behaviour during the dynamical transition in swirl-stabilized combustor: temporal and spatiotemporal analysis. In *2018 AIAA Aerospace Sciences Meeting*. 2018. DOI: 10.2514/6.2018-0394.
116. **Pawar, S. A., S. Mondal, N. B. George, and R. I. Sujith** (2019). Temporal and spatiotemporal analyses of synchronization transition in a swirl-stabilized combustor. *AIAA Journal*, **57**(2), 836–847. DOI:10.2514/1.J057143.
117. **Pawar, S. A., A. Seshadri, V. R. Unni, and R. I. Sujith** (2017). Thermoacoustic instability as mutual synchronization between the acoustic field of the confinement and turbulent reactive flow. *Journal of Fluid Mechanics*, **827**, 664–693.
118. **Pawar, S. A. and R. I. Sujith** (2018). Transition to thermoacoustic instability in a turbulent combustor. *Journal of the Combustion Society of Japan*, **60**(192), 99–111. DOI: 10.20619/jcombsj.60.192.99.
119. **Peracchio, A. and W. Proscia**, Nonlinear heat-release/acoustic model for thermoacoustic instability in lean premixed combustors. In *Turbo Expo: Power for Land, Sea, and Air*, volume 78644. American Society of Mechanical Engineers, 1998.
120. **Perets, Y., E. Sher, and R. Harari** (2018). An experimental study on axial-flow-induced vibration of confined flexible rods with sequenced transverse rib roughness. *Experimental Thermal and Fluid Science*, **93**, 86–95.
121. **Pikovsky, A., M. Rosenblum, J. Kurths, et al.** (2001). A universal concept in nonlinear sciences. *Self*, **2**, 3.

122. **Poinsot, T. J., A. C. Trouve, D. P. Veynante, S. M. Candel, and E. J. Esposito** (1987). Vortex-driven acoustically coupled combustion instabilities. *Journal of Fluid Mechanics*, **177**, 265–292.
123. **Putnam, A. A. and W. R. Dennis** (1956). Survey of organ-pipe oscillations in combustion systems. *The Journal of the Acoustical Society of America*, **28**(2), 246–259.
124. **Rayleigh** (1878). The explanation of certain acoustical phenomena. *Nature*, **18**(455), 319–321. ISSN 1476-4687. URL <https://doi.org/10.1038/018319a0>.
125. **Renard, P. H., D. Thevenin, J. C. Rolon, and S. Candel** (2000). Dynamics of flame/vortex interactions. *Progress in Energy and Combustion Science*, **26**(3), 225–282.
126. **Rijke, P. L.** (1859). Lxxi. notice of a new method of causing a vibration of the air contained in a tube open at both ends. *The London, Edinburgh, and Dublin Philosophical Magazine and Journal of Science*, **17**(116), 419–422.
127. **Roos, F. W. and J. T. Kegelman** (1986). Control of coherent structures in reattaching laminar and turbulent shear layers. *AIAA journal*, **24**(12), 1956–1963.
128. **Rosenblum, M. G., A. S. Pikovsky, and J. Kurths** (1996). Phase synchronization of chaotic oscillators. *Physical review letters*, **76**(11), 1804.
129. **Roy, R. and A. K. Gupta** (2023). Performance enhancement of swirl-assisted distributed combustion with hydrogen-enriched methane. *Applied Energy*, **338**, 120919.
130. **Ryan, M., M. Gruber, C. Carter, and T. Mathur** (2009). Planar laser-induced fluorescence imaging of oh in a supersonic combustor fueled with ethylene and methane. *Proceedings of the Combustion Institute*, **32**(2), 2429–2436.
131. **Sampath, R. and S. R. Chakravarthy** (2016). Investigation of intermittent oscillations in a premixed dump combustor using time-resolved particle image velocimetry. *Combustion and Flame*, **172**, 309–325. DOI:<https://doi.org/10.1016/j.combustflame.2016.06.018>.
132. **Sayadi, T., V. Le Chenadec, P. J. Schmid, F. Richecoeur, and M. Massot** (2014). Thermoacoustic instability—a dynamical system and time domain analysis. *Journal of Fluid Mechanics*, **753**, 448–471.
133. **Schadow, K. and E. Gutmark** (1992). Combustion instability related to vortex shedding in dump combustors and their passive control. *Prog.Ene.Comb. Sci.*, **18**(2), 117–132.
134. **Schefer, R.** (2003). Hydrogen enrichment for improved lean flame stability. *International Journal of Hydrogen Energy*, **28**(10), 1131–1141. DOI: 10.1016/S0360-3199(02)00199-4.

135. **Schefer, R. W., D. M. Wicksall, and A. K. Agrawal** (2002). Combustion of hydrogen-enriched methane in a lean premixed swirl-stabilized burner. *Proceedings of the combustion institute*, **29**(1), 843–851.
136. **Seshadri, A., V. Nair, and R. I. Sujith** (2016). A reduced-order deterministic model describing an intermittency route to combustion instability. *Combustion Theory and Modelling*, **20**(3), 441–456.
137. **Shanbhogue, S. J., S. Husain, and T. Lieuwen** (2009). Lean blowoff of bluff body stabilized flames: Scaling and dynamics. *Progress in Energy and Combustion Science*, **35**(1), 98–120.
138. **Shanbhogue, S. J., Y. S. Sanusi, S. Taamallah, M. A. Habib, E. M. A. Mokheimer, and A. F. Ghoniem** (2016). Flame macrostructures, combustion instability and extinction strain scaling in swirl-stabilized premixed CH₄/H₂ combustion. *Combustion and Flame*, **163**, 494–507.
139. **Shoeb, A. and G. Clird** (2005). Chapter 16—wavelets; multiscale activity in physiological signals. *Biomedical signal and image processing*.
140. **Sieber, M., C. Oliver Paschereit, and K. Oberleithner** (2017). Advanced identification of coherent structures in swirl-stabilized combustors. *Journal of Engineering for Gas Turbines and Power*, **139**(2).
141. **Sierens, R. and E. Rosseel** (2000). Variable composition hydrogen/natural gas mixtures for increased engine efficiency and decreased emissions. *J. Eng. Gas Turbines Power*, **122**(1), 135–140.
142. **Singla, G., P. Scoufflaire, C. Rolon, and S. Candel** (2006). Planar laser-induced fluorescence of oh in high-pressure cryogenic lox/gh₂ jet flames. *Combustion and Flame*, **144**(1-2), 151–169.
143. **Sirovich, L.** (1987). Turbulence and the dynamics of coherent structures. i. coherent structures. *Quarterly of applied mathematics*, **45**(3), 561–571.
144. **Sivashinsky, G. I.** (1977). Nonlinear analysis of hydrodynamic instability in laminar flames—i. derivation of basic equations. *Acta astronautica*, **4**(11), 1177–1206.
145. **Small, M.**, *Applied nonlinear time series analysis: applications in physics, physiology and finance*, volume 52. World Scientific, 2005.
146. **Sondhauss, C.** (1850). Ueber die schallschwingungen der luft in erhitzten glasröhren und in gedeckten pfeifen von ungleicher weite. *Annalen der Physik*, **155**(1), 1–34.
147. **Sterling, J. and E. E. Zukoski** (1987). Longitudinal mode combustion instabilities in a dump combustor.
148. **Sterling, J. D.** (1993). Nonlinear analysis and modelling of combustion instabilities in a laboratory combustor. *Combustion Science and Technology*, **89**(1-4), 167–179.

149. **Sui, J., D. Zhao, B. Zhang, and N. Gao** (2017). Experimental study of rijke-type thermoacoustic instability by using proper orthogonal decomposition method. *Experimental Thermal and Fluid Science*, **81**, 336–344.
150. **Sujith, R. and L. Kabiraj**, Bifurcation analysis and observation of intermittency in combustion-driven thermoacoustic oscillations. *In 50th AIAA Aerospace Sciences Meeting including the New Horizons Forum and Aerospace Exposition*. 2012.
151. **Sujith, R. I., M. Juniper, and P. Schmid** (2016). Non-normality and nonlinearity in thermoacoustic instabilities. *International Journal of Spray and Combustion Dynamics*, **8**(2), 119–146.
152. **Suresh, S.**, *Fatigue of materials*. Cambridge university press, 1998.
153. **Taamallah, S., Z. A. LaBry, S. J. Shanbhogue, and A. F. Ghoniem** (2015a). Thermo-acoustic instabilities in lean premixed swirl-stabilized combustion and their link to acoustically coupled and decoupled flame macrostructures. *Proceedings of the combustion institute*, **35**(3), 3273–3282.
154. **Taamallah, S., K. Vogiatzaki, F. M. Alzahrani, E. M. Mokheimer, M. Habib, and A. F. Ghoniem** (2015b). Fuel flexibility, stability and emissions in premixed hydrogen-rich gas turbine combustion: Technology, fundamentals, and numerical simulations. *Applied Energy*, **154**, 1020–1047. URL <https://www.sciencedirect.com/science/article/pii/S0306261915004997>. DOI:10.1016/j.apenergy.2015.04.044.
155. **Takens, F.**, Detecting strange attractors in turbulence. *In Dynamical systems and turbulence, Warwick 1980*. Springer, 1981, 366–381.
156. **Timagenis, G. J.** (1980). International control of marine pollution. (*No Title*).
157. **Toker, D., F. T. Sommer, and M. D’Esposito** (2020). A simple method for detecting chaos in nature. *Communications biology*, **3**(1), 1–13. DOI:<https://doi.org/10.1038/s42003-019-0715-9>.
158. **Tony, J., E. Gopalakrishnan, E. Sreelekha, and R. I. Sujith** (2015). Detecting deterministic nature of pressure measurements from a turbulent combustor. *Phys. Rev. E*, **92**(6), 062902.
159. **Torrence, C. and G. P. Compo** (1998). A practical guide to wavelet analysis. *Bulletin of the American Meteorological society*, **79**(1), 61–78.
160. **Unni, V. R., A. Krishnan, R. Manikandan, N. B. George, R. I. Sujith, N. Marwan, and J. Kurths** (2018). On the emergence of critical regions at the onset of thermoacoustic instability in a turbulent combustor. *Chaos*, **28**(6), 063125.
161. **Unni, V. R. and R. I. Sujith** (2017). Flame dynamics during intermittency in a turbulent combustor. *Proceedings of the Combustion Institute*, **36**(3), 3791–3798.

162. **Wang, P., H. Ma, and Y. Liu** (2019). Proper orthogonal decomposition and extended-proper orthogonal decomposition analysis of pressure fluctuations and vortex structures inside a steam turbine control valve. *J. Eng. Gas Turbines Power*, **141**(4). DOI: <https://doi.org/10.1115/1.4040903>.
163. **Wilke, C. R.** (1950). A viscosity equation for gas mixtures. *The journal of chemical physics*, **18**(4), 517–519.
164. **Yazaki, T., S. Sugioka, F. Mizutani, and H. Mamada** (1990). Nonlinear dynamics of a forced thermoacoustic oscillation. *Physical review letters*, **64**(21), 2515.
165. **Yi, J., H. Xiaomin, J. ZHANG, B. JIANG, and W. Zejun** (2012). Experimental study on emission performance of an lpp/tvc. *Chinese Journal of Aeronautics*, **25**(3), 335–341.
166. **Zhang, J. and A. Ratner** (2019). Experimental study on the excitation of thermoacoustic instability of hydrogen-methane/air premixed flames under atmospheric and elevated pressure conditions. *International Journal of Hydrogen Energy*, **44**(39), 21324–21335.
167. **Zhen, H., C. S. Cheung, C. W. Leung, and Y. S. Choy** (2012). Effects of hydrogen concentration on the emission and heat transfer of a premixed lpg-hydrogen flame. *international journal of hydrogen energy*, **37**(7), 6097–6105.
168. **Zhou, H., Y. Huang, and S. Meng** (2017). Response of non-premixed swirl-stabilized flames to acoustic excitation and jet in cross-flow perturbations. *Experimental Thermal and Fluid Science*, **82**, 124–135.

CURRICULUM VITAE

1. **NAME** : Abhishek Kushwaha

2. **DATE OF BIRTH** : 15 Oct 1994

3. **EDUCATIONAL QUALIFICATIONS**

2017 Bachelor of Technology (B. Tech.)

Institution : Babu Banarasi Das National Institute of Technology
and Management, Lucknow

University : Dr. A.P.J. Abdul Kalam Technical University,
Lucknow

Specialization : Aeronautical Engineering

Master of Science (M. S.)

Institution : Indian Institute of Technology, Madras

Specialization : Aerospace Engineering

Doctor of Philosophy

Institution : Indian Institute of Technology, Madras

Specialization : Aerospace Engineering

Registration Date : 09 Jul 2018

PUBLICATIONS

1. REFEREED JOURNAL ARTICLES BASED ON THE THESIS

- (a) **A. Kushwaha, K. Praveen, Samadhan A. Pawar, R. I. Sujith, I. Chterev, and I. Boxx** (2021). Dynamical characterization of thermoacoustic oscillations in a hydrogen-enriched partially premixed swirl-stabilized methane/air combustor. *Journal of Engineering for Gas Turbines and Power*, **143(12)**: , 121022 (11 pages).

2. REFEREED JOURNAL ARTICLES (Others)

- (a) **A. Sahay, A. Kushwaha, Samadhan A. Pawar, PR Midhun, Jayesh M. Dhadphale, and R. I. Sujith** (2023). Mitigation of limit cycle oscillations in a turbulent thermoacoustic system via delayed acoustic self-feedback. *Chaos: An Interdisciplinary Journal of Nonlinear Science*, **33(4)**, 043118.

3. REFEREED CONFERENCE ARTICLES

- (a) **A. Kushwaha, K. Praveen, Samadhan A. Pawar, R. I. Sujith, I. Chterev, and I. Boxx** (2021). Dynamical characterization of thermoacoustic oscillations in a hydrogen-enriched partially premixed swirl-stabilized methane/air combustor. *Turbo Expo: Power for Land, Sea, and Air*, (pp. **V03BT04A024**).

DOCTORAL COMMITTEE

CHAIRPERSON:

Dr. H S N Murthy
Professor and Head
Department of Aerospace Engineering

GUIDE(S):

Dr. R I Sujith
D. Srinivasan Chair Professor
Department of Aerospace Engineering

MEMBERS:

Dr. Nagabhushana Rao Vadlamani
Assistant Professor
Department of Aerospace Engineering

Dr. Nandan Kumar Sinha
Professor
Department of Aerospace Engineering

Dr. Niket Kaisare
Professor
Department of Chemical Engineering